FABRICATION AND CHARACTERIZATION OF SOLID OXIDE FUEL CELL INTERCONNECT ALLOYS

A Dissertation
Presented to
The Academic Faculty

by

Benjamin Cortright Church

In Partial Fulfillment
Of the Requirements for the Degree
Doctor of Philosophy in Materials Science and Engineering

Georgia Institute of Technology
Atlanta, Georgia

October, 2004

FABRICATION AND CHARACTERIZATION OF SOLID OXIDE FUEL CELL INTERCONNECT ALLOYS

Approved by:

Dr. Thomas H. Sanders, Jr., Advisor

Dr. Joe K. Cochran

Dr. Henry Paris

Dr. Robert Speyer

Dr. Naresh Thadhani

Date Approved: October 26, 2004

Dedication

for Jerry

Acknowledgments

I would like to thank Dr. Tom Sanders for being an outstanding adviser and mentor. His guidance and insight have been invaluable both in completing my research and throughout my academic development. Dr. Joe Cochran has been a great source of enthusiasm and his knowledge of ceramics and paste extrusion helped me overcome many processing hurdles. Dr. Robert Speyer has been a tremendous help in working with dilatometric and thermogravimetric equipment as well as teaching me the meaning of scientific rigor. I would like to thank my other committee members, Dr. Naresh Thadhani and Dr. Henry Paris for their encouragement, advice, and support. I would also like to thank the faculty and staff of the School of Materials Science and Engineering.

I have had the great pleasure of working with many talented and friendly people while here at Georgia Tech. My current and past group members, Jason Nadler, Kevin Hurysz, 'Le Hayes, Ray Oh, Tammy McCoy, Justin Clark and Wes Seay, have all been good friends and colleagues who were always willing to lend a hand, discuss an idea, or go to coffee. I have also enjoyed working with Tracie Durbin and Matt Trexler who have been terrific officemates and have helped with so many of the small-yet-important aspects of graduate school. I would like to extend my thanks to Jeff King, Curtis Neff, Silvia Liong, Lou Ferranti, Greg Kennedy, Monique McIntosh, Bill Nemeth, and Yancy Riddle. I would

also like to thank Dr. Walt Milligan for his advice over the years.

I would like to express my gratitude to my immediate and extended family for the years of support and encouragement. My parents, Jim and Mary Ann, have inspired me throughout my entire life to work hard, invest in myself through education, and to strive to be a good person. My brothers, Bob and Tim, have been life-long friends and role models. My scholastic achievements pale in comparison to their exemplary lives. Finally, I would like to thank my wife, Carmen, for her unending love, encouragement, and understanding.

This work was sponsored by DSO of DARPA (N00014-99-1-1016) under Dr. Leo Cristodoulou and by ONR (N00014-99-1-0582) under Dr. Steven Fishman.

Table of Contents

List of Tables

List of Figures

Summary

Metal alloy honeycomb structures were fabricated using a paste extrusion technique and characterized for potential application as interconnects in solid oxide fuel cells. Thermal expansion characteristics of Fe-Cr, Fe-Ni, Ni-Cr, Fe-Ni-Cr, and similar alloys containing an oxide dispersion were determined and compared with the thermal expansion behavior of yttria-stabilized zirconia (YSZ). A method was developed to calculate thermal expansion mismatch between two materials under a variety of heating and cooling conditions. It was shown that Fe 20 wt% Cr and Fe 47.5 wt% Ni alloys have low expansion mismatch with YSZ under a wide range of heating and cooling conditions. Oxidation experiments showed that Fe-Cr alloys have superior oxidation resistance in air at 700 °C compared with Fe-Ni-Cr alloys with similar chromium contents. The inclusion of oxide dispersions (Y_2O_3 and CaO) into an alloy honeycomb was shown to improve oxidation resistance without affecting thermal expansion behavior. The honeycomb extrusion process provides a method by which experimental alloys can be produced and characterized rapidly to develop an alloy suitable for use as an interconnect in a solid oxide fuel cell.

1. Introduction

Fuel cells are generally regarded to be of central importance for the transformation to the so-called hydrogen economy. These devices offer the impressive potential of efficient generation of power using a fuel such as hydrogen with essentially no environmentally harmful by-products. As such, fuel cells have been the focus of many recent research programs.

Technological advances have made it possible to incorporate metal alloys in place of the traditional ceramic interconnect material in certain fuel cell devices. The use of a metal interconnect can serve to reduce fabrication costs, improve the efficiency of the fuel cell, and facilitate the production of more complex fuel cell designs. However, the fuel cell operating environment is harsh and many common metal alloys are not capable of performing adequately over extended periods. This has lead to the search for a metal alloy with specific physical and mechanical properties that could be applied successfully as a fuel cell interconnect.

This work is in essence a discussion of designing an alloy with tailored properties and creating that alloy, entirely in the solid state, from metal oxide precursors. Alloys are produced using a thermo-chemical processing technique which utilizes inexpensive metal oxide powders as raw ingredients. These powders are formed into useful shapes by way of a paste extrusion technique. After the desired shape has been produced, the material is

processed at high-temperatures in a hydrogen atmosphere where the metal oxides are reduced into the constituent metals and sinter to form a relatively dense metallic structure. After processing, the materials can be characterized to determine physical and mechanical properties which can then be used to ascertain the suitability of the particular alloy for use as an interconnect in a fuel cell.

The criteria used to select a suitable interconnect remain non-specific, likely due to the fact that many fuel cell designs, materials, fuels, for example, are currently under investigation. This study places a focus on thermal expansion behavior of the potential alloy as being the primary selection criterion. The fuel cell structure for which these alloys are being designed is particularly susceptible to processing defects which are, in part, due to thermal expansion related issues. That being the case, it is more important to fabricate a defect-free structure than it is to demonstrate the ability to operate the structure for an extended period of time.

This work aims to understand the thermal expansion behavior of alloys within the Fe-Cr, Fe-Ni. and Fe-Ni-Cr systems produced from metal oxide precursors and to propose methods by which the thermal expansion behavior of a given alloy can be examined to determine the applicability of that alloy as a fuel cell interconnect. In addition, other performance criteria are examined including mechanical properties and oxidation resistance in air. In combination, these provide a basis from which an alloy can be designed for eventual service as the interconnect of a fuel cell.

2. Background

2.1 Solid Oxide Fuel Cells

Fuel cells are devices that electrochemically convert a fuel into usable electricity. A simplified schematic of a fuel cell is shown in Figure 1. A fuel such as hydrogen comes into contact with the electrolyte on the anode side of the cell where it is oxidized and in the process releases electrons which flow toward the outside circuit. The oxidant, typically oxygen, accepts electrons from the outer circuit and ionizes. The oxidant then diffuses through the electrolyte via ionic diffusion toward the anode where it meets with the fuel and completes the cycle. The electron flow through the circuit produces a direct current that can be used as a power source.

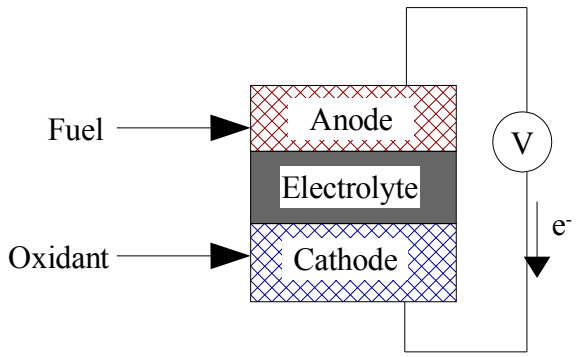

Figure 1. Schematic of a basic fuel cell.

A solid oxide fuel cell (SOFC) is a specific type of fuel cell which utilizes an ion-conducting ceramic material as the electrolyte. These solid-state structures typically operate at relatively high temperatures (~ 700 °C) where the electrolyte has sufficiently high ionic conductivity. Zirconia stabilized with yttira (YSZ) is commonly used as the electrolyte. A SOFC also uses anode and cathode materials, typically nickel-YSZ cermet and doped lanthanum manganite, respectively. Often, the cell is stacked in such a way that additional voltage can be created. In this case, an interconnect component is needed to electrically connect the different cells as also to provide physical barriers to keep the oxidant and fuel separated. Several designs of SOFCs have been created, the most significant of which have been reviewed by Minh [1].

The fuel and oxidant could, in theory, be any combination of gases that would provide the electrochemical reaction required for power generation to occur. Hydrogen is by far the most common fuel in use. The hydrogen can be in the form of pure hydrogen gas, methane, or alcohols. The oxidant most commonly used is oxygen which is introduced into the SOFC in the form of natural air or as a pure gas. With these common gases, the fuel cell reaction produces by-products of water vapor and heat.

The flat-plate, or planar type of SOFC has been the subject of intense research due to it's potential for becoming an efficient, high energy-density power generation device. A schematic of a planar SOFC [2] is shown in Figure 2. The structure is comprised of individual layers of anode, electrolyte, cathode, and interconnect materials. The individual cells can be layered, or stacked, to form multi-cell structures thereby providing for additional power generation capabilities. The traditional SOFC fabrication method consists of assembling alternating layers of anode, interconnect, electrolyte and cathode at room temperature [1]. The layers are stacked to create the desired cell height and seals, such as

compression, glass, or cement, are applied to the edges of the plate to make the stack hermetic. Certain types of seals require a high-temperature heat-treatment during which the layers become rigidly joined while other seals become rigid upon application at room temperature. The selection criteria used for the anode, cathode, and electrolyte materials are beyond the scope of the current work; Minh [1] provides additional information on this topic.

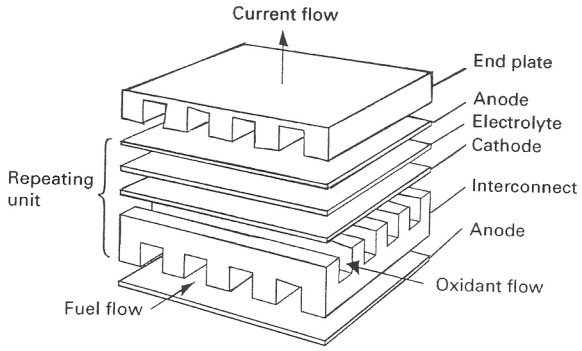

Figure 2. Schematic of a typical planar SOFC stack [2].

2.2 Interconnect

The interconnect serves several vital functions in the SOFC structure. First, it provides electrical contact between cells allowing the stack to function as a single power generation unit. In addition, the interconnect keeps the oxidant and fuel gases from mixing by forming a dense, physical barrier between the repeating cells. In certain designs, the interconnect may also provide mechanical support to the SOFC structure.

The traditional material used for the SOFC interconnect is lanthanum chromite ($LaCrO_3$). This material exhibits a remarkable high electric conductivity under SOFC

operating conditions compared with typical ceramics with a value of 1 Ω^1 cm^{-1} at 1000 °C [1]. The conductivity of $LaCrO_3$ can be improved up to a factor of 35 times by doping with magnesium, strontium, or calcium oxides. In addition to high electrical conductivity, $LaCrO_3$ exhibits other properties which make it particularly well suited for the interconnect. It is chemically stable in both the typical anode and cathode side environments. The coefficient of thermal expansion (CTE) of $LaCrO_3$ at temperatures above 240 °C is roughly $9.8 \cdot 10^{-6}$ K^{-1} which is quite similar to the other common materials in a SOFC.

The advantages of $LaCrO_3$ do not come without weaknesses. Lanthanum, being a rare-earth element, is expensive compared with typical engineering materials. Because $LaCrO_3$ is a ceramic, processing methods are limited which results in limitations as to the geometry of interconnect that can be fabricated. Also, the $LaCrO_3$ is difficult to sinter to a high relative density which makes processing of a hermetic $LaCrO_3$ layer difficult. Because of these weaknesses of $LaCrO_3$, significant research efforts have been made to find an alternative material.

Metal alloys are widely seen as possessing superior properties compared with $LaCrO_3$ which offer the potential to increase efficiency of the SOFC. Metals generally have very high electrical conductivity. Since any decrease in resistance of the cell would translate directly into increased output, moving to a more electrically conductive interconnect material could offer significant advantages. Thermal conductivity for metals is generally higher than for ceramics. Incorporating a high thermal conductivity material into a SOFC stack would serve to reduce temperature gradients within the structure that could impact thermal stresses and stack efficiency. Metals are generally easy to fabricate into a wide variety of shapes, which would allow designers to fabricate more complex SOFC designs. Also, many metals and alloys are relatively inexpensive and readily

available.

Metallic alloys, however, also bring several negatives along with these potential benefits. The two main negative aspects of metal alloys for SOFC interconnects are oxidation of the metal during operation and the potential for problems arising due to thermal expansion mismatch between the metal other SOFC materials. In a broad sense, metals tend to have higher CTEs compared with ceramics. In terms of the SOFC, this can cause significant levels of stress to develop when temperature changes. Metals also tend to oxidize when exposed to the range of temperatures and atmospheres commonly seen during operation of a SOFC. Excessive oxidation could lead to such problems as reduced efficiency due to higher surface resistance or the eventual loss of hermeticity of the interconnect layer. A discussion of potential interconnect alloys is given later in this section.

In general terms, the properties which a metal interconnect should possess can be described as follows:

A) Thermal expansion. The thermal expansion of the interconnect metal should match with the other materials in the SOFC. It is particularly important that the alloy match well with the electrolyte.

B) Oxidation resistance. The alloy must not corrode severely under the operating conditions of the fuel cell in both anode and cathode atmospheres. Furthermore, the oxidation layer of the interconnect should exhibit some degree of electrical conductivity and should be adherent to the base alloy.

C) Hermeticity. The interconnect must be able to prevent the mixing of the fuel and oxidant gases. Permeability of H^+ and O^{-2} ions should be minimized.

D) Innocuous to other SOFC materials. The alloy and it's oxidation layer should not

contribute to the chemical degradation of other SOFC materials. (i.e. chromia poisoning of the electrode).

E) Thermodynamic stability. The alloy must be thermodynamically stable during processing and operation of the SOFC.

F) Low cost. The cost of the alloy should be low to help facilitate the economic manufacture of the SOFC.

2.3 Hybrid Solid Oxide Fuel Cell

Recently, Rauch, *et al.* [3] have described a method for producing SOFC stacks by means of a paste extrusion technique developed at Georgia Tech. An example of a SOFC structure making use of this technique is shown schematically in Figure 3. The main structure is comprised of alternating layers of electrolyte and metal interconnect. These layers are made from the simultaneous co-extrusion of two pastes using a custom-made extrusion system. The interconnect paste is comprised of metal oxides blended in proportion to yield the desired metal alloy composition and the electrolyte paste is comprised of YSZ. After co-extrusion, the SOFC stack is heat-treated in a highly reducing atmosphere where the metal oxides that constitute the interconnect layers reduce, densify and homogenize. The YSZ electrolyte is chemically stable in the reducing atmosphere and only undergoes densification. The anode, cathode, gas manifolds, and contacts are added in post-heat-treatment stages. Cochran *et al.* [4] have discussed the co-extrusion process used to fabricate these hybrid SOFC stacks in greater detail and have also mentioned processing issues such as co-sintering and joining of metal and ceramic layers.

The hybrid SOFC fabrication method is significantly different from the traditional SOFC fabrication method which consists of assembling the alternating layers of anode,

interconnect, electrolyte and cathode at room temperature. The layers are stacked to create the desired cell height and seals, such as compression, glass, or cement, are applied to the edges of the plate to make the stack hermetic. Certain types of seals require a high-temperature heat-treatment during which the layers become rigidly joined while other seals become rigid upon application at room temperature. Stresses as a result of thermal expansion mismatch evolve from either an initial room-temperature stress-free state of from a high-temperature (seal processing temperature) stress-free state. Typically, the SOFC will not be exposed to temperatures in excess of roughly 700 °C which is the operating temperature of the fuel cell.

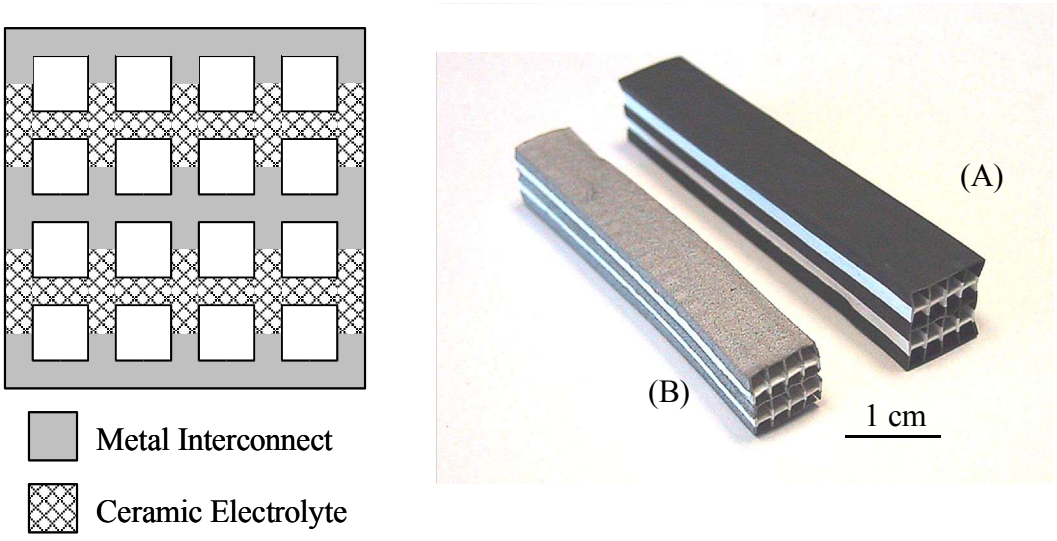

Figure 3. Schematic of a hybrid fuel cell stack (left) comprised of alternating layers of interconnect and electrolyte. Photos of (A) as-extruded hybrid stack and (B) after heat-treating in hydrogen (After Rauch, *et al.* [3]).

2.4 Processing Challenges for the Hybrid Solid Oxide Fuel Cell

After co-extrusion, the hybrid SOFC stack is processed using a reduction heat-

treatment which is comprised of three main stages: initial heat-up, high temperature hold, and cool-down. During this heat-treatment, the interconnect paste reduces and sinters and the electrolyte sinters. After the high-temperature processing, the main structure undergoes further steps to incorporate the electrode layers and gas manifolding needed for operation.

The successful fabrication of a hybrid SOFC is not trivial. Eisele [5] has recently modeled the stresses which develop during the reduction and sintering stages of the extruded hybrid stack and observed various processing defects. It was noted that severe cracking can result from even slight changes in heat-treatment schedules. Some issues related to the cool-down from processing were also mentioned including the potential for stress-relaxation in the ceramic electrolyte depending on the porosity of the ceramic and the cooling rate. For scandia-stabilized zirconia, it was estimated that stress relaxation could occur as low as 1200 °C with a 5 °C/min cooling rate and 10% porosity. Cochran, *et al.* [4] showed that while total shrinkage of the YSZ portion of the hybrid SOFC stack can be similar to that of the metal interconnect, the shrinkage of the different components occurs to different extents at different temperatures during the reduction/sintering heat-treatment, which then leads to cracking and delamination of the YSZ/metal interface. These defects will result in a structure that is neither hermetic nor mechanically reliable. It was also shown that the sintering profile of the metal interconnect layer can be modified to match the sintering profile of YSZ more closely by making changes to the raw material (i.e. particle size and distribution) or changing the sintering heat-treatment profile.

The work of Eisele and Cochran *et al*. refer to the potential for reducing or eliminating processing related defects caused during the heat-up and hold steps in the reduction heat-treatment of the hybrid SOFC. The potential for the generation of defects during the cool-down stage also exists. Any differential contraction between electrolyte

and interconnect materials could potentially create strain within the structure. Defects occurring during the heat-up and high-temperature hold stages can be addressed through modifications to the heat-treatment schedule or through manipulation of the constituent powders [4, 5]. However, with a given geometry and cooling schedule, the contraction of the metal upon cooling can only be modified by changing the metal composition. Furthermore, using a metal with a closer thermal expansion match to the electrolyte reduces the likelihood of failure due to thermal cycling during service. Therefore, the thermal expansion behavior of the metal interconnect must be tailored to match that of the electrolyte.

2.5 Thermal Stress Due to Thermal Expansion Mismatch

While it is not the intention of this work to address the concept of stress in the SOFC directly, a basic discussion of the topic will help to provide context to the issue of thermal expansion mismatch. A recent paper by Montross, *et al.* [6] provides an excellent overview of the topic and defines key relations used to estimate stress in various planar SOFC components.

Thermal stresses in a SOFC (planar or hybrid) can arise as a result of several factors after the fabrication of the stack is complete and it is placed into service. Thermal gradients that may be present in the stack when at the operating temperature can cause thermal stresses to develop. This has been studied for the case of tubular SOFC designs by Hall and Colclaser [7]. Planar and hybrid designs are considered to be more difficult to study due to the lower degree of symmetry compared with tubular structures. One benefit of metal interconnects is the generally higher thermal conductivity of metals compared with ceramics. Higher thermal conductivity would result in a more even distribution of thermal

energy throughout the structure thereby reducing stresses associated with thermal gradients.

Stress could also develop as a result of a phase change or composition change within one of the various SOFC materials. A Fe alloy consisting of 0 to 10 wt% Cr would undergo an α to γ phase transformation upon heating to temperatures in the range of 831 to ~ 1000 °C. There is a volume change associated with such a phase change; this rapid volume change would result in the development of stresses in the SOFC stack. In a similar way, changes to the chemistry of ceramic SOFC components could occur that could alter the CTE of the material. For example, the elastic modulus of $LaCrO_3$ can change as a function of oxygen partial pressure [8]. Since the elastic modulus relates how a strain would equate with stress, a change in the elastic modulus would change the stress associated with a given strain.

A difference in CTEs of various SOFC materials would also account for the development of stress in the structure. Any two materials, joined or constrained, with different thermal expansion behavior, would develop stress as a result of temperature changes. Since a SOFC is commonly assembled at one temperature and placed into operation at another, any difference in thermal expansion behavior of the different materials would become a potential source of stresses in the SOFC. In addition, a SOFC would likely experience thermal cycling during service due to periodic shut-downs and restarts. The importance of a close thermal expansion match between SOFC materials is well understood and is commonly mentioned when various interconnect alloys are examined for potential use in a SOFC. However, there has been relatively little work in examining the precise impact of a difference in thermal expansion behavior for a particular design. This may be partly because the actual design of the stack would likely have a strong effect when

attempting to understand the development of such stresses. A generalized approach for understanding the impact of a thermal expansion difference between different SOFC materials was used by Montross *et al.*, originally created for multi-layered stacks by Incan and Munz [9] and Bergreen [10]. For a constrained plate made of a number of individual layers (*i*) which can expand into the x-y plane only, the stress in the x-y plane of layer *i*, σ^i can be estimated by

$$\sigma^i = E_i^{'}(\alpha - \alpha_i)\Delta T \tag{2.1}$$

where $E_i^{`}$ is the effective elastic modulus which is calculated from the elastic modulus, *E*, and the Poision's ratio, ν, by

$$E_i^{'} = \frac{E}{(1-\nu)} \tag{2.2}$$

and α is the overall expansion coefficient of *N* layers of *h* thickness [6]. The value of the overall CTE value α is defined as

$$\alpha = \sum_{1}^{N} \frac{E_i\, h_i\, \alpha_i}{E_i\, h_i} \tag{2.3}$$

The main concept taken from this stress calculation is that the stress is proportional to the difference in CTEs of the different materials multiplied by the temperature interval. It was noted by Montross *et al.* that the actual state of stress of a SOFC stack would be dependent

on the actual geometry of the stack design. The equation for the constrained series of laminates was simply used as a base from which materials could be compared. Stress relations assuming fully constrained and fully unconstrained conditions were also presented. These conditions also showed that the stress in a given layer of laminate is proportional to the CTE difference between the component materials.

The equation for semi-constrained stress in the laminate stack reveals a subtlety regarding the CTE of the different materials. The method used to calculate CTE must be understood and compensated for when analyzing this type of equation. The equation shown assumes that CTE values, α, were calculated using a formula such as

$$\alpha = \frac{1}{l_0} \cdot \frac{\Delta l}{\Delta T} \tag{2.4}$$

where l_0 is the length at room temperature and l is the length at temperature T. This can be considered as the slope of a chord on an expansion vs. temperature plot for a given material. This form of CTE is widely reported in tabular form for various materials. In order to calculate the percent expansion from this form of CTE, one would simply be required to multiply the CTE by ΔT.

Small yet discernible errors could be introduced using this method. If the CTE of the material were not completely linear with temperature, it would be necessary to calculate the CTE using the same upper and lower temperature values that were to be used in the calculation to estimate stress. Using a CTE value calculated from a different temperature range would introduce an error into the result. The error would likely be small and would be related to the degree of non-linearity of the CTE with temperature. This would

potentially limit the ability to estimate stress levels accurately at various temperatures if the researcher did not have access to CTE values at all temperature ranges of interest. The CTE of a material can also be defined as

$$\alpha = \frac{1}{l_0} \cdot \frac{dl}{dT} \tag{2.5}$$

which is essentially the slope at a point on the expansion versus temperature plot for a given material. To extract a percent expansion from a CTE in this form, one would be required to integrate the CTE with respect to temperature. If the CTE were independent of temperature, this would simply take the form of

$$\frac{\Delta l}{l_0} = \int \alpha \, dT = \alpha \, \Delta T \tag{2.6}$$

When α is temperature dependent, the relation between α and T must be know and, therefor, expansion could not simply be equated to $\alpha \cdot \Delta T$. If an equation for CTE versus temperature could be obtained, the percent expansion of a material with non-linear CTE-temperature behavior could be calculated accurately. However, such equations are not typically found in reference literature of thermal expansion data.

The thermal expansion behavior of the various component materials should be closely matched to minimize the stress in a SOFC. The amount of allowable mismatch in thermal expansion has been mentioned [2, 6] though the proposed design limits are not generally in agreement. These proposed design limits are intended for traditional planar

SOFC stacks; the hybrid SOFC design will require a separate set of limits due to the different fabrication process. Montross *et al.* estimated probability of failure of a laminate structure based on material properties, layer thickness, and CTE difference. In general, they determined that the range of CTE values of the different materials must be within 1%. Linderoth *et al.* estimate that a CTE difference of 0.2 to $0.8 \cdot 10^{-6}$ K^{-1} between a metal interconnect and YSZ electrolyte would be sufficient to ensure a low probability of failure.

These general guidelines for a planar SOFC may not necessarily reflect the requirements of a hybrid SOFC stack. However, the main tenet that excessive CTE differences between major components must be avoided would be applicable to any SOFC design that incorporates rigid joining of different materials such as with the hybrid stack design.

2.6 Oxidation of the Interconnect

Oxidation of the interconnect can lead to a loss in efficiency of the stack due to the increased electrical resistance of the oxidation layer or, in a severe case, loss of hermeticity of the interconnect layer. There are two general methods used to improve the oxidation resistance of an alloy: alloying additions and coatings. Of these two methods, only alloy additions are discussed here.

Alloying additions of aluminum and chromium are often made to engineering alloys to improve oxidation resistance. These elements tend to form dense, adherent oxide layers on the surface of the alloy during oxidation. The oxide layer then acts as a diffusion barrier and slows the oxidation process. This phenomenon is well understood and appears in introductory texts on the topic of oxidation [11].

Oxidation layers of alumina are considerably more protective to the base alloy

compared with chromia layers. For this reason, when oxidation resistance of the alloy is of primary importance, alloying additions of aluminum to the alloy are preferable to chromium. Also, successful oxidation prevention can typically be accomplished with a lower alloying composition of aluminum than with chromium.

Often, a particular application will place more than a single demand upon the material. For the case of the SOFC interconnect, considerations such as thermal expansion and electrical conductivity are also crucial along with oxidation resistance. The electrical conductivity of alumina is roughly three orders of magnitude less than that of chromia. The added resistance of alumina would have a significant effect on the efficiency of the fuel cell. For this reason, alloys which form protective layers of alumina during oxidation are generally considered to be inferior to chromia formers for application as an interconnect [24].

Iron-based alloys have received much attention for potential application as SOFC interconnects. Traditionally, Fe-based steels with additions of chromium have been used in room and medium (~ 500 °C) temperature applications where oxidation or corrosion resistance is required. The addition of chromium to the alloy is made primarily to promote the formation of a dense, adherent layer of Cr_2O_3 on the surface of the alloy.

The SOFC offers a new challenge for such materials mostly due to the slightly higher temperature during service (~ 700 °C) compared with more common applications. As a result, many recent publications contain data on the oxidation behavior of various Fe-based alloys for use in a SOFC environment. The majority of the work has been performed on commercially available alloys or sample materials provided directly by metal producers. Oxidation is commonly studied in an air environment as it is believed that the "cathode" or air side of the SOFC is a more demanding environment. Other studies have been

conducted in H_2 atmospheres with a variety of H_2O partial pressures, methane, or atmospheres with controlled sulpher additions. A more complete discussion of research into potential interconnect alloys and the oxidation behavior of each particular system is provided in a later section.

While the formation of a dense chromia layer is beneficial to prevent continued oxidation of the interconnect, the presence of chromia also has the potential to cause performance degradation of the fuel cell through a process commonly referred to as chromia poisoning [12, 13]. In this situation, chromium deposits on to the anode and cathode materials in the fuel cell and degrades the electrical performance of the electrode thereby reducing the overall efficiency of the SOFC stack.

2.7 Potential Interconnect Alloys

A metal interconnect must exhibit certain specific properties, several of which were outlined previously. Many materials can be immediately excluded from consideration based on these performance criteria and known material properties. For example, platinum would provide an excellent combination of oxidation resistance and electrical conductivity but the high material cost would be prohibitive for the economic production of these devices. Similarly, copper would be relatively inexpensive and highly conductive, but it would melt during the high-temperature processing of the hybrid stack. The following section provides an overview of potential alloy systems, highlighting recent work done and the potential each has for application as a SOFC interconnect. Several reviews on the topic of potential alloys for SOFC interconnects have been published recently [2, 14, 15].

2.7.1 Iron-Chromium

The iron-chromium system has long been used as the basis of many engineering alloys for high-strength, corrosion-resistant applications. Chromium acts as an α-phase stabilizer when added to iron because chromium has the same BCC crystal structure as α-iron. This results in the suppression of the FCC γ-phase of iron and creates the so-called "γ-loop" in the Fe-Cr phase diagram, Figure 4 [16]. At low temperatures, chromium and iron do not form a complete solid solution due to the presence of the σ-phase which has a tetragonal structure and is generally hard and brittle. The equilibrium phase diagram predicts the formation of σ-phase for alloys containing greater than 15 wt% Cr at temperatures between 475 and 821 °C. However, heat-treatments at high temperatures and long hold times or slow cooling rates are required for the formation of this phase. For a Fe 27 wt% Cr alloy, it was shown that the σ-phase would precipitate out of the α-phase after holding at 565 °C for 131 days [17]. A Fe-20 wt% Cr alloy, held at temperatures of 600 °C and above, would be within the α-phase field and would therefore never form σ-phase even after extended high-temperature exposure.

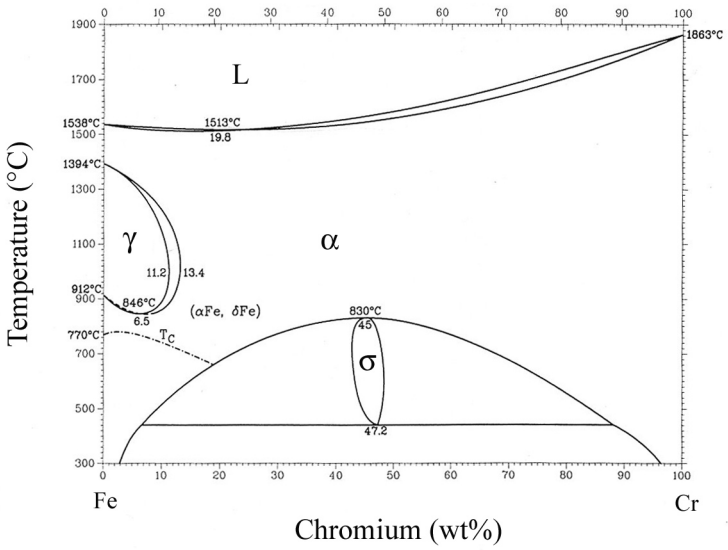

Figure 4. Fe-Cr phase diagram, after [16].

Iron-chromium based alloys have been widely investigated for application as interconnects in fuel cells [18, 19, 20, 21, 22]. Fe-Cr alloys containing between 15 and 40 wt% Cr have been shown to have average CTE values close to that of YSZ [18]. Oxidation rates of Fe-Cr alloys have been studied at SOFC operating temperatures in air [18], wet air, [23], and carbon-containing [24] atmospheres.

Linderoth and Larsen [18] used commercially provided binary Fe-Cr alloys ranging in composition from 10 to 60 wt% Cr to study thermal expansion and oxidation in air. It was shown that the best corrosion resistance was observed from a Fe 20 wt% Cr sample. The application of a ceria coating on the surface of a bare Fe 40wt% Cr sample decreased the scale growth at 1000 °C in air by a factor of four compared with the same alloy without the ceria coating.

Uehara, *et al.* [19] investigated the impact of small alloying additions to Fe-Cr alloys containing ~ 20 wt% Cr on the oxidation rate and contact resistance of the oxide scale. Contact resistance was found to increase with chromium content while oxidation rate

decreased with increasing chromium. The impact of small variations in Mn, Si, C, and Al additions were not significant in comparison to that due to a variation in chromium content.

The oxidation rate and contact resistance of a commercial Fe-Cr alloy (E-Brite) with 26 wt% Cr and 1 wt% Mo was studied by Huang, *et al.* [20]. The oxidation rate of the alloy, Figure 5, was shown to be strongly dependent on temperature. The area-specific resistance of the resultant oxide layer was said to approach the "toleration limit" for a practical SOFC device after oxidation at temperatures of 850 °C when using an oxide-based electrode contact. The average thermal expansion coefficient (α_M) of this alloy was reported to be $11.8 \cdot 10^{-6}$ K^{-1} between room temperature and 500 °C.

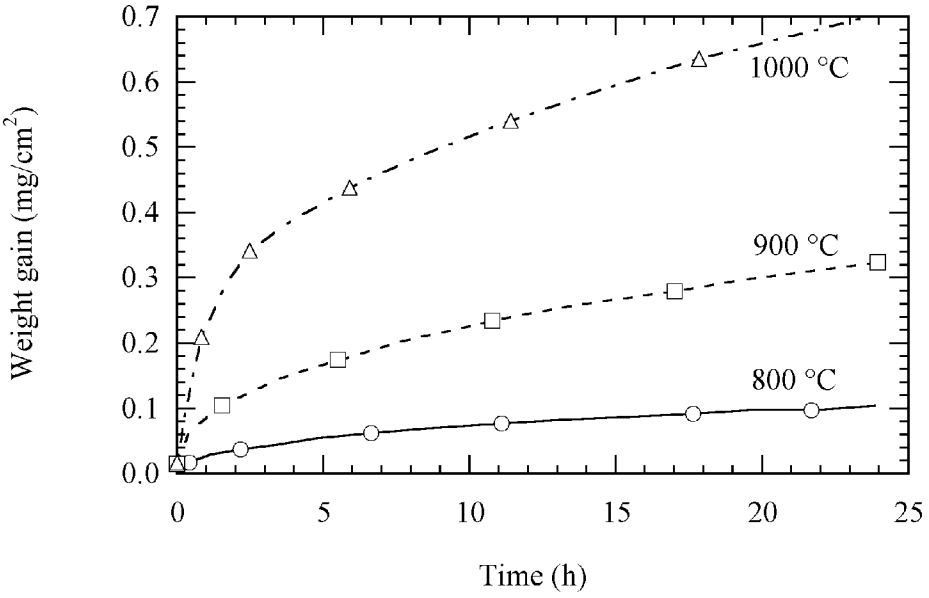

Figure 5. Oxidation in air of a Fe 26 wt% Cr 1 wt% Mo alloy, after [20].

Oxidation of a Fe 22 wt% Cr alloy was studied in wet air and hydrogen at two water vapor levels by Mikkelsen and Linderoth [23]. It was determined that a variation in the water vapor content in the oxidizing atmosphere affected oxidation rate; lower oxidation rates were observed with increased water vapor contents. This was determined to be due to

the fact that wet air facilitated the vaporization of the chromia from the oxide layer, thereby lowering the observed weight gain of the sample. In addition, the oxide scale structure was observed to be different for oxides grown in hydrogen-rich or air atmospheres.

Horita *et al.* [24] studied the oxidation of two commercial Fe-Cr alloys containing 16 and 22 wt% Cr in a wet methane atmosphere at 800 °C. Results indicated that a higher chromium-containing alloy would have a slightly lower oxidation rate in that environment. Electrical conductivity measurements showed that the 22 wt% Cr alloy had higher conductivity after the oxidation experiment compared with the 16 wt% Cr alloy. The oxide layers for both alloys were found to be comprised of Cr_2O_3 along with Fe-Mn-Cr spinel.

Additions of rare-earth elements, specifically Neodymium (Nd) and Praseodymium (Pr), were shown by Villafañe *et al.* [25] to improve the oxidation resistance of a Fe-Cr alloy in air. Small additions of these elements (~ 0.03 wt%) were shown to drastically reduce weight gain of a Fe 13 wt% Cr alloy in air at 800 °C.

The majority of research conducted on Fe-Cr based alloys have used commercially available or supplier-provided experimental alloys. Oxidation behavior of the alloy has typically been the main emphasis of research programs and only passing attention has been given to thermal expansion behavior and other properties. When thermal expansion has been investigated specifically, the published results have not been sufficiently detailed to allow for an exacting comparison of thermal expansion mismatch between the metal and YSZ. Linderoth and Larsen [18] presented expansion data in the form of α_M values as a function of temperature for Fe-Cr alloys which, as discussed earlier, tends to diminish the variation that the CTE can have over small temperature intervals. Presenting data in the form of α_T versus temperature allows for a more complete picture of the material's

behavior.

2.7.2 Chromium Based Alloys

Chromium based alloys with a dispersion of oxide particles have been investigated for potential application of SOFC interconnects primarily due to the high oxidation resistance of the alloy and the relatively low CTE of 9 to $10 \cdot 10^{-6}$ K^{-1} [15]. The addition of the oxide dispersion has been shown to improve mechanical properties of Cr-based alloys and reduce the detrimental effect of ambient temperature ductile-to-brittle transitions commonly found in these alloys [26].

It was shown by Nadler [27] that the complete reduction of pure chromium oxide is not possible using standard laboratory temperatures and atmospheres. Complete reduction of chromium oxide occurred when chromia was added to iron oxide as an alloy addition of 25 wt% or less Cr in Fe. Because it is believed that chromium based alloys can not be successfully produced using the honeycomb extrusion process, these alloys were eliminated from consideration in the current work.

2.7.3 Iron-Nickel

Nickel and iron form a solid solution in the FCC γ-phase across the entire composition range at temperatures between 912 and 1394 °C. Nickel is often added to Fe-based stainless steels to improve the corrosion resistance of the material. At higher Ni contents, the Fe-Ni system forms the basis of iron-nickel superalloys where the addition of iron is made to decrease the cost of the alloy.

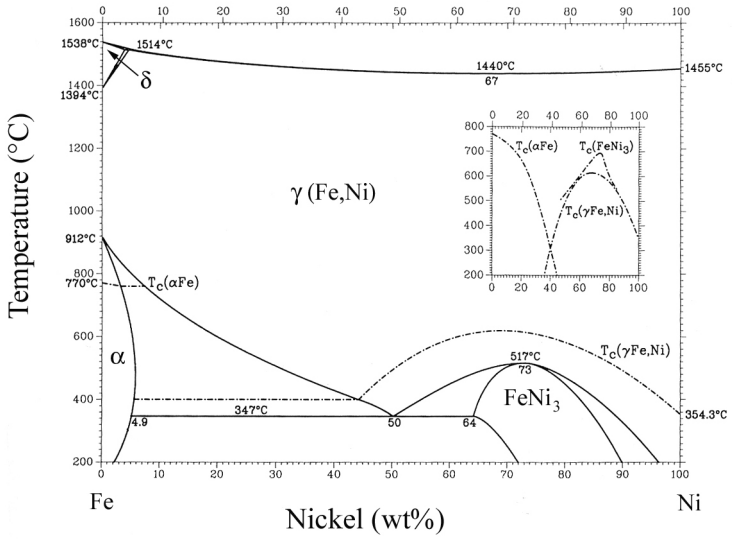

Figure 6. Fe-Ni phase diagram, after [16].

The interesting thermal expansion behavior of Fe-Ni alloys containing roughly 35 wt% Ni was first discovered by Guillaume [28] in 1897. The name "Invar" was coined to indicate that the thermal expansion was invariable with temperature. The material was a curiosity that quickly gained application in precision devices such as balances and time pieces which would benefit from the elimination (or reduction) of thermal expansion related issues. A later paper by Guillaume [29] showed the minimum CTE in the binary Fe-Ni system to be located at 35.6 wt% Ni. The minimum CTE was shown to be strongly influenced by thermal processing (slow cool vs. quench), mechanical processing (i.e. rolling) and the presence of impurity elements.

Much of the attention to the invar alloys was geared toward making the materials more usable in engineering applications. Binary Fe-Ni alloys are relatively weak and exhibit relatively little work hardenability. The additions of alloying elements were studied to a wide extent. This resulted in the discovery of invar-like behavior in other systems (Fe-Ni-Co, for example) with little improvement in the mechanical properties of the Fe-Ni alloys. Study of the Invar behavior continues to the modern day. A recent paper by van

Schilfgaarde *et al.* [30] investigated the invar effect from a quantum mechanical perspective. A review [31] of invar-related work was published in 1978 and remains an excellent compilation and reference on invar alloys.

The invar effect is generally noticeable only at relatively low temperatures. Chevenard [32] showed that the invar behavior effectively disappeared at temperatures above 700 ºC. As shown in Figure 7, the invar effect tends to lessen in magnitude and shift toward higher nickel contents with increasing temperature. Since the interest with these alloys lied with the invar effect, little work was done on the thermal properties at temperatures greater that 700 ºC.

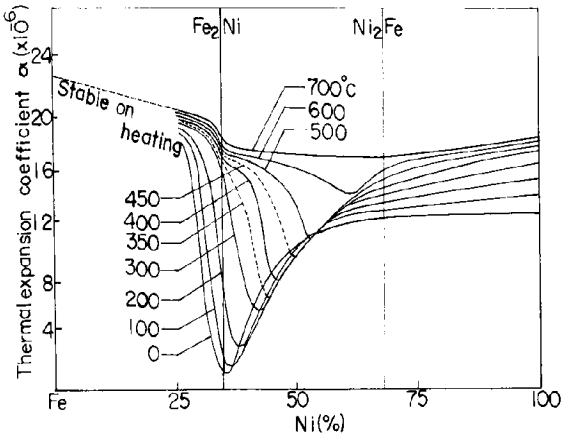

Figure 7. Thermal expansion coefficient vs. composition at various temperatures. Taken from [31] after [28].

The mechanisms which determine the thermal behavior of invar alloys is still a matter of research in solid-state physics [30]. From the discovery of invar by Guillaume, it was believed that magnetism was somehow involved. An early theory [29] postulated the existence of a Fe_2Ni phase which had two states; a low temperature state and a higher

temperature state which was mored dense and rigid. Upon heating from room temperature, there was a gradual change to the more dense state. The tendency of the metal to expand with temperature was countered by the slight contraction resulting from the gradual transformation to a higher density state. Later work in the Fe-Ni system showed that such a Fe_2Ni phase did not exist. A more commonly accepted framework [30] is based on the magnetic susceptibility, magnetic exchange integral, and lattice binding force. The balance between these factors in a Fe-Ni alloy near 35 wt% Ni is such that the magnetic exchange force between atoms compensates to a degree for the binding force change upon heating of the alloy.

If one assumes an average thermal expansion coefficient for the SOFC electrolyte to be $10.5 \cdot 10^{-6}$ K^{-1}, certain Fe-Ni compositions would have a very similar CTE compared to YSZ. As shown in Figure 7, Fe-Ni alloys with roughly 50 wt% Ni have an average CTE of roughly $10 \cdot 10^{-6}$ K^{-1}. As mentioned previously, CTE values alone do not provide a clear picture of thermal expansion behavior. The CTEs of these Fe-Ni alloys change significantly with temperature which makes any comparison using average CTE values only rough approximations which likely contain large errors. Dilatometric studies of Fe-Ni alloys and YSZ would provide raw data from which an accurate comparison of thermal expansion behavior of the respective materials could be made.

Fe-Ni alloys would likely experience severe oxidation when exposed to the operating environment of the SOFC. Oxides of iron and nickel do not form dense, adherent layers that act to slow the diffusion process. On the contrary, oxides of iron (FeO, Fe_3O_4, and Fe_2O_3) are widely known to form non-uniform layers that tend to spall due to the volume change when transitioning from the different valance state in the various oxides. Similarly, NiO does not significantly slow the diffusion of oxygen to the base alloy and

thus does not slow the oxidation process. Because of this, relatively few research programs have examined Ni-Fe based alloys as potential interconnect alloys.

The lack of oxidation resistance of Fe-Ni alloys would generally eliminate them from being used as a SOFC interconnect. However, because of the interesting thermal properties of these alloys and the potential for thermal expansion behavior matching that of YSZ, research into making the alloys more resistant to oxidation may yield new alloys that would exhibit the properties needed for the SOFC interconnect application.

2.7.4 Nickel-Chromium

Chromium has a high solid solubility in nickel as indicated by the Ni-Cr phase diagram, Figure 8, and is an important addition to nickel for high-temperature and corrosion-resistant applications. This system forms the basis for the Inconel and Nimonic series of alloys which consist largely of Ni and Cr along with smaller additions of Fe, Mo, and Ti. These alloys have gained notoriety as "super-alloys" due to their ability to withstand severe operating environments while maintaining high strength.

Nickel-chromium alloys have not received significant attention as potential SOFC interconnect alloys (Yang, *et al.* [33] a notable exception) generally because of the high CTE values observed in this system. In addition, these alloys are generally more expensive than other oxidation-resistant alloys due to the high nickel contents. However, Ni-Cr binary alloys were included in the present work to quantify the impact of chromium additions on the thermal expansion behavior of other systems.

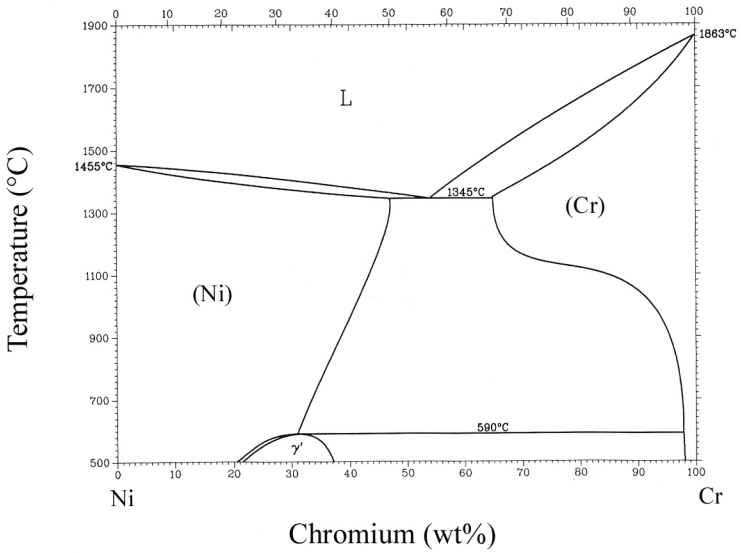

Figure 8. Ni-Cr phase diagram, after [16].

2.7.5 Oxide Dispersions

Dating back to the development of long-lasting tungsten light bulb filaments, additions of small amounts of oxides into a metal matrix have been used to alter specific properties of alloys. Additions of oxides are most commonly used to increase the strength of metal alloys by way of dispersion strengthening. The incorporation of oxides into particular alloys have also been shown to improve oxidation resistance of the base alloy.

Alloys reinforced by second phase particles such as oxides, carbides, or intermetallics offer the potential for superior high-temperature performance. Dispersion-strengthened materials are commonly produced by internal oxidation, rapid solidification, chemical precipitation, or mechanical alloying. These processes and others that are used to make dispersion-strengthened copper have been reviewed by Groza [34]. Similar methods are used to produce dispersion-strengthened alloys in other systems.

The second phase particles used in dispersion-strengthened alloys are typically sub-micron in size and widely dispersed throughout the matrix. At room temperature, the

dispersion-strengthened materials closely resemble precipitation-hardened alloys but the similarity ends with increasing temperature. Precipitation-hardened alloys tend to loose stability at higher temperatures due to phenomena such as particle coarsening and dissolution whereas dispersion-strengthened materials typically exhibit stable structures up to the melting point of the matrix.

A particle to be used in a dispersion-strengthened material should exhibit several characteristics to produce an acceptable final product [35]. The particle should be thermodynamically stable up to the melting point of the matrix to allow the material to be used at high temperatures. The particles should be incoherent with the matrix and form a uniform distribution of fine particle size to provide good high temperature strength and creep resistance. Particles comprised of solute atoms having low diffusivity in the matrix will better resist coarsening at elevated temperatures. The particles should also have a small mismatch in coefficient of thermal expansion with the matrix material to minimize fatigue due to thermal cycling.

The oxide particles in an ODS material can coarsen when exposed to high temperatures. The particle coarsening process is driven by the decrease in total free energy from the reduction in interfacial area per unit volume. Dissolution of smaller particles proceeds along with the growth of larger particles. If the coarsening process is controlled by volume diffusion, the change in particle size (radius) can be calculated by

$$r^3 - r_0^3 = \frac{8\gamma D C_0 t \Omega}{9RT} \tag{2.7}$$

where γ is the surface energy, D is the diffusivity of the particle in the matrix, C_0 is the

concentration of the solute in the matrix near the particle surface, Ω is the partial molar volume, t is time, T is absolute temperature, and R is the gas constant.

The coarsening process results in a simultaneous increase in average particle size and particle spacing. This tends to reduce the strengthening effect of the dispersion. To reduce the coarsening tendency, oxides that have low diffusivity in the matrix are selected for use in a particular alloy.

A dispersion-strengthened alloy with the general properties outlined above would exhibit increased strength as compared to the pure matrix material. The dispersion of fine particles acts as a barrier to dislocation flow. For hard, incoherent particles, the yield stress associated with dislocation bowing (τ_b) is

$$\tau_b = \frac{Gb}{(L-2r)} \tag{2.8}$$

where G is the shear modulus, b is the Burger's vector, L is the inter-particle spacing, and r is the particle radius. Since the quantity *(L-2r)* increases with a coarser structure, strength can be maximized with a fine dispersion of very small particles. The strengthening effect decreases with increasing particle sizes at a constant volume fraction. The effect of the dispersion of particles on the yield strength is given by

$$\Delta\sigma_h = \frac{0.8GbM}{L} \tag{2.9}$$

where $\Delta\sigma_h$ is the increase in yield strength due to the presence of hard particles, M is the

Taylor factor, and the other parameters having been defined previously. From this equation it is again clear that lower particle spacing result in higher strengthening effects. The increase in yield strength due to the strengthening particles is generally additive with other strengthening mechanisms such as the formation of γ' or solid solution strengthening. As an example, a Ni-20Cr alloy has a yield strength of roughly 175 MPa while MA 754 (Ni-20Cr with 1 vol% thoria) has a yield strength of roughly 600 MPa [36].

Tikkanen and Ylasaari [37] investigated the densification of Ni-CaO and Ni-MgO powders. The sample preparation entailed blending NiO and either CaO or MgO, pressing the blended powder into pellets, firing in air at 1200 °C for an unspecified time, reduction in hydrogen at 700 to 850 °C, crushing the pellets, pressing pellets and finally sintering at 1250 °C. With this type of sample preparation, it was expected that the CaO or MgO would form a nearly homogeneous distribution of particles throughout the nickel matrix. No experimental evidence was presented regarding the actual structure of the oxide dispersion.

Tikkanen and Ylasaari were attempting to indirectly link densification with dislocation mobility. It was well understood that a fine dispersion of oxide particles in dense nickel would prevent recrystallization and increase high temperature hardness by pinning dislocations. The authors theorized that any observed reduction in densification due to the presence of the oxide dispersion could also be attributed to the reduction in dislocation mobility. As shown in Figure 9, Tikkanen and Ylassaari showed that the presence of 1 to 5% CaO dispersed in nickel powder greatly reduced densification. By showing this phenomenon, the authors concluded that dislocation mobility was the basic condition for densification in metals.

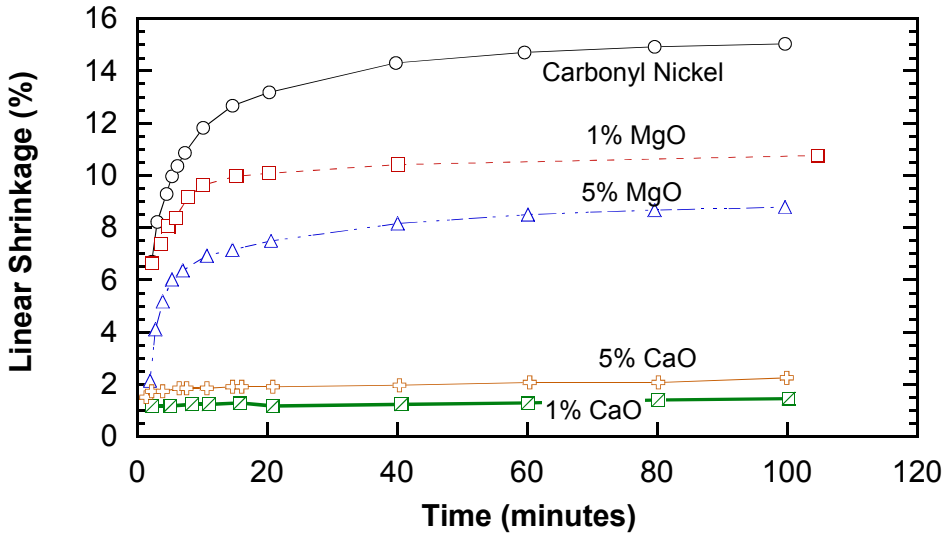

Figure 9. Linear shrinkage of Ni powders with an oxide addition plotted versus sintering time at 1250 °C, after [37].

Similar results were reported by Takahashi, *et al.* [38] for Ni-MgO materials made from the reduction of (Ni,Mg)O solid-solution powder precursors. The presence of the oxide dispersion was shown to limit the degree of densification of the metal powder. Porosity levels after sintering at a given temperature increased with increasing oxide content.

The hardness of the Ni-MgO materials made by the same process were studied as a function of MgO content. As shown in Figure 11, hardness increased with increasing MgO composition as would be expected from the addition of a strengthening dispersoid. The increase in hardness is not particularly significant which may indicate that the MgO is not as potent of a strengthening agent as other oxides such as yttria and thoria. Questions remained as to other mechanical properties such as strength and elongation at elevated temperatures.

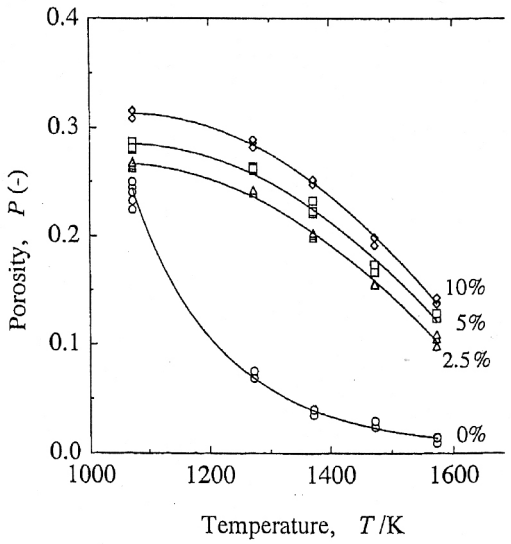

Figure 10. Porosity (volume fraction) as a function of volume percent MgO in Ni and sintering temperature [38].

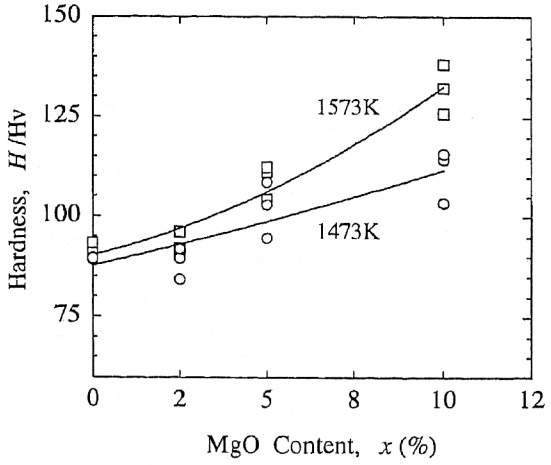

Figure 11. Hardness of Ni-MgO material made from (Ni.Mg)O powder [38].

Oxide dispersions have also been investigated for improving the oxidation resistance of certain alloys. Ramanathan [39] reviewed recent work showing that additions of 1 to 2 vol % or certain oxides such as ceria or yttria to Fe- or Ni-based alloys can improve oxidation resistance. The oxides present in the alloys act to improve the adhesion

of the oxidation layer to the base metal. Additions of Y or Ce (in elemental form) to melts of similar alloys showed a more effective reduction in oxidation rate compared to oxide additions with the same elemental basis. An acceptable mechanism(s) by which the oxides act to improve oxidation resistance has not yet been fully developed. It has been suggested that the oxide addition can promote anionic diffusion through the layer and retard cationic diffusion, oxides tend to accumulate at the scale/metal interface and hence slow cation diffusion, the oxide addition can act as a nucleation site for the oxidation layer. Alternatively, the presence of the oxide is thought reduce the accumulation of voids at the scale/metal interface. While the mechanism is still a matter of debate, the observed improvement of oxidation resistance with the addition of rare-earth elements or their oxides has been well documented.

2.8 Use of Honeycomb Extrusion for Interconnect Research

The hybrid SOFC co-extrusion process described by Rauch was a processing advancement of a similar technique used to make linear cellular alloys, or, metallic honeycomb. The main difference is that the hybrid process uses two materials which are co-extruded into a single structure while the standard honeycomb extrusion process uses a single material. The honeycomb extrusion process has been used to fabricate metallic structures of a variety of alloy compositions [40,41,42] which have been examined for thermal [43] and mechanical [44, 45] applications. It would be expected that metal interconnect alloys made into monolithic honeycomb structures would exhibit properties similar to the same material made into the interconnect layer of a hybrid SOFC. Compared to the hybrid extrusion process, extrusion of a monolithic structure is relatively simple and has been used extensively in past research programs. Also, making many potential

interconnect alloys without the expensive electrolyte layers in the hybrid structure would greatly reduce sample fabrication costs.

Instead of creating the complex hybrid structure, single component extrusions can be made and tested independently for properties such as thermal expansion, sintering characteristics, and oxidation resistance. Potential interconnect alloys that show superior properties can then be incorporated into the more complex hybrid structure for further testing. Also, alloys that are identified as having superior properties for this hybrid SOFC design would likely be applicable to other SOFC designs as well.

The honeycomb extrusion process developed at Georgia Tech is based on the room temperature extrusion of a paste comprised of metal oxides. The extrusion process is similar to the commercial process used to fabricate ceramic honeycomb supports for catalytic converters [46]. A process flow diagram of this technique is shown in Figure 12.

Metal oxides are first blended in a specific proportion to yield a desired alloy composition assuming complete chemical reduction and homogenization during subsequent processing. The oxides are mixed with a common cellulose binder dissolved in water to serve as the fluid phase and processed into a stiff paste using a kneader. The paste is extruded at room temperature using common extrusion equipment and custom-made dies. After the structure is throughly dried, the honeycomb is heat-treated in hydrogen at high temperatures. During the heat-treatment, the metal oxides reduce, sinter, and homogenize to form relatively dense walls. Many complex honeycomb designs have been produced using this method; several examples are shown in Figure 13.

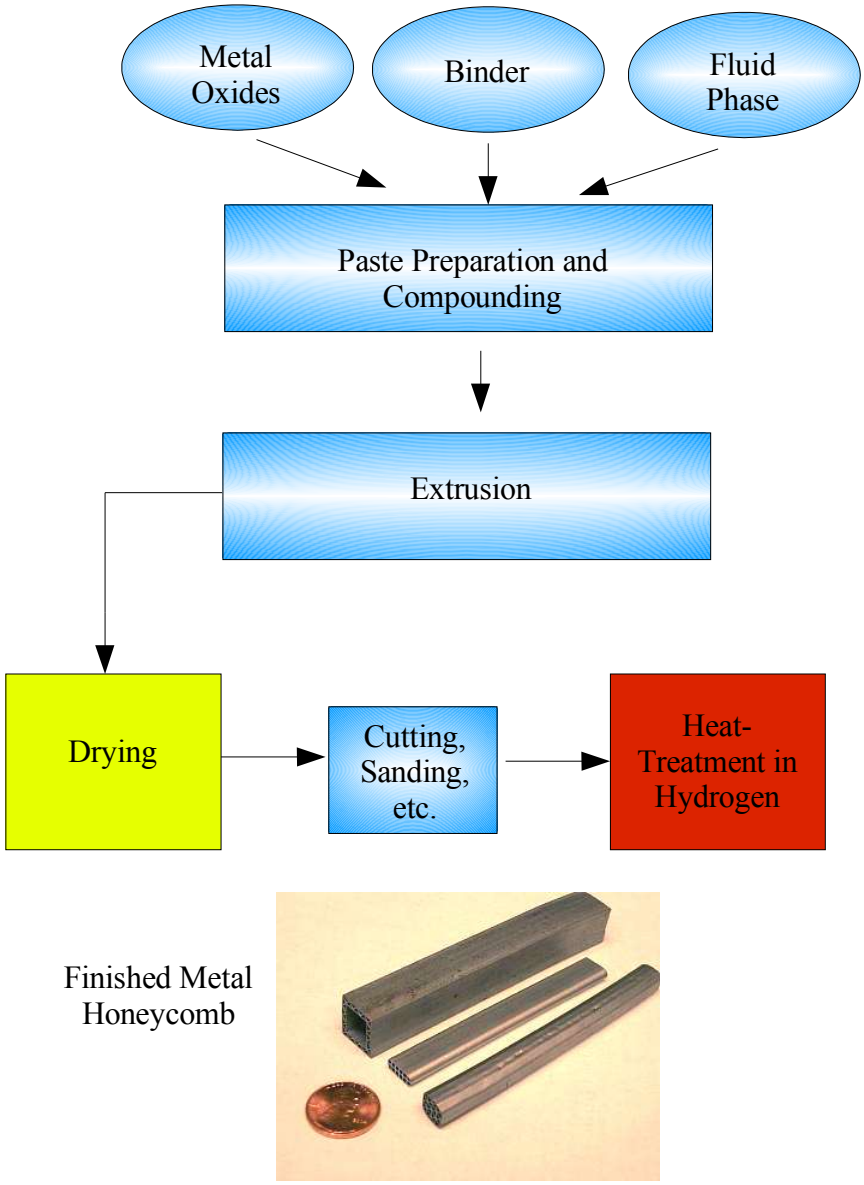

Figure 12. Honeycomb extrusion process flow diagram.

Figure 13. Example of several honeycomb dies used to produce complex honeycomb geometries. Scale at bottom is in cm.

In order to produce a given alloy using the honeycomb extrusion process, the desired metal oxides must be reducible in the high-temperature hydrogen atmosphere heat-treatment used to fabricate these alloys. The reducibility of a given metal oxide as a function of parameters that include temperature and oxygen partial pressure can be ascertained using an Ellingham diagram of the metal oxide in question. These diagrams plot the free energy of formation of the oxide versus temperature and include axes of atmospheric gases that control the oxygen partial pressure. In general, the lower an oxide is on such a diagram, or, the more negative the free energy of formation of the oxide at a given temperature, the more resistant the oxide will be to chemical reduction. An Ellingham diagram of several oxides used in this study is shown in Figure 14 along with lines representing the H_2/H_2O ratio. Ellingham diagrams predict the thermodynamic potential of a given oxide to reduce under certain conditions but do not address kinetics of the potential reaction. When metal oxides are reduced in a mixture with other metal oxides, additional reactions can occur which can act to promote the reduction of a particular

component to an extent not predicted by the Ellingham. Nadler, *et al.* [47] observed the reduction of iron and chromium oxides separately and in mixtures and noted that the reduction of chromium oxide was facilitated by the presence of iron. The chromium would dissolve into the iron matrix and diffuse away from the chromia thereby facilitating the continuation of the reduction reaction. If the metallic iron were not present, the chromium would remain as chromia and act to hinder further reduction.

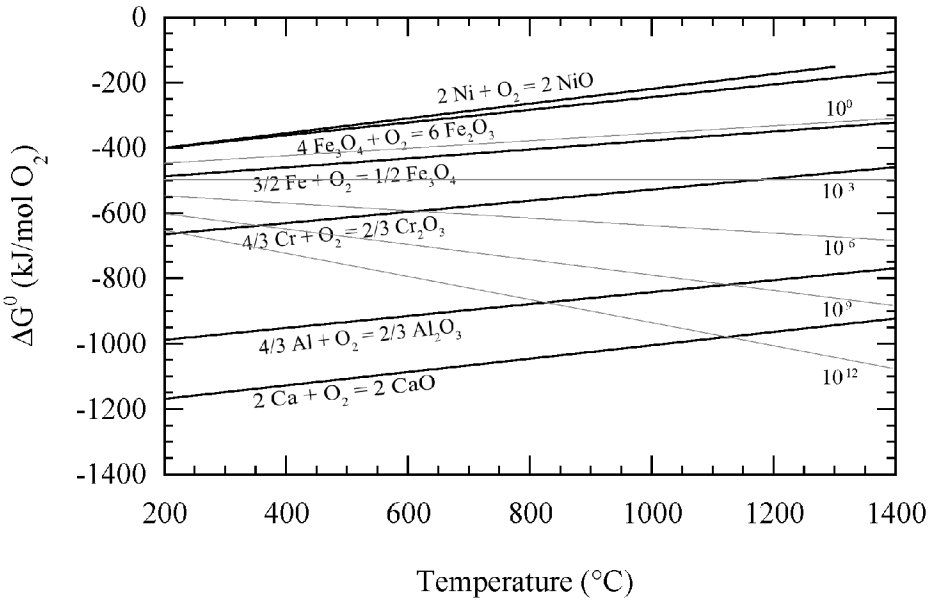

Figure 14. Ellingham diagram for components used in this study. Gray lines represent H_2/H_2O ratio.

The honeycomb fabrication method has distinct advantages compared with traditional methods for producing experimental alloys such as arc-melting of small sample buttons or producing small quantity melts. Both of these traditional techniques rely on the availability of high-purity metals or alloys with tightly controlled compositions; such materials tend to be expensive and not widely available. Also, the equipment necessary to

melt, cast, and mechanically form a wrought alloy is expensive and potentially hazardous to inexperienced users. Arc-melting equipment, while generally easy and safe to use, generally produces small batch sizes and samples with small dimensions. Machining standard or sub-standard sized tensile bars from an arc-melted sample may simply not be possible. These limitations are not present with the honeycomb extrusion process. Metal oxides are generally available in high-purity grades and various particle size ranges. The equipment needed for processing is widely used in ceramic processing and is easily obtained. Honeycomb extrusions can be produced to nearly any desired length, facilitating the fabrication of long samples needed for CTE or tensile testing. With the exception of the reduction heat-treatment, the honeycomb extrusion process is carried out at room temperature. The combination of these features makes the honeycomb extrusion process a promising alternative for the fabrication of experimental alloy compositions.

3. Experimental Procedure

3.1 Fabrication of Alloy Honeycomb Samples

Metal oxides [Fe_2O_3 (Pea Ridge, 2-8 μm, 99.7%), NiO (Ceramic Color, 6 μm, 99.9%) and Cr_2O_3 (Fisher Scientific, 2-5 μm, 99.9%)] were mixed in proportion to produce the desired alloy compositions after complete reduction. The metal oxide powders were first dry-mixed with Methocel A4M (Dow Chemical), which acts as a binder when hydrated. A solution of deionized water with 2.5 wt% Pegosperse 100S (Lonza), a lubricant, was then added to the dry powder mixture in a commercially available food blender. Solids loading was kept constant at 50.5 vol% for each composition. An example batch is shown in Table 1.

Table 1. Batch composition for Ni 40 Fe 10 Cr (reduced composition, in wt%) at 50.5 vol% solids.

Ingredient	***Amount (g)***
Fe_2O_3	506.8
Cr_2O_3	129.5
NiO	563.7
Methocel A4M	53.4
Water 2.5 wt% Pegosperse	158.7

A granulated powder mixture was produced after mixing for 30 s in a food blender. Next, the granulated powder was pugged in a Buss kneader to form a homogeneous paste. The paste was then formed into a honeycomb structure using a Loomis extruder and custom-made extrusion dies of various cross-section. Figure 15 shows the extrusion dies used in this work. The extrudate was allowed to dry at room temperature for a minimum of 24 h.

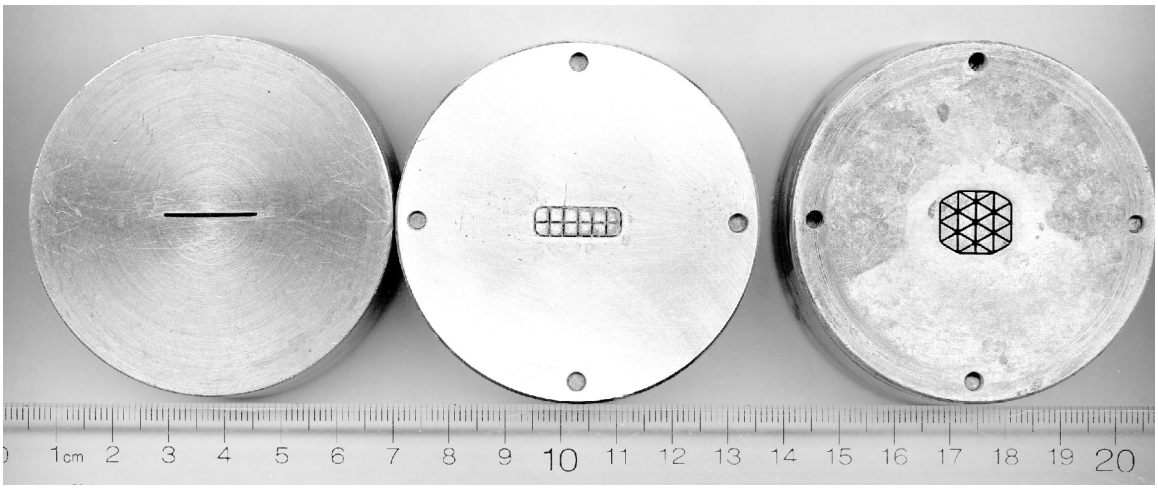

Figure 15. Extrusion dies used to produce A) Flat strip, B) 2 x 6 square cell, and C) Octagonal samples. Scale shown is in cm.

All samples were heat-treated in a resistance tube furnace, Figure 16, with a hydrogen atmosphere. The temperature was controlled using a feedback loop from a thermocouple junction placed in the center of the tube in close proximity to the samples. Sample temperature was assumed to be the same as the furnace temperature as measured using the control thermocouple. A programmable furnace was used to acheive specific heating schedules and hold times. Unless otherwise stated, heat-treatments were performed by heating at 2 ºC/min from room temperature to 1100 ºC and then 1 ºC/min to 1300 ºC.

Samples were held at 1300 ºC for 10 h. Cooling was controlled using rates and temperatures identical to the heating cycle.

Prior to the initiation of the heat-treatment, the furnace chamber was purged to approximately 1 torr followed by backfilling with ultra-high purity (UHP) (99.9999%) hydrogen. The purge/backfill cycle was repeated two additional times. The UHP hydrogen was then flowed continuously throughout the heat-treatment cycle at a flow rate of 0.5 l/min. Exhaust from the furnace was passed through a bubbler filled with glycol before being sent to a fume hood. The bubbler provided a slight positive pressure inside the furnace tube and also prevented the back-diffusion of air from the exhaust line.

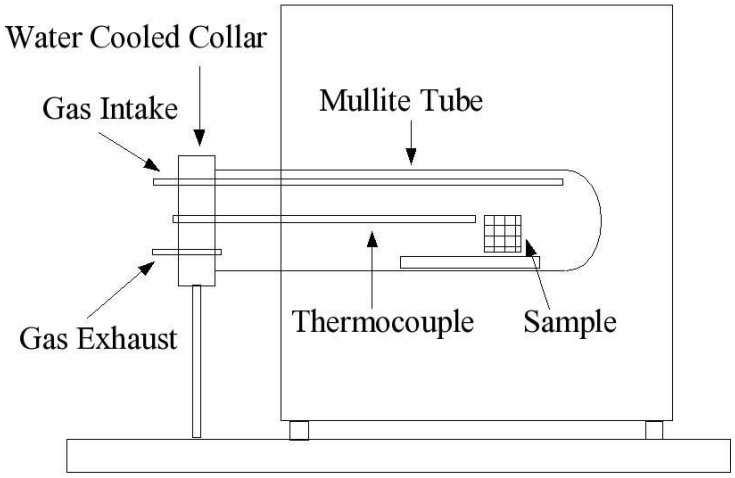

Figure 16. Schematic of the close-ended 101 mm outer diameter tube furnace used for hydrogen reduction.

3.2 Fabrication of YSZ Honeycomb

Honeycomb made of 8 mol% yttria-stabilized zirconia was formed using the same

process as that for metal alloy honeycomb with the exception that the solids content was 40% and sintering was carried out in static air in a bottom loading $MoSi_2$ resistance element furnace.

3.3 Fabrication of ODS Alloy Samples

Additions of Y_2O_3 were added to the other metal oxides during the dry-mixing stage. After extrusion and drying, these samples were processed identically as alloy samples without a yttria addition.

Samples containing CaO were made using paste preparation and extrusion techniques described earlier. Powdered $Ca(OH)_2$ was added to the metal oxide powders to create the desired composition of CaO in the metal after oxidation of the $Ca(OH)_2$ and reduction of the metal oxides. After the samples were extruded and dried, select samples were heat treated in air. The purpose of this heat treatment was to first oxidize the $Ca(OH)_2$ to CaO and second to create a solid solution. For example, in the case of Ni-CaO, the heat-treatment in air would dissolve the CaO into the NiO thereby producing a (Ni,Ca)O solid solution. Samples heat treated in air have been termed "solutionized". The heat-treatment in air was performed in a bottom loading $MoSi_2$ element resistance furnace in static air. The heating and cooling rates were both fixed at 5 ºC/min and the samples were held at 1500 ºC for 2 hours. Solutionized and non-solutionized samples were reduced and sintered in hydrogen using a resistance tube furnace as described previously for the metal alloy honeycomb.

3.4 Thermal Expansion

Honeycomb samples were cut from green 2x6 cell extrusions prior to reduction to form a 2x3-type cell structure, as shown in Figure 17. After reduction, the samples were cut to length (34.7 mm, typical) and ground to ensure parallel ends. Dilatometry experiments were performed in a dual pushrod dilatometer using alumina pushrods and a sapphire reference. A flowing argon atmosphere was used to prevent excessive oxidation of the samples. Three pump-down / backfill cycles were performed prior to each run. All experiments used a 3 °C/min heating rate up to 1300 °C. Data were typically not collected during cooling. Sample temperature was measured and recorded using a thermocouple junction floating roughly 1 mm above the sample.

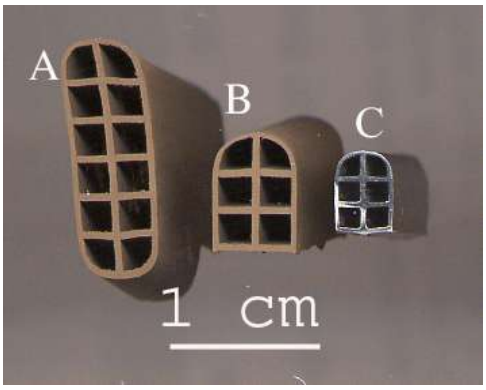

Figure 17. Cross-sections of dilatometry samples A) as-extruded and dried, B) cut into 2x3 cell geometry, and C) as-reduced.

The coefficient of thermal expansion (CTE), α_T, was calculated from the displacement versus temperature data and is given in Equation 3.1

$$\alpha_T = \frac{dl/l_0}{dT} = \frac{1}{l_0}\frac{dl}{dT} \tag{3.1}$$

where T is temperature in °C, l_0 is the length at room temperature, and l is the length at a given temperature. It should be noted that the values of α_T may vary from other calculated values of CTE, as has been described recently by James, *et al*. [48]. With the raw dilatometer data of $\Delta l/l_0$ versus T, the value of α_T was calculated by a linear regression over small temperature intervals as shown in Equation 3.2,

$$\alpha_T = \frac{n\sum x_i y_i - \sum x_i \sum y_i}{n\sum x_i^2 - \left(\sum x_i\right)^2} \tag{3.2}$$

where x_i represents a T datum point, y_i represents a $\Delta l/l_0$ datum point, and n is the range over which each regression is performed. The value of $n = 41$ was used in all calculations which roughly equates to a 20 °C temperature range. A more detailed discussion on the selection of this particular interval value is provided in the appendix. The value of α_T calculated for each regression was assigned to the median temperature for each particular regression range. A different CTE over a specific temperature range was calculated using Equation 3.3.

$$\alpha_M = \frac{1}{l_0}\frac{\Delta l}{\Delta T} \tag{3.3}$$

The value of α_M is more commonly reported than α_T and can generally be considered as the average or mean CTE value over a specified temperature range. In this work, all values of α_M are based on a reference temperature of 20 °C unless otherwise specified.

The thermal expansion mismatch, $\Delta E_{T,\,\text{heating}}$, between an alloy and YSZ upon heating from the zero-mismatch point of room temperature to a temperature T was calculated from the raw expansion data using Equation 3.4.

$$\Delta E_{T,\text{heating}} = \left[\frac{\Delta l}{l_0}\right]_{\text{metal},T} - \left[\frac{\Delta l}{l_0}\right]_{\text{YSZ},T} \tag{3.4}$$

The thermal expansion mismatch between an alloy and YSZ from a zero-mismatch

temperature of T_S (600 or 1100 °C) to a lower temperature T was calculated from Equation 3.5.

$$\Delta E_{T,\text{cooling}} = \left(\left[\frac{\Delta l}{l_0}\right]_{\text{metal},T} - \left[\frac{\Delta l}{l_0}\right]_{\text{metal},T_s}\right) - \left(\left[\frac{\Delta l}{l_0}\right]_{\text{YSZ},T} - \left[\frac{\Delta l}{l_0}\right]_{\text{YSZ},T_s}\right) \qquad (3.5)$$

Equation 3.5 is based on the assumption that there is a zero-stress state between the metal and YSZ at T_S due to plastic flow in the metal at all higher temperatures.

The Curie temperature was measured from α_T versus temperature plots of the respective alloys. A typical example is shown in Figure 18. Lines were first drawn to extend the near-linear portions of the CTE curve. The temperature at which these lines intersected was defined as the Curie Temperature. Phase transformation temperatures were determined using a similar technique but were based on thermal expansion versus temperature plots.

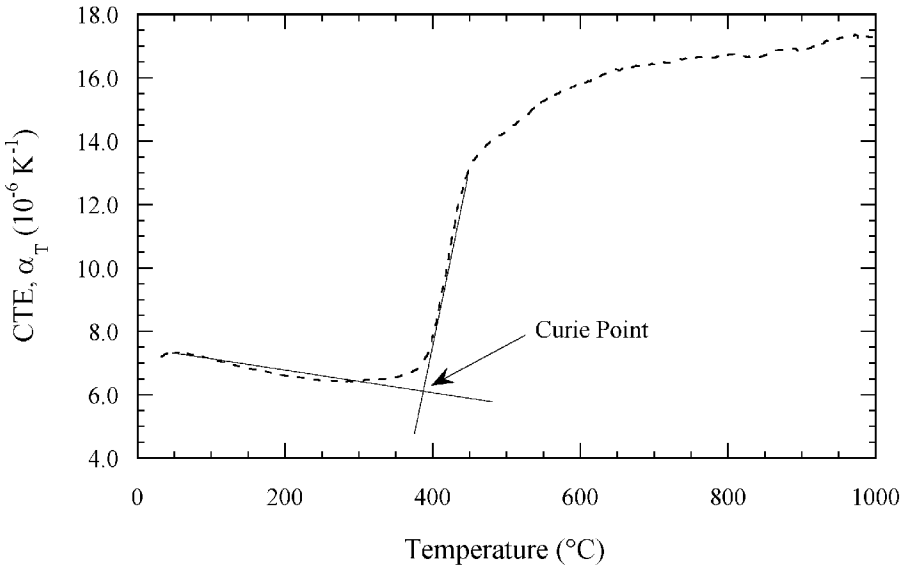

Figure 18. Example showing the method for determination of the Curie temperature.

3.5 Oxidation

Oxidation studies were performed using a resistance box furnace in static air. Samples in the form of rectangular strip were placed on alumina cards and set inside a pre-heated furnace set to 700 °C. Samples were removed periodically from the furnace to take weight measurements. Sample weight was measured using a Denver Instruments scale with resolution of 0.01 mg. All oxidation samples analyzed for weight gain were processed during one experiment to assure that each sample was exposed to identical conditions.

3.6 X-Ray Diffraction

X-ray diffraction (XRD) data were taken using a Philips PW1800 diffractometer with Cu K_α radiation. Scans of lattice parameter samples were performed in a step-wise procedure using 0.02 °2θ steps with a 2.5 second hold at each position. After $K_{\alpha 2}$ stripping, the 2θ peak positions were determined using software which used least-square fits of the XRD data to Gaussian functions. Lattice parameter measurements were made using the Nelson-Riley method [49]. This method uses linear extrapolation techniques and is based on the assumption that the lattice parameter varies linearly with

$$f(\theta) = \frac{1}{2}\left(\frac{\cos^2\theta}{\sin\theta} + \frac{\cos^2\theta}{\theta}\right) \tag{3.6}$$

For each peak position, a lattice parameter value, *a*, is calculated using

$$a = \frac{\lambda}{2} \frac{\sqrt{h^2+k^2+l^2}}{\sin\theta} \tag{3.7}$$

where *h*, *k*, and *l* represent the crystallographic plane associated with the particular peak and λ is the wavelength of the incident x-rays. The lattice parameter is then taken to be the intercept of $f(\theta)$ (also referred to as the Nelson-Riley parameter) with the y-axis on a *a* vs. $f(\theta)$ plot.

The accuracy of the Nelson-Riley method is generally considered to be 1 part in 100,000. A simple method was created to estimate the relative error associated with the lattice parameter calculation taken from the different XRD scans. Figure 19 shows a Nelson-Riley plot for two samples. It can be seen that the Fe 75 wt% Ni sample has a smaller deviation, or R^2, when calculating a linear curve fit. The assumption made was that a smaller R^2 value would in turn result in less certainty in the calculated a_0 value. The following equation was used as an estimate of the experimental deviation range in the a_0 calculation.

$$\text{Error} = \pm 1.96 \left(\frac{\sum |a_i - a_0|}{n^{1.5}} \right) \tag{3.8}$$

where a_0 is the calculated lattice parameter, a_i is the lattice constant for each particular diffraction peak, and *n* is the number of data points. Equation 3.8 is a modified form of a statistical method for determining 95% confidence intervals from data sets.

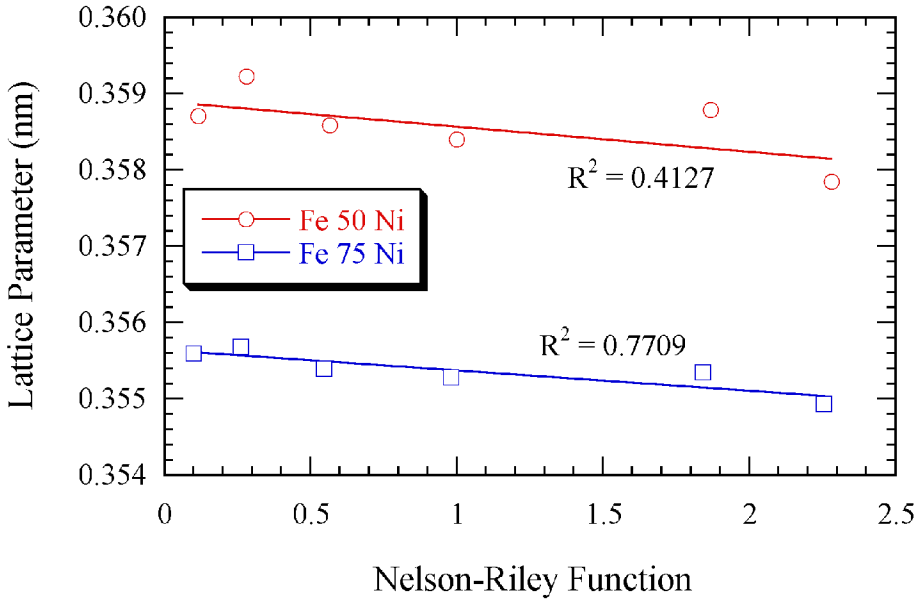

Figure 19. Example Nelson-Riley plots for two samples showing the difference in the quality of the linear regression.

It should be noted that this was used simply as a tool to indicate how well the linear curve-fit regression line approximated the data points of the Nelson-Riley calculation. In other words, the estimation provided a way to compare the potential error in lattice parameter from different XRD scans based on the quality of the initial pattern. This method was thought to be superior to using R^2 because this estimated error range could be used to estimate the error in composition as well.

The accuracy of each scan was also verified by including an internal silicon standard in each sample. Variations of lattice parameter calculations of the silicon, calculated using the method outlined previously, were in the fifth place after the decimal in nm units for each sample tested. The above method for estimating error of the lattice parameter was not applied to the silicon measurements because the Si scans showed remarkable sample to sample consistency in linear curve-fit deviation.

Lattice parameters of γ Fe-Ni samples were converted to composition based on lattice parameter data taken from Pearson [50], plotted in Figure 20.

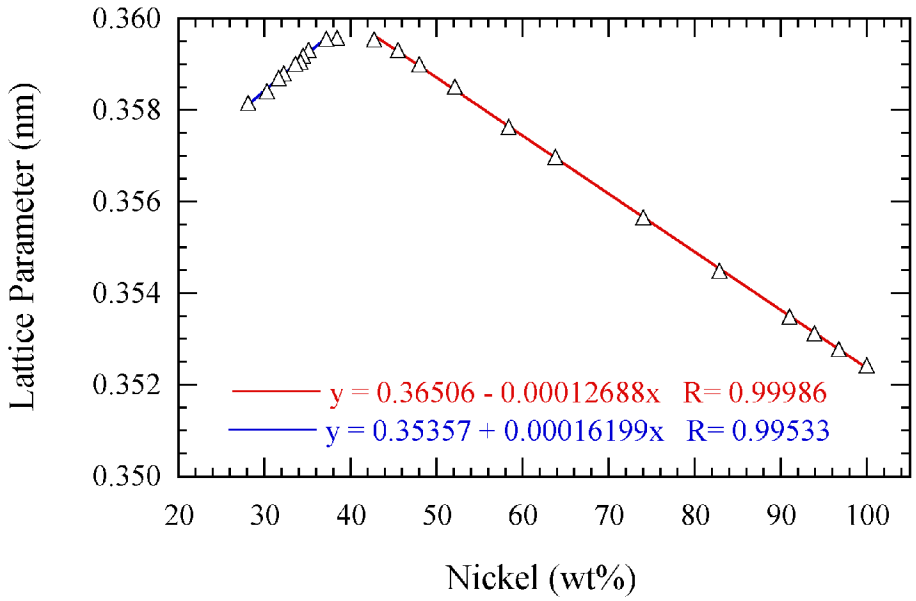

Figure 20. Lattice parameter data for γ Fe-Ni taken from Pearson [48].

Two linear regions were assumed and conversion equations obtained from linear regression. These conversion equations were

$$C = -2162 + 6115.6 \cdot a, \quad 28 < C < 38 \text{ wt\% Ni} \tag{3.9-a}$$

$$C = 2862.12 - 7838.8 \cdot a, \quad 43 < C < 100 \text{ wt\% Ni} \tag{3.9-b}$$

where C is composition in wt% Ni and a is lattice parameter in nm. Since for certain lattice parameters one could calculate two acceptable compositions, it was assumed that the as-batched composition was sufficiently accurate to act as a guide in selecting the appropriate conversion equation. For example, given an as-batched composition of Fe 40 wt% Ni, only

Equation 3.9-b would be used to convert the calculated lattice parameter into a composition.

Scans of oxidation samples for the purpose of oxidation layer phase identification were performed using the same equipment although using different scan parameters. For this situation, scans were continuous at a scan rate of 0.025 °2θ/s. Phase identification scans also utilized Cu K_α radiation and $K_{\alpha 2}$ stripping was performed prior to analysis of the pattern.

3.7 Optical and Scanning Electron Microscopy

Optical microscopy samples were prepared using standard metallographic techniques. When mounting was necessary, samples were hot mounted in phenolic resin. Grinding and sanding were performed with SiC paper of various grits. Polishing was performed using 1 μm alumina suspended in water. Final polishing was done with either 0.5 μm alumina or 0.05 μm silica. Prepared samples were observed using a Leica BM IMR optical microscope with digital image capture capability.

Scanning electron microscopy (SEM) samples were prepared in the same manner as previously described with the exception that a carbon-doped phenolic resin was used for hot mounting. This was done to facilitate grounding of the sample in the microscope. A Hitachi S-800 field emission SEM with energy dispersive spectrometry (EDS) was used for analyzing SEM samples.

3.8 Density and Porosity

Density measurements were made using the Archimedes method. Samples were

first weighed in dry air (W_D), then placed in distilled water and set in a vacuum for ten minutes. The saturated samples were then weighed while suspended in distilled water (W_{SS}). The samples were then weighed after having surface water removed with a damp tissue, thereby providing the saturated weight (W_S). Using these three values, the bulk (ρ_{Bulk}) and apparent ($\rho_{Apparent}$) densities could be calculated using the following equations, respectively:

$$\rho_{\text{Bulk}} = \frac{W_D}{W_S - W_{SS}} \tag{3.10}$$

$$\rho_{\text{Apparent}} = \frac{W_D}{W_D - W_{SS}} \tag{3.11}$$

The porosity of the samples could also be calculated using these same data. Open porosity, ε_O, is defined as porosity that is open to the surface of the sample. Closed porosity, ε_C, is porosity that is isolated from the surface of the sample.

$$\epsilon_O = \frac{W_S - W_D}{W_S - W_{SS}} \tag{3.12}$$

$$\epsilon_C = 1 - \left[\frac{1}{\rho_{th}}\left(\frac{W_D}{W_D - W_{SS}}\right)\right] \tag{3.13}$$

where ρ_{th} is the theoretical density. The total porosity of the sample, ε_T, could then be calculated by

$$\epsilon_T = \epsilon_O - \epsilon_C \tag{3.14}$$

The percent theoretical density could then be calculated by

$$\text{TD}\,(\%) = (1 - \epsilon_T) \times 100 \tag{3.15}$$

It should be noted that the W_S measurement could not be made for honeycomb samples since it was exceedingly difficult to remove surface water from the inner channels of the fine extrusions in a consistent manner. Density values reported in this work originated from strip samples unless otherwise specified.

Porosity measurements were also made using metallographic techniques. Polished and unetched samples were observed in a Leica BM IMR light microscope and a digital image taken. The digital image was then processed using a program called GNU Image Manipulation Program (GIMP) version 2.0. The image was first thresholded to make the image black and white as opposed to gray-scale. The porosity was calculated by measuring the area fraction of pores in the image using the Histogram function in the software. This function would simply sum the pixel values of the image by category. For the case of a black and white image, summing the pixels with a color value of zero and dividing by the total pixels in the image would equate to measuring the area fraction of pores in the image. This area fraction is equivalent to the volume fraction of pores (ε_T) when a randomly oriented pore structure is assumed.

3.9 Mechanical Properties

Extruded strips were cut into dog-bone shapes, Figure 21, using a "cookie-cutter" die prior to the reduction heat-treatment. All samples were reduced in pure hydrogen and sintered at 1300 °C for 10 h. The as-reduced sample dimensions (gage length and cross-section) were measured using a standard caliper prior to testing.

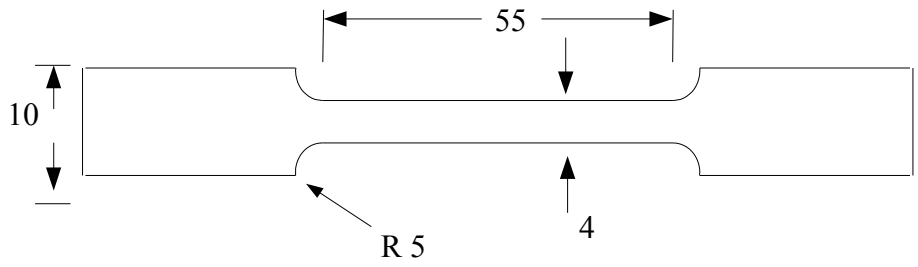

Figure 21. Schematic of the die used to cut tensile samples from green strip (dimensions in mm).

Tensile tests were performed on a standard screw driven frame with a rate of 0.1 in/min. All tests were performed at room temperature. Load was measured using a 1000 lb load cell. Data of load and displacement were collected by the test frame control computer. Elongation was determined by measuring initial and final gage length directly from the sample.

4. Results and Discussion

4.1 Lattice Parameter Measurements

Producing metals directly from oxide precursors may be problematic if complete chemical reduction and homogenization are not achieved. If the sample were homogenized poorly, an XRD pattern taken from the sample would tend to have broad peaks indicating a compositional variation. In addition, a larger error would be expected in calculated lattice parameter values.

Lattice parameter calculations were made from XRD data taken using flat strip samples of various Fe-Ni compositions to compare the experimental values to literature data. Figure 22 shows the calculated lattice parameter results along with literature data taken from Pearson [50]. The x-axis values of composition for the experimental data were taken to be the intended batch composition. The experimental lattice parameter values agreed very well with the literature data. It should be noted that the XRD scans for the various compositions all had similar diffraction peak widths. If, for example, the peak widths for a binary sample were systematically broader than that for a single component sample, it could be inferred that peak broadening could be the result of a chemically non-homogeneous structure. Since the peak widths for the different samples were all similar, it appeared that each sample was well homogenized after the 10 h heat-treatment in hydrogen at 1300 °C.

Of the Fe-Ni samples tested using XRD, all were observed to be single-phase austenitic (γ) Fe,Ni with the exception of the Fe 30 wt% Ni sample which showed trace amounts of the ferritic (α) phase. The γ to α transition temperature for a Fe 30 wt% Ni alloy was shown by Jones and Pumphrey [51] to be approximately 50 °C, and decreased with increasing nickel content. This makes the presence of the ferritic phase improbable in alloys prepared in this work containing greater than 30 wt% Ni.

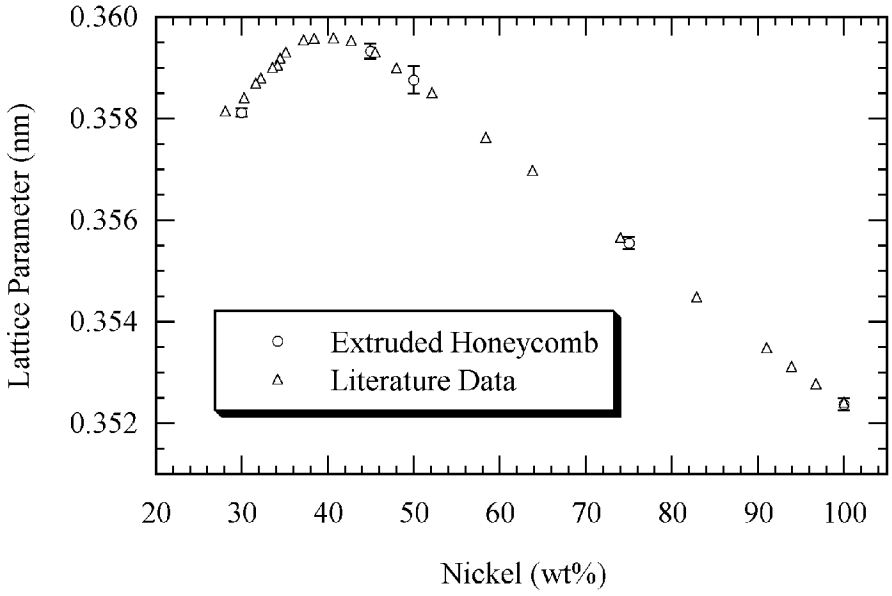

Figure 22. Calculated lattice parameter for extruded Fe-Ni samples compared with literature data.

Additional lattice parameter calculations were made from Fe-Ni-Cr ternary strip samples. Starting with a Fe 50 wt% Ni base alloy, chromium was added in three ways: maintaining a constant Fe content, constant Ni content, and a constant iron-to-nickel ratio. Comparison literature data could not be found for these specific Fe-Ni-Cr alloy compositions. The lattice parameter, Figure 23, was found to vary slightly with chromium

content and Fe/Ni ratio at a given Cr composition.

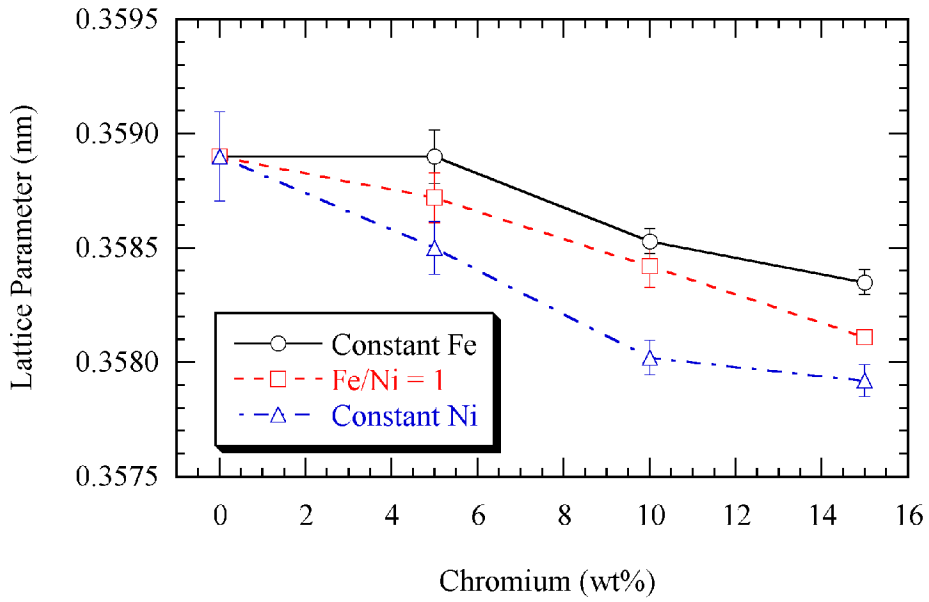

Figure 23. Lattice parameter of Fe-Ni-Cr alloys based on Cr additions made to a Fe 50 wt% Ni base alloy.

Table 2 compares the intended composition to that calculated from the lattice parameter measurements of γ Fe-Ni alloys. The calculated compositions deviated from the intended compositions by no more that 0.4 wt% Ni and tended to be accurate to within 0.1 wt% Ni. The calculated composition ranges fell within +/- 1.1 wt% or less of the intended value when experimental error in the lattice parameter measurement was considered. The error range was a result of potential error in the lattice parameter which was estimated using Equation 3.8. This result implies that the process by which the alloy honeycomb are made can be used to produce specific compositions accurately. Another consideration would be the potential for compositional variation between batches of extruded material. While not systematically studied for all compositions, limited data suggest there is very

little variation in properties from batch to batch.

Table 2. Intended compositions of alloys made from reduced metal oxides and compositions calculated by converting lattice parameter measurements to composition using literature data [50]. Composition ranges are a result of potential error in the lattice parameter measurements.

Sample	Intended Composition (wt% Ni)	Calculated Composition and Range (wt% Ni)
Fe 30 Ni	30	28.6*
Fe 45 Ni	45	45.4 +/- 0.6
Fe 50 Ni	50	49.9 +/- 1.1
Fe 75 Ni	75	75.0 +/- 0.5
100 Ni	100	99.9 +/- 0.5

*A Ferritic Fe-Ni phase was also detected in the XRD pattern.

Another example of composition control is exemplified by observing the thermal expansion behavior of two Fe-Cr alloys. The Fe-Cr system contains a γ to α phase transition for alloys containing less than roughly 12 wt% Cr (see Figure 4). Figure 24 shows the thermal expansion behavior of Fe 10 wt% Cr and Fe 12 wt% Cr. It can be seen that the Fe 10 wt% Cr alloy goes through the γ to α transition, signified by the sharp contraction in sample length at roughly 900 °C. The Fe 12 wt% Cr alloy does not go through any phase change upon heating. If the composition control were poor, it would be possible that either the Fe 10 wt% Cr alloy would not have shown then phase transformation or that the Fe 12 wt% Cr alloy would have shown the phase transformation. The fact that the thermal expansion behavior of these two samples with similar compositions both displayed the expected behavior reinforces the position that composition can be controlled to a high degree with this fabrication technique. Naturally, this serves not as proof but as an indication of composition control.

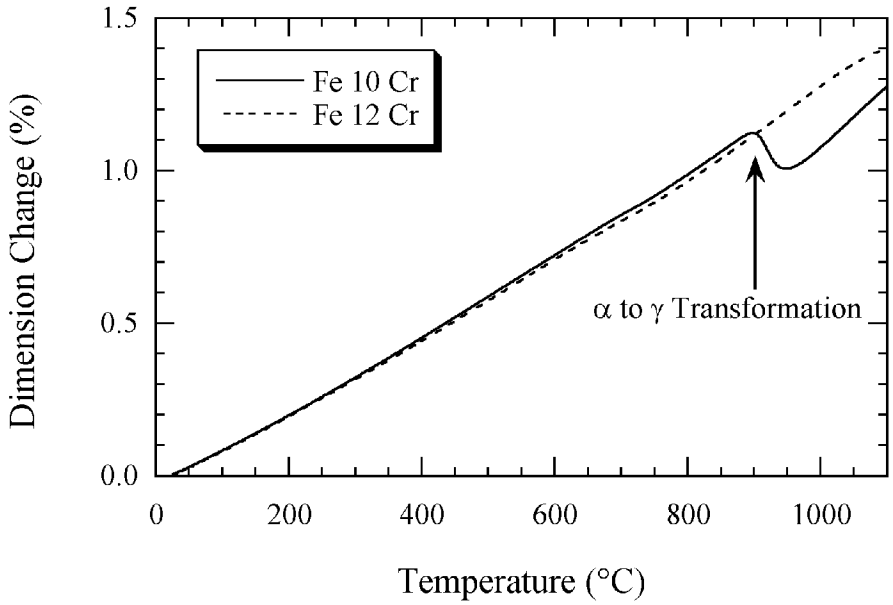

Figure 24. Linear expansion of Fe 10 and 12 wt% Cr showing the α to γ transformation for the Fe 10 wt% Cr sample.

While a full systematic study examining the ability to produce precise batch compositions reproducibly was not performed, these data provide initial evidence that this process can be used to produce a given desired alloy composition. This becomes particularly important when considering the variability of certain material properties, such as thermal expansion, with slight (~ 1 wt%) changes in composition. The particular sensitivity of thermal expansion behavior with composition will be discussed in detail for the case of Fe-Ni alloys in a later section.

Many studies of potential SOFC interconnects rely on the availability of commercial alloys [57, 18, 20, 21, 22] which tends to limit the ability of researchers to explore a wide range of compositions in a given system. A select few studies have used samples produced in-house by means of vacuum induction melting and subsequent hot forging of ~ 10 kg melts [19] or arc-melting of small buttons for oxidation tests [23]. The

honeycomb extrusion process used in this work is relatively simple, rapid, cost-effective and allows the researcher to produce a wide range of compositions including Fe-Ni, Fe-Cr [47], and Fe-Ni-Cr, among others. The primary limitation of this fabrication technique is the inability to incorporate low nobility elements such as Al, Mg, or Si.

4.2 Density and Porosity

Density and porosity measurements were performed using the Archimedes method with flat strip specimens weighing roughly 1 g in the as-reduced condition. The experimental error for an average porosity measurement was estimated to be ± 1% based on the resolution of the scale (0.001 g) used for these tests.

The as-reduced density and porosity data for Fe-Cr, Fe-Ni, Ni-Cr, and Fe-Ni-Cr alloys after heat-treatment in hydrogen at 1300 °C for 10 h are shown in Tables 3, 4, 5, and 6, respectively. The majority of samples were well-sintered and primarily contained closed porosity which is common for materials made with the oxide extrusion process with greater that 92% theoretical density [52].

The addition of chromium tended to increase porosity in the majority of Cr-containing samples. Chromium oxide was shown [27] to resist reduction until relatively high temperatures are reached in the heat-treatment cycle which can explain the general trend of increased porosity with increasing chromium content. The presence of an inert (at that temperature) oxide in the metal would act to hinder densification [53]. Also, if the chromia particles were to reduce at a point in the heat-treatment after the other oxides had fully reduced and were mostly sintered, the contraction of the chromia upon reduction would cause a local increase in porosity by forming pores adjacent to the chromia particle. If these pores were fairly large, impractically long hold times may be needed to eliminate

this porosity. Density and porosity values did not vary significantly within the Fe-Ni system and there was no apparent trend between as-reduced density and composition. Total porosity as a function of chromium content for Fe-Ni-Cr alloys is shown in Figure 25.

Table 3. Density and porosity of Fe-Cr alloys.

Composition (wt%)	Density (g/cm^3)			Porosity (vol%)		
	Theoretical	Bulk	Apparent	Closed	Open	Total
100 Fe	7.87	7.34	7.34	6.67	0.00	6.67
Fe 5 Cr	7.83	7.30	7.47	4.63	2.29	6.92
Fe 10 Cr	7.80	7.51	7.60	2.49	1.19	3.68
Fe 15 Cr	7.76	7.46	7.58	2.38	1.49	3.87
Fe 20 Cr	7.72	7.12	7.19	6.86	1.01	7.87

Table 4. Density and porosity of Fe-Ni alloys.

Composition (wt%)	Density (g/cm^3)			Porosity (vol%)		
	Theoretical	Bulk	Apparent	Closed	Open	Total
100 Fe	7.87	7.34	7.34	6.67	0.00	6.67
Fe 36 Ni	8.24	7.85	7.95	3.57	1.23	4.80
Fe 40 Ni	8.29	7.85	7.92	4.42	0.93	5.35
Fe 45 Ni	8.34	7.97	8.11	2.68	1.80	4.48
Fe 50 Ni	8.39	7.90	7.99	4.72	1.23	5.95
Ni 60 Fe	8.49	8.14	8.26	2.76	1.40	4.16
Ni 75 Fe	8.65	8.32	8.36	3.37	0.50	3.87
100 Ni	8.91	8.68	8.68	2.61	0.00	2.61

Table 5. Density and porosity of Ni-Cr alloys.

Composition (wt%)	Density (g/cm^3)			Porosity (vol%)		
	Theoretical	Bulk	Apparent	Closed	Open	Total
100 Ni	8.91	8.68	8.68	2.61	0.00	2.61
Ni 5 Cr	8.82	8.66	8.66	1.79	0.00	1.79
Ni 10 Cr	8.73	8.31	8.31	4.89	0.00	4.89
Ni 15 Cr	8.64	8.15	8.15	5.71	0.00	5.71

Table 6. Density and porosity of Fe-Ni-Cr samples.

Composition (wt%)	Density (g/cm^3)			Porosity (vol%)		
	Theoretical	Bulk	Apparent	Closed	Open	Total
Fe 45 Ni 5 Cr	8.30	7.72	7.79	6.20	0.83	7.03
Fe 40 Ni 10 Cr	8.21	7.55	7.60	7.44	0.75	8.19
Fe 35 Ni 15 Cr	8.13	7.37	7.51	7.52	1.95	9.47
Fe 47.5 Ni 5 Cr	8.33	7.65	7.74	7.03	1.21	8.24
Fe 45 Ni 5 Cr	8.27	7.49	7.57	8.39	1.12	9.51
Fe 42.5 Ni 15 Cr	8.20	7.48	7.61	7.17	1.82	8.99
Ni 45 Fe 5 Cr	8.35	7.73	7.79	6.74	0.74	7.48
Ni 40 Fe 10 Cr	8.32	7.48	7.60	8.56	1.62	10.18
Ni 35 Fe 15 Cr	8.28	7.40	7.56	8.74	2.10	10.84

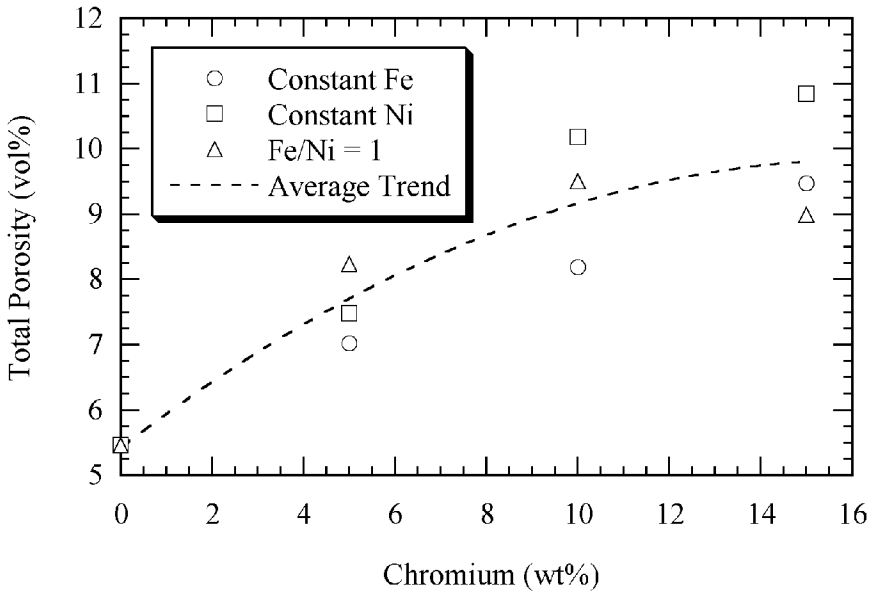

Figure 25. Total porosity of Fe-Ni-Cr.

The addition of CaO into nickel strongly affected as-reduced porosity as shown in Table 7 and Figure 26. Total porosity increased linearly with CaO content for samples heat-treated in the as-extruded condition. Samples which were solutionized in air prior to reduction to form a (Ni,Ca)O solid solution showed a dramatically different trend between

porosity and composition as is shown in Figure 26. Microstructures of solutionized samples, Figure 27, revealed a layer of high porosity toward the outer surface of the sample while the interior areas had lower porosity levels. Samples reduced in the as-extruded condition were observed to have a constant porosity level throughout the structure.

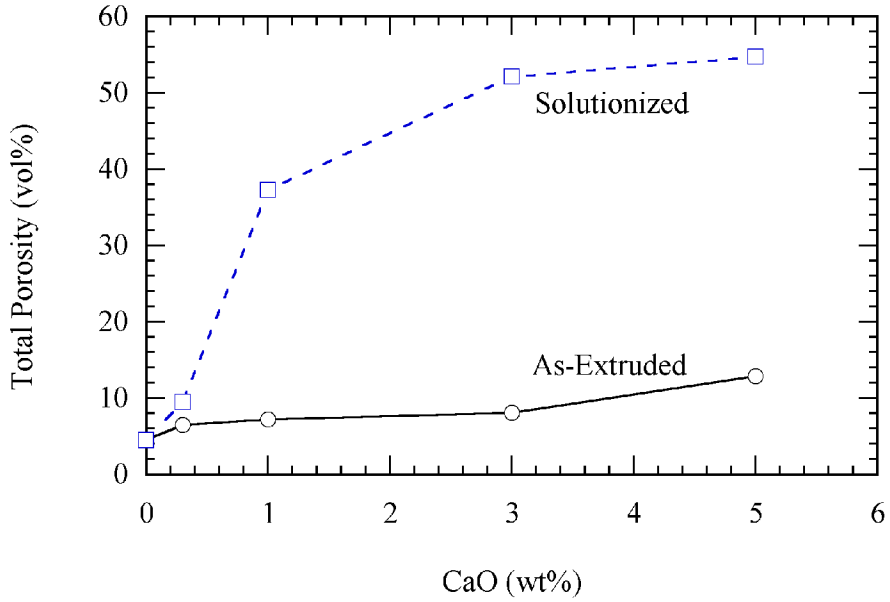

Figure 26. Total porosity of Ni-CaO after heat-treatment in hydrogen at 1300 °C for 10 h.

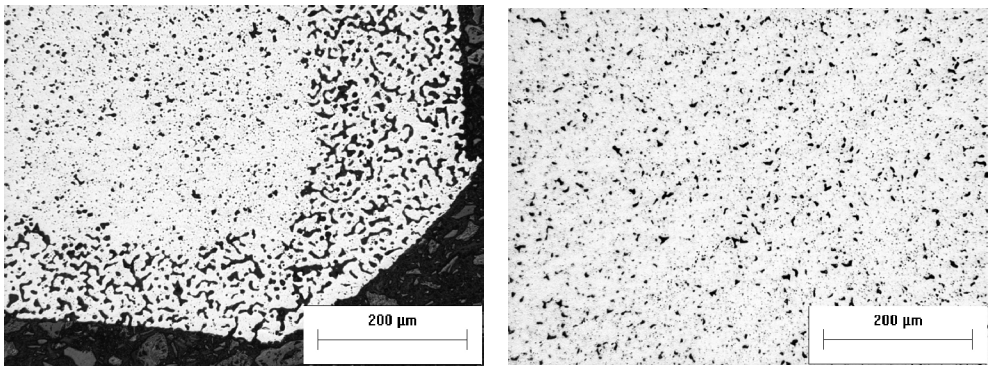

Figure 27. Optical micrographs of Ni 2 wt% CaO. Image at left is the edge region, at right in the interior region.

The solutionizing processing step for the NiO-CaO samples entailed a heat-treatment in air at 1500 °C for 2 hours. Lattice parameter measurements of solutionized samples, Figure 28, confirmed that the CaO dissolved into the NiO matrix as a result of the heat-treatment. These measurements show that the lattice parameter of the NiO phase increases linearly with CaO content up to the solid solubility limit as predicted by the phase diagram indicating that the (Ni,Ca)O solid solution was created as a result of the heat-treatment.

Additions of CaO and Y_2O_3 to Fe-Ni-Cr alloys, Tables 8 and 9, respectively, generally resulted in increased porosity levels. These samples were reduced in the as-extruded condition and were not put through a "solutionizing" heat-treatment prior to reduction as in the case of Ni-CaO samples discussed earlier. That being the case, it would be expected that the oxide particles would be located primarily on grain boundaries within the metal matrix of the alloy.

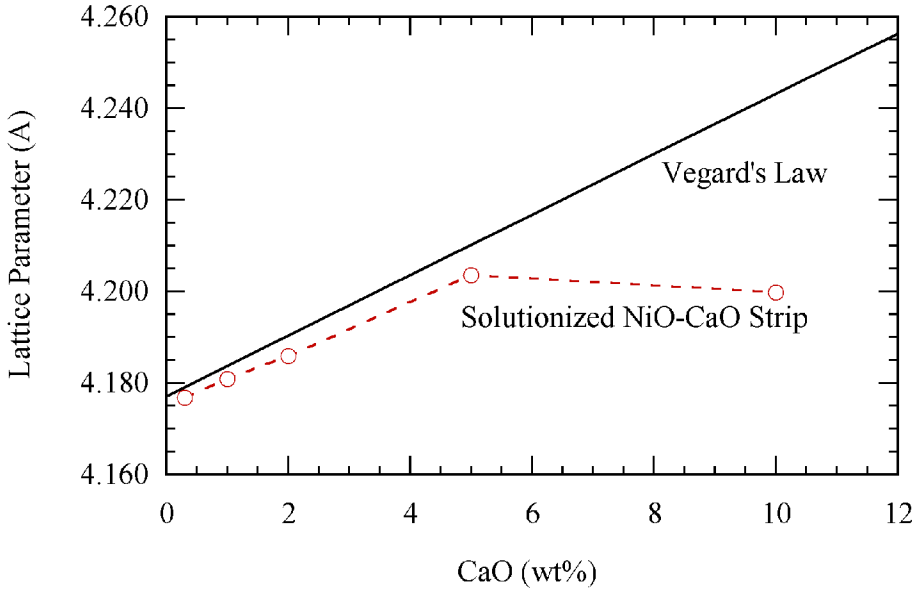

Figure 28. Lattice parameter of NiO-CaO strip solutionized in air at 1500 ° C for 2 h.

Table 7. Density and porosity of Ni-CaO samples reduced in the as-extruded and solutionized conditions.

	Composition (Ni X wt% CaO)	Density (g/cm³)			Porosity (vol%)		
		Theoretical	Bulk	Apparent	Closed	Open	Total
As-Extruded	0	8.91	8.51	8.74	1.91	2.67	4.58
	0.3	8.89	8.32	8.43	5.16	1.35	6.51
	1	8.85	8.22	8.33	5.86	1.36	7.22
	2	8.74	8.04	8.04	8.05	0.00	8.05
	5	8.63	7.54	7.77	9.98	2.90	12.88
Solutionized	0	8.91	8.52	8.58	3.71	0.75	4.46
	0.3	8.89	8.06	8.25	7.22	2.26	9.48
	1	8.85	5.63	8.61	2.67	34.61	37.28
	2	8.74	4.41	8.25	5.63	46.48	52.11
	5	8.63	4.22	7.96	7.75	47.01	54.76

Table 8. Density and porosity of Fe 47.5 Ni 5 Cr base alloys with CaO additions. Samples reduced in the as-extruded condition.

Composition* (wt% CaO)	Density (g/cm^3)			Porosity (vol%)		
	Theoretical	Bulk	Apparent	Closed	Open	Total
0	8.33	7.65	7.74	7.03	1.21	8.24
0.5	8.30	7.74	7.74	6.77	0.00	6.77
1	8.28	7.66	7.66	7.50	0.00	7.50
2	8.23	7.22	7.29	11.37	1.03	12.40
5	8.08	7.20	7.35	9.05	2.00	11.05

*Base alloy is Fe 47.5 Ni 5 Cr

Table 9. Density and porosity of Fe 39 Ni 8 Cr alloy with and without a 0.5 wt% Y_2O_3 addition.

Composition (wt%)	Density (g/cm^3)			Porosity (vol%)		
	Theoretical	Bulk	Apparent	Closed	Open	Total
Fe 39 Ni 8 Cr	8.23	7.51	7.86	4.34	4.44	8.78
Fe 39 Ni 8 Cr 0.5 Y_2O_3	8.18	7.10	7.54	7.73	5.95	13.68

Porosity is typically a concern for most sintered materials, particularly when sintering is performed without the application of pressure. Prior work [52] has shown the possibility to produce materials with near 100% theoretical density using the oxide extrusion process by using a combination of liquid-phase sintering and sintering aids. The majority of samples studied in this work sintered to 90 to 95% of theoretical density entirely in the solid state without the the addition of sintering aids. Sintering of samples containing an oxide dispersion addition was, in general, inferior to similar compositions without the oxide addition. It is important to note that the reduction heat-treatment was kept constant for the majority of samples to reduce experimental variation. It may be possible to improve the densification of many of the alloys, particularly those containing chromium, by making modifications to the reduction heat-treatment process.

4.3 Thermal Expansion

The raw data for dilatometry results for each sample tested are provided graphically in the appendix. In addition, the calculated α_T of the respective samples are included in the same figures. Results for select samples are also provided in this section though the linear expansion curves are typically omitted. The comparison plots presented in this section are intended to provide insight into the thermal expansion behavior trends within the respective systems. Unless otherwise specified, curves are constructed of continuous data and symbols are used only to signify datum sets. All compositions are in weight percent.

4.3.1 Yttria-Stabilized Zirconia

The raw expansion versus temperature data for YSZ honeycomb are shown in Figure 29 along with calculated α_T values. The average CTE (α_M) between room temperature and 1000 °C was calculated to be $10.39 \cdot 10^{-6}$ K^{-1}. This result is roughly equivalent to α_M values for the same composition of YSZ of 10.5 [15], 11 [57], and $9.8 \cdot 10^{-6}$ K^{-1} [54] found in the literature.

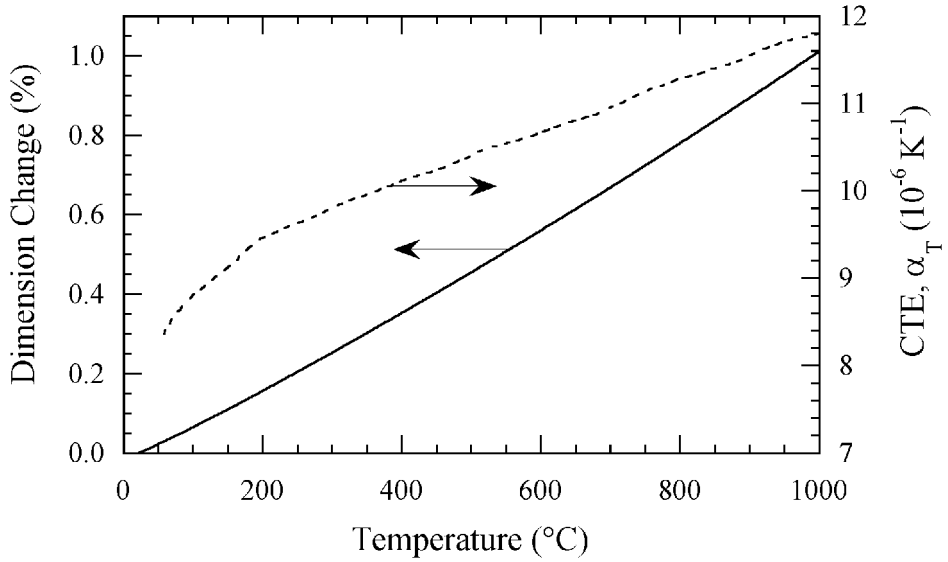

Figure 29. Linear expansion and α_T versus temperature for YSZ.

4.3.2 Nickel-Chromium System

Honeycomb samples were prepared with compositions from 0 to 15 wt% Cr at 5 wt% intervals. Figure 30 shows a plot of α_T versus temperature for these four compositions. Chromium additions tend to increase the α_T of the alloy slightly. In general, the α_T values for these compositions range from roughly $14 \cdot 10^{-6}$ K^{-1} at 100 °C to 17 to $19 \cdot 10^{-6}$ K^{-1} at 800 °C.

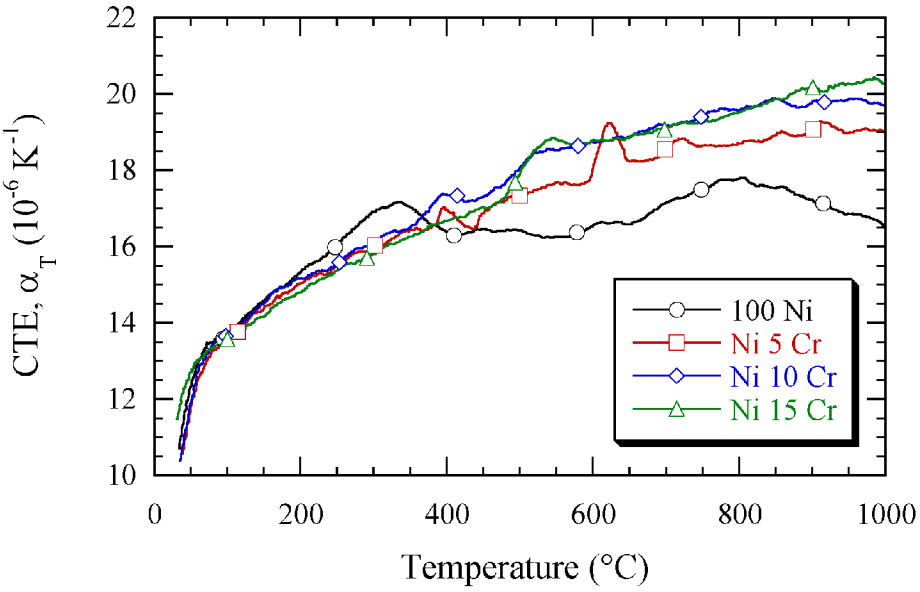

Figure 30. CTE versus temperature for Ni-Cr honeycomb alloys.

4.3.3 Iron-Chromium System

As previously mentioned, Fe-Cr alloys with less than roughly 12 wt% Cr will experience a phase transformation upon heating at temperatures between 912 and 850 °C depending on the exact composition. The phase change results in a large discontinuity in the CTE versus temperature curves. Figure 31 shows CTE values for Fe-Cr alloys containing less that 10 wt% Cr. The respective phase transformations create a large discontinuity in the α_T vs. T plots. Also, these alloys go through a Curie transformation, signified by a slight dip in CTE, at temperatures ranging from 700 to 775 °C.

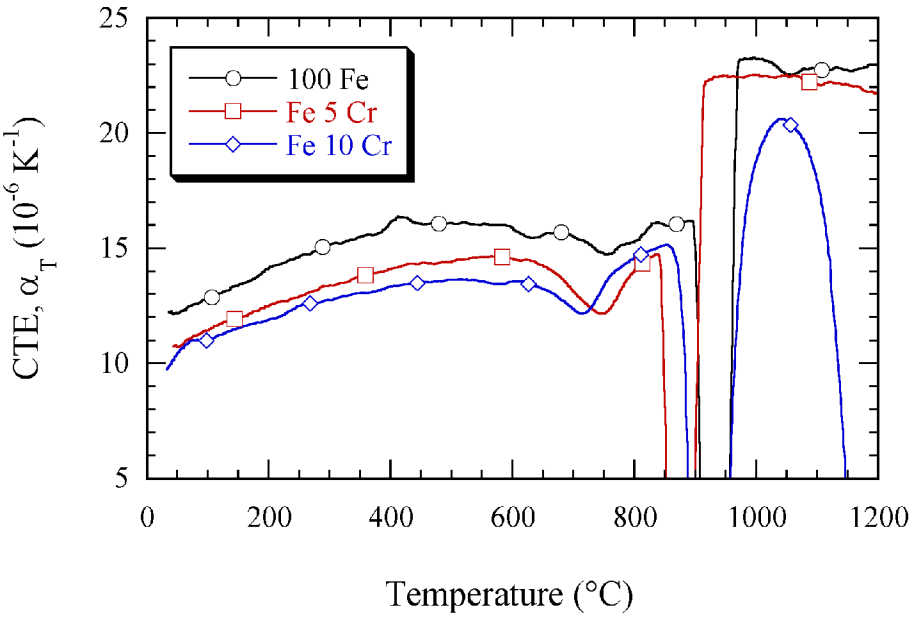

Figure 31. CTE versus temperature for Fe-Cr alloys which go through the α to γ phase transformation. The Fe 10 wt% Cr sample slumped at roughly 1050 °C.

Figure 32 shows results of α_T versus temperature for Fe-Cr alloys with greater than 10 wt% Cr. The trend of decreasing α_T with increasing chromium content at temperatures below the Curie temperature as shown in Figure 31 is also apparent for alloys which contain greater than 10 wt% Cr.

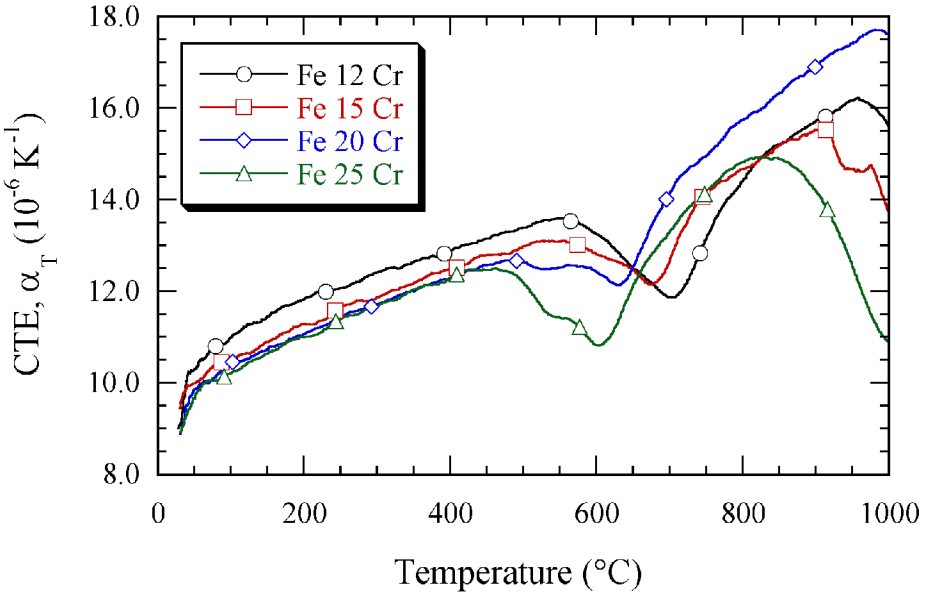

Figure 32. CTE versus temperature for Fe-Cr alloys that do not go through the α to γ phase transformation. The Fe 25 wt% Cr sample slumped after roughly 800 °C.

Values of α_T at 200 and 500 °C isotherms are plotted versus composition in Figure 33. This shows the effect of chromium content on the CTE at various temperatures across the range of Fe-Cr compositions examined in this study. There is a relatively large decrease in α_T between 0 and 10 wt% Cr. After roughly 10 wt% Cr, additional chromium has a diminishing impact on the α_T of the alloy. There is little difference in α_T values between the 20 and 25 wt% Cr alloys.

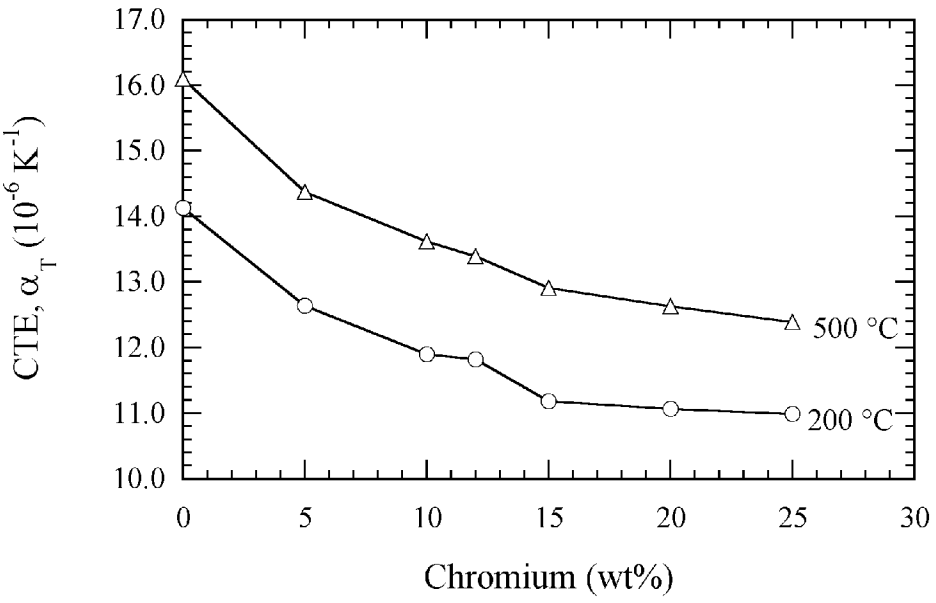

Figure 33. CTE versus chromium content for Fe-Cr honeycomb alloys at 200 and 500 °C.

The Fe-Cr alloys experience a Curie transformation as can be seen by the slight dip in the α_T curves at temperatures between approximately 600 and 750 °C in Figures 31 and 32. The measured Curie temperatures of the various Fe-Cr samples are shown in Figure 34 along with values taken from the Fe-Cr phase diagram, Figure 4. The measured values show a trend similar to the phase diagram but have an offset to lower temperatures. The phase diagram values do not extend to compositions greater than 17 wt% Cr because at equilibrium these compositions would have a two-phase structure. The honeycomb samples above 17 wt% Cr do, however, display a Curie temperature due to the fact that they do not have an equilibrium structure as a result of the normal fabrication process. The equilibrium structure can only be brought about through specific heat-treatments which incorporate long isothermal hold times at temperatures just below the equilibrium phase boundary.

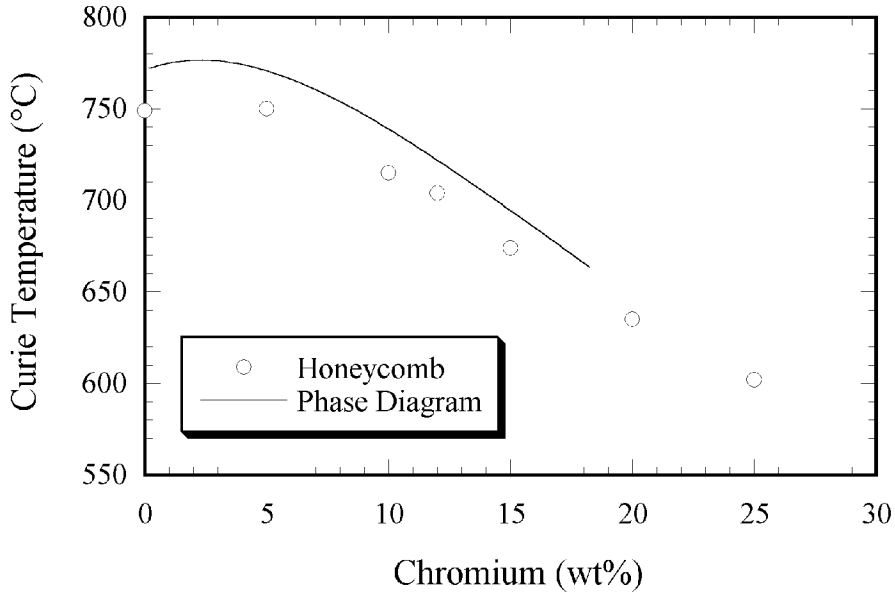

Figure 34. Curie temperatures of Fe-Cr honeycomb alloys compared with values taken from the Fe-Cr phase diagram [16].

The Fe-Cr alloys containing between 15 at 25 wt% Cr have similar α_T values as YSZ. The α_T values of alloys containing over 12 wt% Cr increase fairly linearly with temperature in much the same manner as that for YSZ. The Curie transformation of these alloys results in a non-linear CTE curve in the region around the Curie temperature although the degree of non-linearity is relatively small. Small chromium variations to an alloy in this range would have only a slight effect on the CTE of the alloy. In other words, alloys in this composition range would likely be tolerant of small (< 5 wt% Cr) composition fluctuations.

4.3.4 Iron-Nickel System

Thermal expansion and CTE as a function of temperature for a Fe 50 wt% Ni honeycomb alloy are shown in Figure 35. This plot shows several important features

which are common to several other Fe-Ni alloys examined in this study. Below the Curie temperature, the CTE is fairly constant with temperature and actually decreases slightly. The CTE increases dramatically just after the Curie temperature (Tc). This behavior is also noticeable in the linear expansion curve though it is less pronounced. After the rapid increase in α_T after Tc, the CTE continues to increase linearly with temperature.

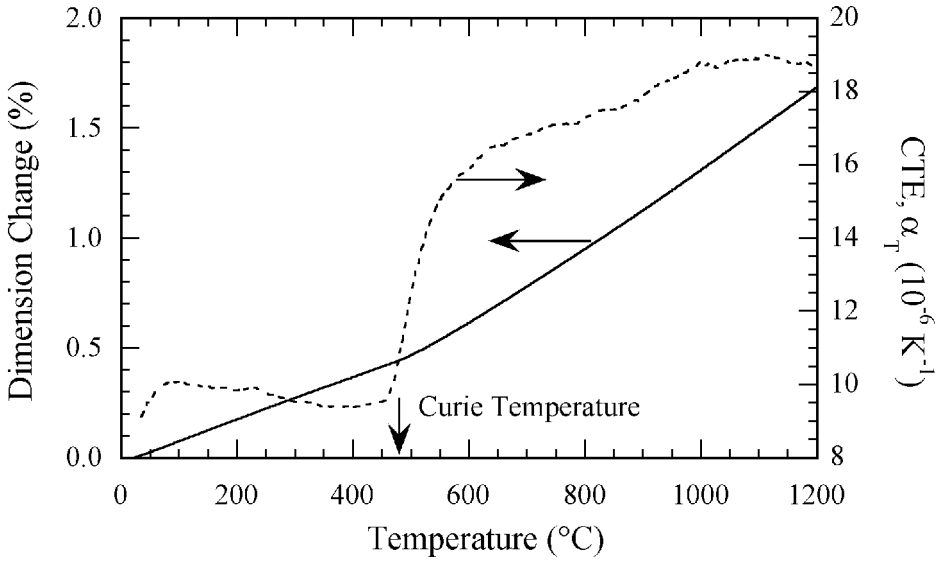

Figure 35. Linear expansion and α_T versus temperature for a Fe 50 wt% Ni honeycomb alloy.

Figure 36 shows α_T versus temperature for several other Fe-Ni alloys ranging from 30 to 75 wt% Ni in iron. Several trends can be observed from this plot. First, the Curie temperature increases with increasing nickel content. Also, the α_T values below the respective Curie temperatures increase in magnitude with increasing nickel. Another trend is that the high temperature CTE values tend to decrease slightly with increasing nickel. In other words, increasing nickel contents give rise to a lower magnitude change between the average low and high temperature CTE values.

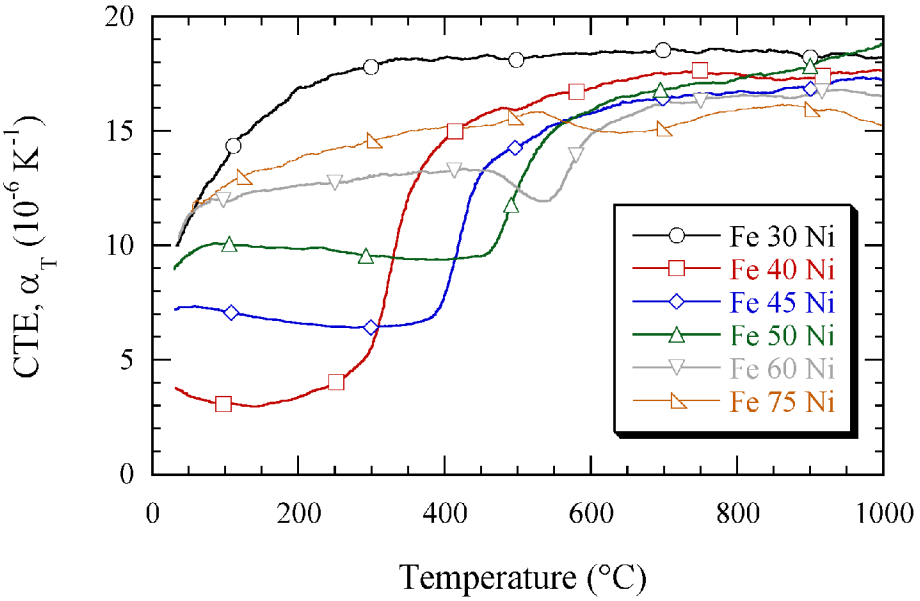

Figure 36. CTE versus temperature for several γ Fe-Ni alloys.

CTE values are plotted versus composition at several temperatures in Figure 37. The CTE drops significantly between 30 and 40 wt% Ni; the lowest CTE value tends to move toward higher nickel contents with increasing temperature. Above roughly 600 °C the characteristic invar 'dip' is no longer apparent.

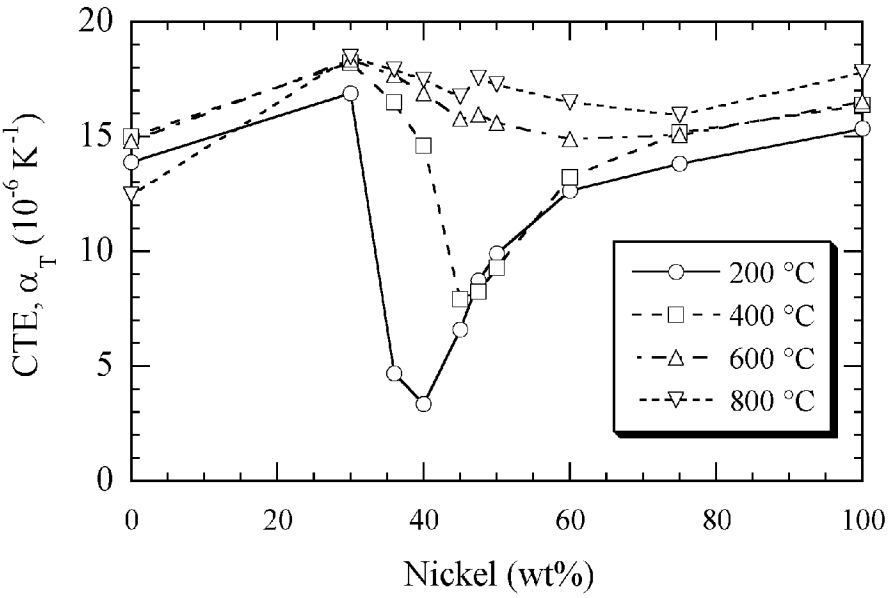

Figure 37. CTE versus nickel content at several temperatures. Symbols represent actual datum pairs; lines are for clarity only and do not represent continuous data.

Curie temperatures are shown for the austenitic Fe-Ni alloys as a function of composition in Figure 38 and compared with literature data [55]. The experimental values show a trend similar to the literature data but have a offset to lower temperatures. The Curie temperature initially increases dramatically from 30 to 50 wt% Ni and reaches a maximum of 560 °C at 67 wt% Ni. Between 67 and 100 wt% Ni, the Curie temperature decreases with increasing nickel content.

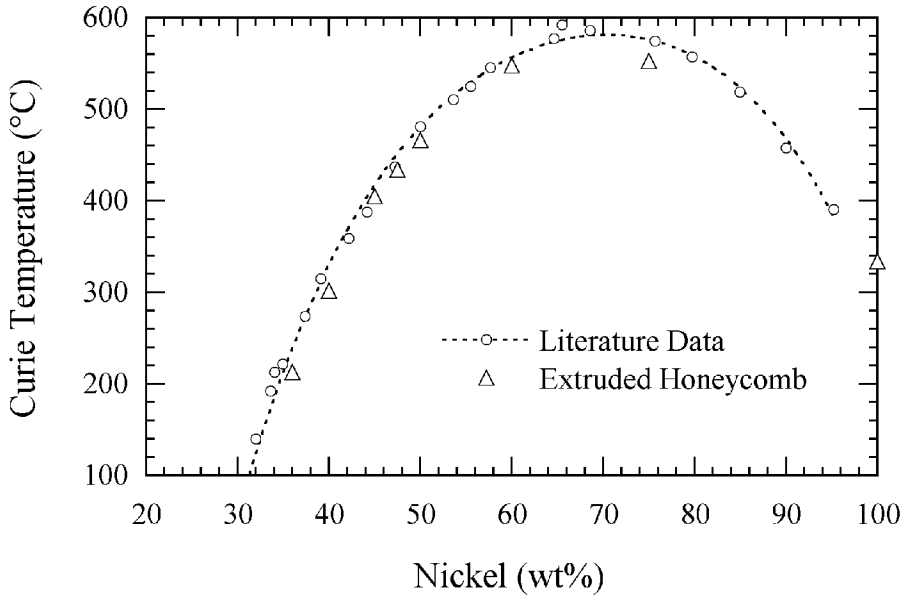

Figure 38. Curie temperature of γ Fe-Ni honeycomb alloys compared with literature data [55].

Table 10 shows α_M values for the Fe-Ni alloys as calculated using Equation 3.3 along with the Curie temperature of the alloy. In this table, the low temperature α_M refers to the α_M between room temperature and an upper temperature, *T*, which is 50 °C less than the Curie temperature for that alloy. Likewise, high temperature α_M value is defined from a initial temperature of 50 °C above the Curie temperature of the alloy to an upper temperature of 1000 °C. The low temperature α_M values increase with increasing nickel content while the high temperature α_m values show a small decrease with composition. The CTE for YSZ was calculated between room temperature and 500 °C and between 500 and 1000 °C for the low and high regions, respectively.

Table 10. Average CTE and Curie temperature for Fe-Ni alloys.

Sample Composition (wt%)	Curie Temperature (°C)	Low Temp CTE, α_M, (10^{-6} K^{-1})	High Temp CTE, α_M, (10^{-6} K^{-1})
Fe 30 Ni	*	N/A	18.45
Fe 36 Ni	213	1.70	17.43
Fe 40 Ni	302	3.20	16.96
Fe 45 Ni	405	6.77	16.32
Fe 47.5 Ni	434	8.73	17.01
Fe 50 Ni	473	9.73	17.09
Ni 40 Fe	548	12.72	16.41
Ni 25 Fe	553	14.16	15.69
YSZ	n/a	9.05	10.88

*Curie Temperature was not measureable

The Fe-Ni alloys exhibit a wide range of α_T values. For compositions near Fe 50 wt% Ni, the low temperature CTE is close to that of YSZ. However, these alloys go through a Curie transformation upon heating which introduces a large degree of non-linearity in the CTE versus temperature plots. Also, the CTE of an alloy near 50 wt% Ni would be strongly dependent on the exact composition of the material. Small changes (roughly 1 or 2 wt%) would likely have a noticeable impact on not only the CTE but also the Curie temperature of the material. If such a material were used in an engineering application, close control over the material composition would be necessary. As shown earlier, the metal oxide extrusion process is likely capable of meeting this type of requirement.

4.3.5 Iron-Nickel-Chromium System

Starting from a composition of Fe 50 wt% Ni, chromium additions were made three ways: keeping the iron content constant (50 Fe 50-x Ni x Cr), keeping the Fe/Ni ratio constant ((100-x)/2 Fe (100-x)/2 Ni x Cr) and keeping the nickel content constant (50 Ni

50-x Fe x Cr). For each method, chromium was added in 5 wt% increments. Figure 39 shows the effect of a chromium addition on the linear expansion of Fe/Ni = 1 alloys. It can be seen that the chromium addition causes an increase in net expansion at a given temperature. The α_T values plotted versus temperature for these same alloys are shown in Figure 40. This plot shows that the Tc of the alloy decreases with increasing chromium content. Furthermore, the α_T values above the respective Curie transformations tend to increase with increasing chromium.

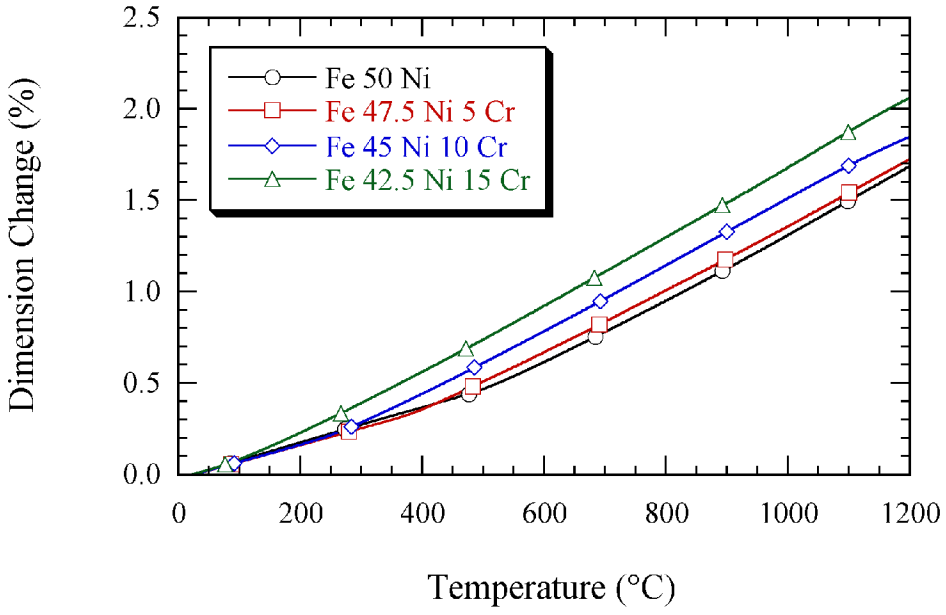

Figure 39. Linear expansion for Fe/Ni = 1 alloys.

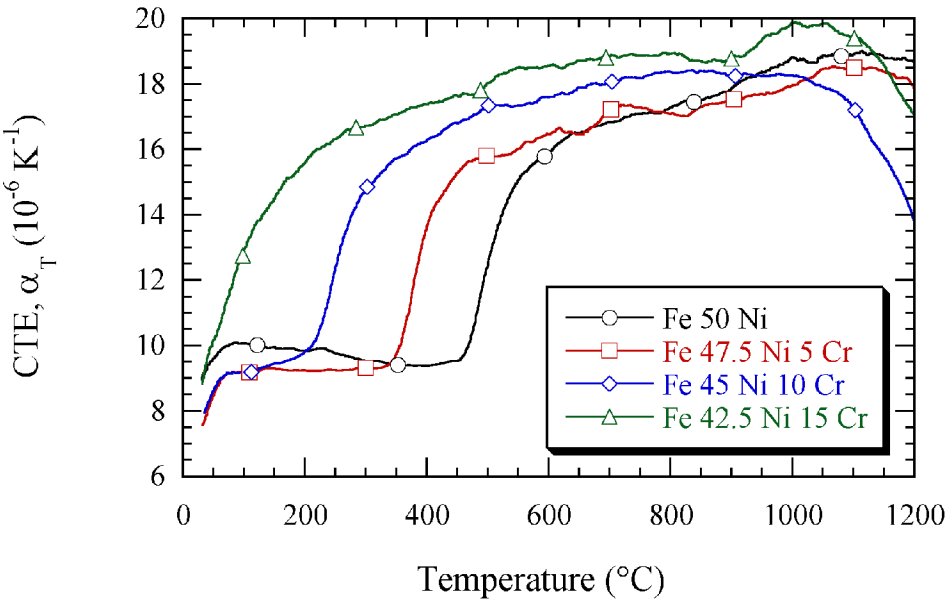

Figure 40. CTE versus temperature for Fe/Ni = 1 alloys.

The effect of Fe/Ni ratio at a constant 10 wt% Cr on α_T is shown in Figure 41. The Curie temperature tends to decrease with higher Fe/Ni ratios. Also, higher Fe/Ni ratios lead to lower α_T values below the Curie temperature and higher α_T values above the Curie temperature.

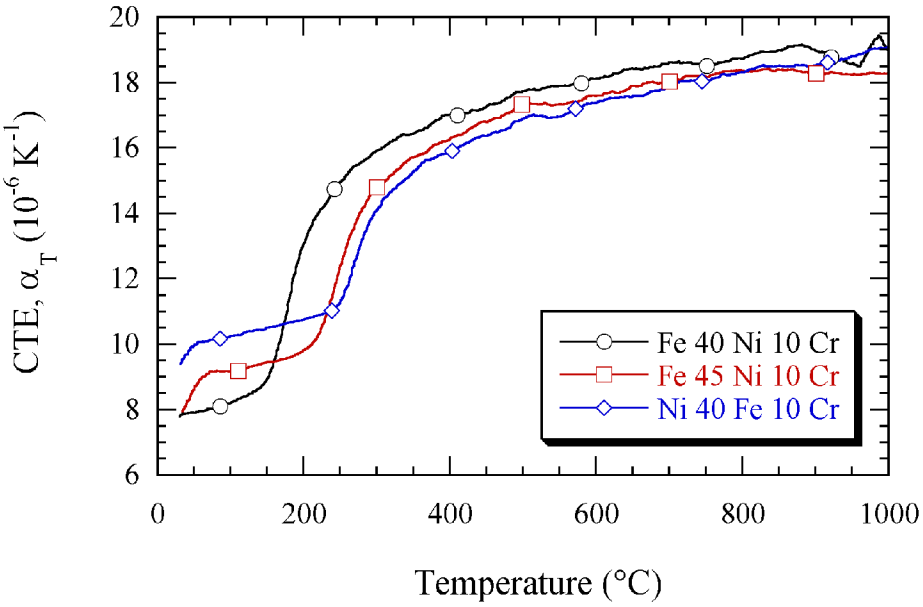

Figure 41. CTE versus temperature for Fe-Ni-Cr alloys with 10 wt% Cr.

The average CTE values before and after the Curie transformation are tabulated in Table 11. As with Table 10 for Fe-Ni alloys, the low temperature α_M is defined from room temperature to 50 °C less than the Tc for each particular alloy. High temperature α_M is defined from 50 °C above the Curie temperature to 1000 °C. The CTE for YSZ was calculated between room temperature and 500 °C and between 500 and 1000 °C for the low and high regions, respectively. An interesting observation from the α_M data in Table 11 is that the low temperature α_M varies only slightly within a given alloy group (Constant Fe, etc.). For example, for Fe/Ni = 1 alloys, the low temperature α_M varies from 9.14 to $9.17 \cdot 10^{-6}$ K^{-1}. The curie temperature, however, has much more variation within the sample groups, varying as much as 300 °C. The high-temperature α_M values tend to vary to a larger degree within sample groups. For each group, higher Cr content results in a slight increase in high-temperature α_M values.

Table 11. Summary of CTE values before and after the respective Curie temperatures

	Sample Composition (wt%)	Curie Temperature (°C)	Low Temp CTE, α_M, (10^{-6} K^{-1})	High Temp CTE, α_M, (10^{-6} K^{-1})
	Fe 50 Ni	473	9.73	17.09
Constant Fe	Fe 45 Ni 5 Cr	324	7.93	17.24
	Fe 40 Ni 10 Cr	156	8.02	17.84
	Fe 35 Fe 15 Cr	*	*	17.99
Fe/Ni = 1	Fe 47.5 Ni 5 Cr	353	9.17	17.12
	Fe 45 Ni 10 Cr	221	9.16	17.52
	Fe 42.5 Ni 15 Cr	64	9.14	17.94
Constant Ni	Ni 45 Fe 5 Cr	375	10.07	16.98
	Ni 40 Fe 10 Cr	251	10.32	17.42
	Ni 35 Fe 15 Cr	89 (est.)	10.20	17.83
	YSZ	n/a	9.05	10.88

*Curie Temperature was not measurable

The Curie temperatures for the Fe-Ni-Cr compositions shown in Table 11 are plotted along with Fe-Ni binary alloys in Figure 42. Literature data was taken from Chevenard [55] for comparison. The honeycomb samples show similar trends as the literature values but have an offset to lower temperatures. The Curie temperature is seen to be strongly dependent on the chromium content of the alloy.

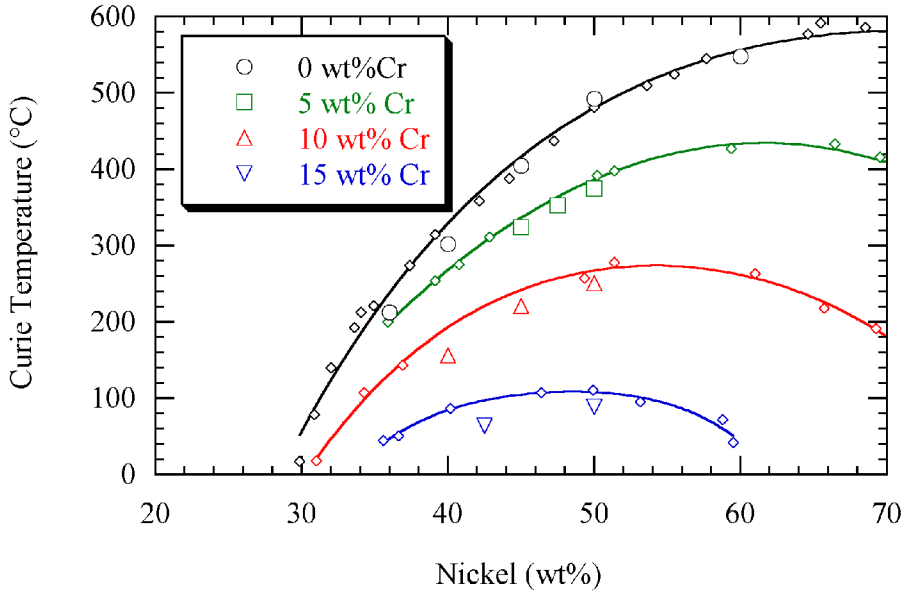

Figure 42. Curie temperature for Fe-Ni and Fe-Ni-Cr honeycomb alloys. Literature data [55] are shown as small diamond symbols with corresponding curve-fits for each respective chromium content.

Another group of Fe-Ni-Cr alloys with higher iron contents was also examined. Figure 43 shows the linear thermal expansion curves for three alloys with 75 to 80 wt% Fe. Although the samples have similar compositions, one displays significantly different expansion behavior. Upon examination of the Fe-Ni-Cr ternary phase diagram, it become evident that the two samples with 10 wt% Ni went through a partial phase change upon heating. The Fe 15 Ni 10 Cr sample shows a very linear expansion curve and does not go through any apparent phase or Curie transitions. From the phase diagram, this composition lies within the γ Fe,Ni,Cr phase field at 650 °C and above. The Fe 15 Ni 5 Cr and Fe 10 Ni 10 Cr samples lie on the γ / $\alpha + \gamma$ phase field at 650 °C. The two-phase region expands to higher nickel contents with decreasing temperatures. It is therefore likely that these two samples were two-phase at room temperature and transformed into single phase γ Fe,Ni,Cr

upon heating to roughly 600 °C. The expansion curves also support this hypothesis. It has been shown that α Fe alloys have a lower CTE that γ phase alloys. The expansion curves for the Fe 15 Ni 5 Cr and Fe 10 Ni 10 Cr alloys have a lower initial slope (thus CTE) than the Fe 15 Ni 10 Cr sample. Just after the phase transformation, the curves have a slope similar to the Fe 15 Ni 10 Cr sample up until roughly 1000 °C where both samples began to slump in the dilatometer.

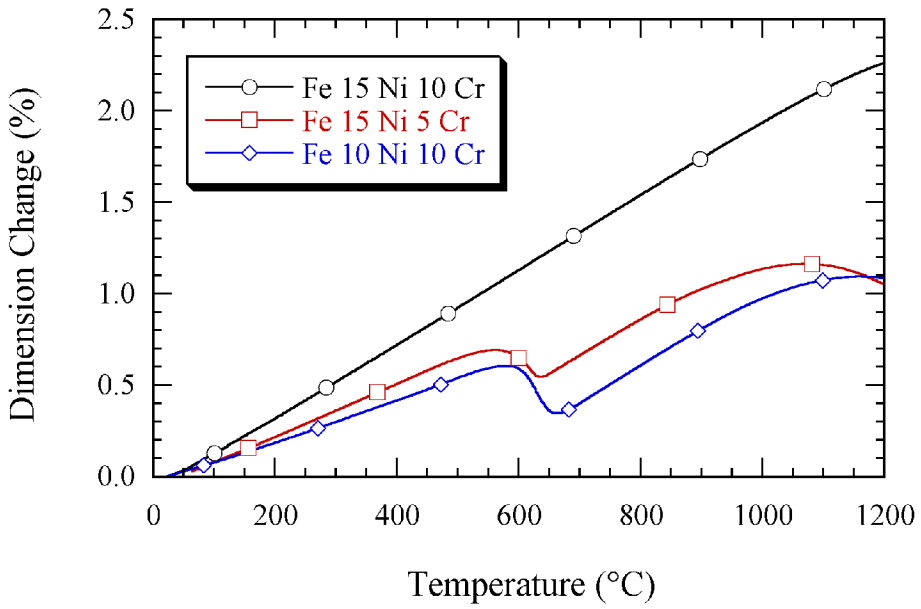

Figure 43. Linear expansion of Fe-Ni-Cr alloys.

The transformation between γ and α + γ phase fields does not occur at the same temperature on heating as on cooling. A separate experiment was performed using the Fe 10 wt% Ni 10 wt% Cr sample with a modified furnace schedule. The samples was heated at 3 °C/min up to 900 °C, held for 30 min, and cooled at 3 °C/min. Data were collected throughout the run thereby providing heating and cooling curves. Figure 44 shows the linear expansion of Fe 10 wt% Ni 10 wt% Cr on heating and cooling. The transition

occurred at 586 °C on heating and 216 °C on cooling.

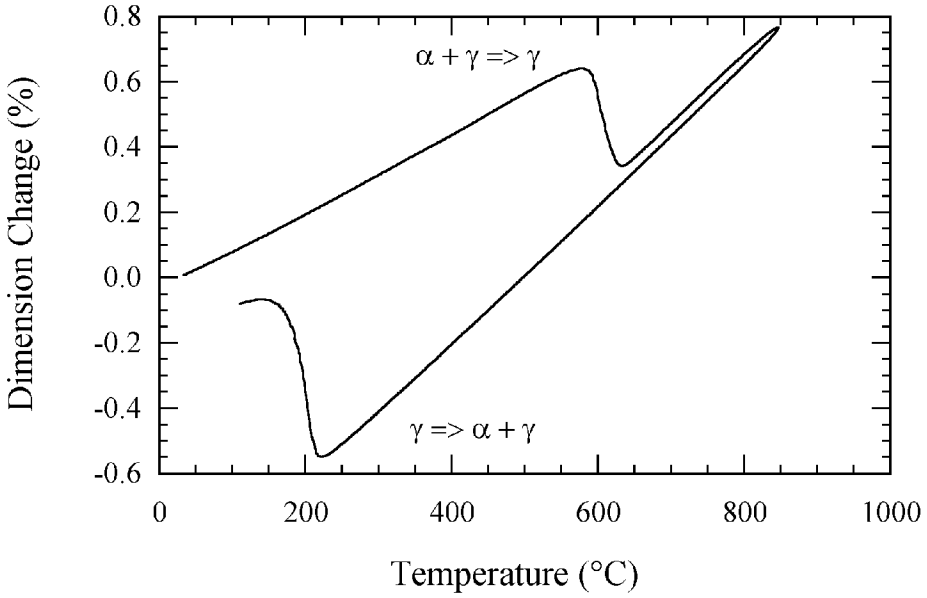

Figure 44. Linear expansion of Fe 10 wt% Ni 10 wt% Cr on heating and cooling.

This type of behavior is in contrast with the Curie transformation which occurs at roughly the same temperature on heating as on cooling. As shown in the expansion and CTE curves for Fe 47.4 wt% Ni, Figures 45 and 46, respectively, an alloy which undergoes a Curie transformation upon heating will exhibit the same event at roughly the same temperature upon cooling. The sample in Figures 45 and 46 was heated in the same manner as was used for the Fe 10 wt% Ni 10 wt% Cr alloy shown in Figure 44. The linear expansion curve, Figure 45, shows a slight amount of slump when the sample reached the 900 °C hold temperature which resulted in a small amount of offset between the heating and cooling curves. The CTE curves, Figure 46, are nearly identical with the exception of the CTE above ~ 780 °C, which is a remnant of the expansion slump, and the small

difference in Curie temperature which was measured to be 425 °C on heating and 411 °C on cooling.

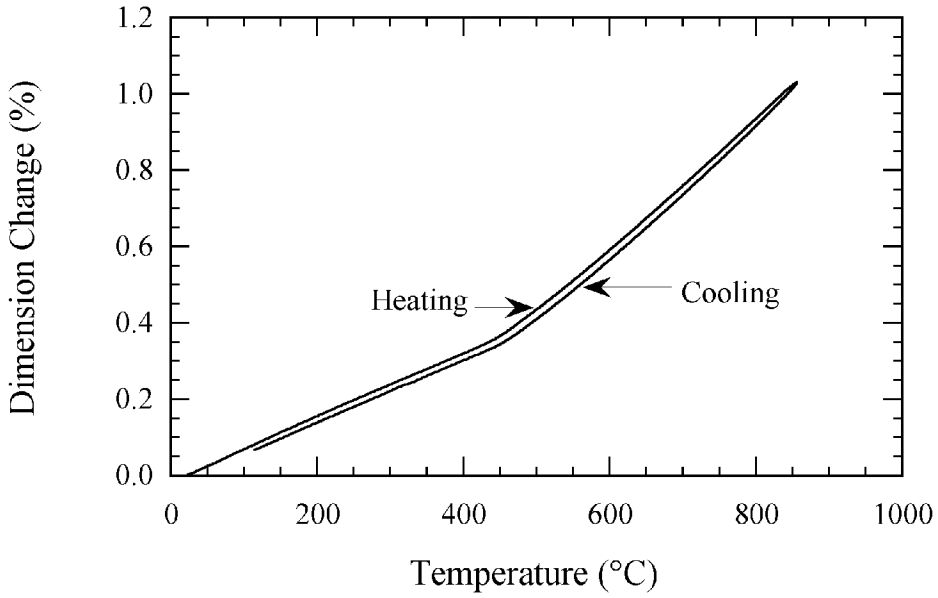

Figure 45. Linear expansion of Fe 47.5 wt% Ni honeycomb on heating and cooling.

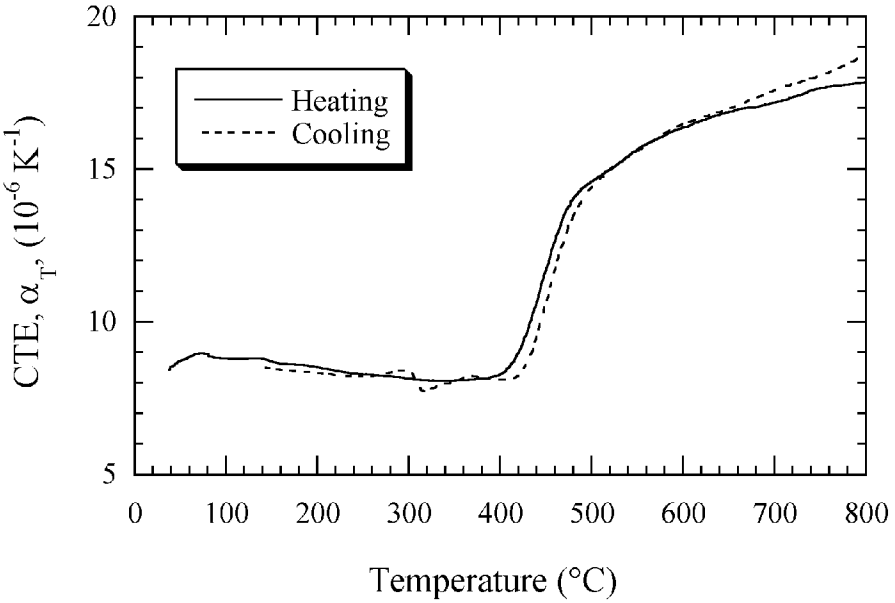

Figure 46. CTE of Fe 47.5 wt% Ni on heating and cooling.

4.3.6 Oxide-Dispersion Strengthened Samples

Two different processing routes were used to fabricate Fe-Ni-Cr alloys with and without an addition of CaO. Samples referred to as "solutionized" were heat-treated in air at 1300 °C for 2 hours prior to the reduction stage. The "non-solutionized" were reduced as-extruded and were not subjected to the heat-treatment in air prior to reduction. In both cases, the alloy samples with the CaO addition were batched to form a 47.025 wt% Fe, 47.025 wt% Ni, 4.95 wt% Cr 1 wt% CaO after reduction. Those without the CaO addition were batched to form a 47.5 wt% Fe 47.5 wt% Ni 5 wt% Cr alloy. The following plots display abbreviated compositions.

Figure 47 shows a comparison of α_T versus temperature for solutionized samples with and without the CaO addition. Figure 48 shows a similar plot for non-solutionized samples. In both cases, the presence of the oxide in the final structure results in no

observable difference in α_T with temperature. Of particular note are the Curie temperatures of the different samples; the Curie temperature range for the four samples is less that 5 °C. The Curie temperature has been shown to be sensitive to composition changes either in the form of Fe/Ni ratio or chromium content. The presence of the oxide in the structure does not appear to affect the reduction and homogenization of the metal alloy. From Figures 47 and 48, it appears that small additions of oxides can be introduced without altering the thermal expansion behavior of the alloy to any appreciable degree. Furthermore, the processing route can be modified to include a pre-reduction heat-treatment without changing the final thermal expansion properties. Attempts were made to fabricate Fe-Ni-Cr-CaO samples with higher amounts of CaO. However, samples with greater than 1 wt% CaO tended to have large defects after the reduction heat-treatment which rendered the samples unusable.

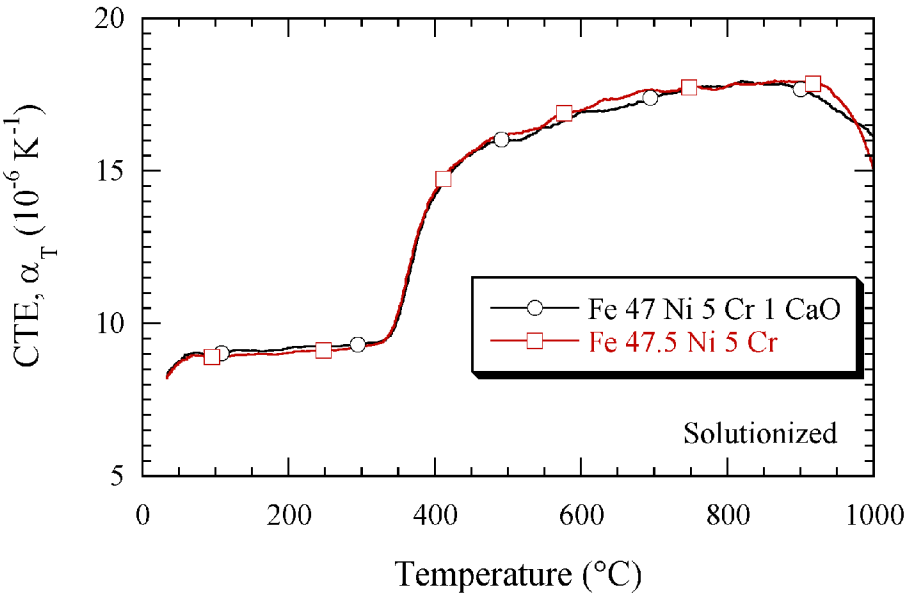

Figure 47. CTE versus temperature for Fe-Ni-Cr with and without a 1 wt% CaO addition. Both samples were heat-treated in air prior to the reduction heat-treatment.

Figure 49 shows the CTE of a Fe 39 wt% Ni 8 wt% Cr alloy with and without a 0.5 wt% Y_2O_3 addition. Both samples were reduced in the as-extruded condition. The presence of the oxide addition resulted in no observably significant change in the CTE behavior of the alloy throughout the majority of the experiment. At high temperatures, the alloy without the yttria addition was observed to slump after ~ 1100 °C while the alloy with the yttria addition did not slump during the experiment. However, this observation was not necessarily due solely to the presence of the oxide addition; experimental set-up of the dilatometer could also have been the cause of this observation.

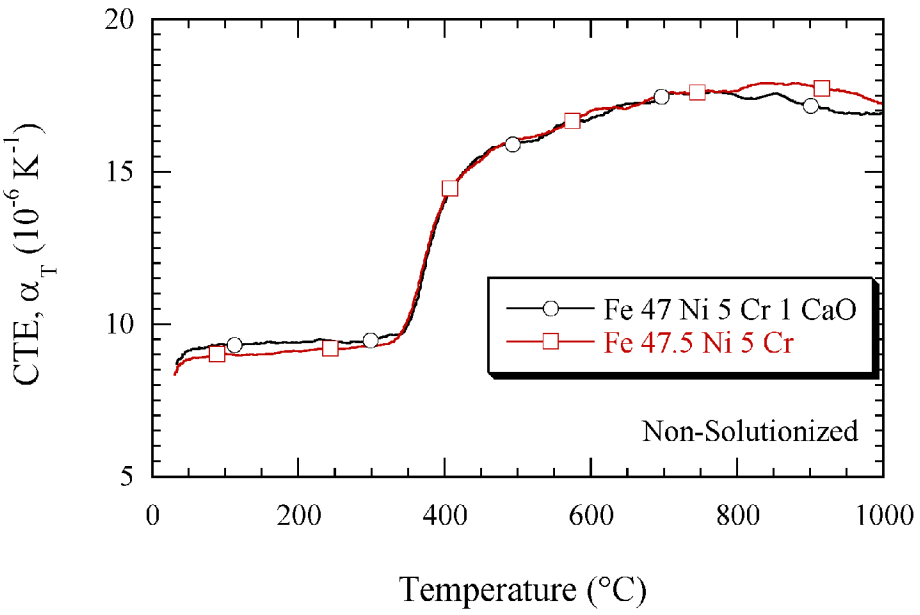

Figure 48. CTE versus temperature for Fe-Ni-Cr with and without a 1 wt% CaO addition. Both samples were reduced in the as-extruded condition.

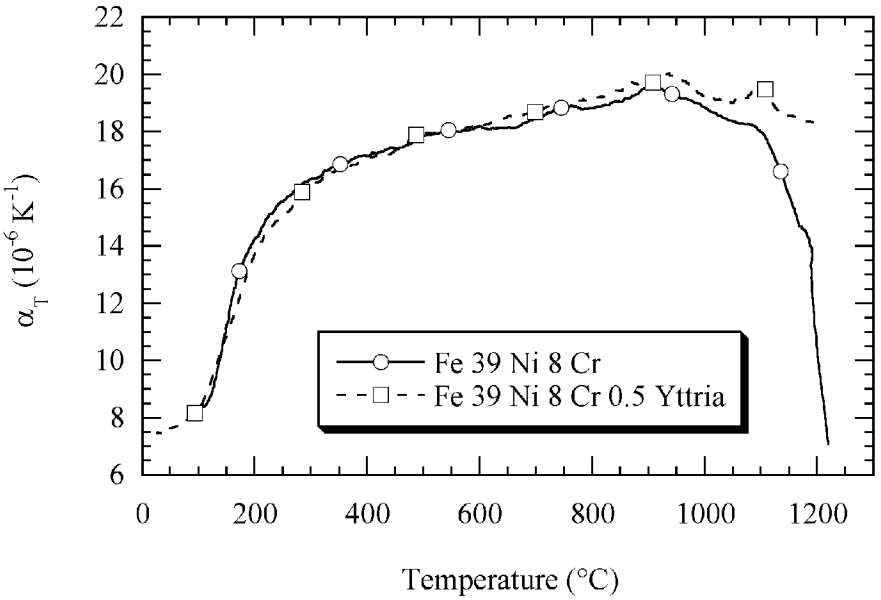

Figure 49. CTE versus temperature for a Fe 39 Ni 8 Cr alloy with and without a 0.5 wt% Y_2O_3 addition.

The thermal expansion behavior of Fe-Cr, Fe-Ni, Ni-Cr, and Fe-Ni-Cr alloys have been described for a wide range of alloy compositions. In general, Fe-Cr and Ni-Cr alloys have fairly linear CTE versus temperature behavior much like that for YSZ. Fe-Ni alloys, on the other hand, have highly non-linear CTE versus temperature behavior due to the strong impact of the Curie transformation in these alloys. Fe-Ni-Cr alloys based on a Fe 50 wt% Ni composition also have highly non-linear CTE versus temperature behavior. Curie temperature measurements made from honeycomb samples matched well with literature data. Alloys containing an oxide dispersion were shown to have nearly identical thermal expansion behavior as similar alloys without an oxide addition.

4.4 Thermal Mismatch

Allowable mismatch in thermal expansion between SOFC materials has been mentioned [2, 6], though the proposed design limits are not generally in agreement. For traditional SOFCs, the evolution of stress due to thermal expansion mismatch would depend on the fabrication method; stress would evolve on heating for stacks rigidly joined at room temperature or on cooling for stacks joined during the high-temperature heat-treatment required for certain types of seals. For hybrid SOFCs, interfacial stress initiates upon cooling at a temperature below which atomic diffusion, plastic flow, and microstructural recrystallization processes in the metal layers can relieve interfacial stresses.

As described previously, raw thermal expansion data for the various alloy samples were compared with that of YSZ to calculate thermal expansion mismatch. All alloy samples described here are compared with 8 mol% YSZ (Figure 68). Mismatch values were calculated using two methods. The first method assumed that the two materials were at a stress-free state at room temperature and expansion mismatch accumulated upon heating. The second method assumed that the materials were at a stress-free state at some temperature above which stress due to thermal expansion mismatch could dissipate due to creep, relaxation, or other such phenomena. Expansion mismatch would then accumulate upon cooling from that upper temperature.

4.4.1 Mismatch upon Heating

Two materials with identical α_T versus T behavior would have zero mismatch for any temperature change, though such identical thermal expansion behavior is uncommon particularly when comparing ceramics to metals. The general trends outlined in the

previous section for the different alloy systems show that several groups of alloys have fairly close α_T values compared to YSZ. Specifically, the Fe-Cr alloys which do not go through the α to γ transformation on heating, Fe-Ni alloys with roughly 50 wt% Ni, and certain Fe-Ni-Cr alloys have α_T values in the general range of that noted for YSZ.

Figure 50 shows the expansion mismatch, $\Delta E_{T,\,heating}$, for Fe 15, 20 and 25 wt% Cr. The mismatch between YSZ and these alloys ranges between 0.20 and 0.28% at 1000 °C. Fe-Cr alloys with less than 10 wt% chromium, Figure 51, also have a low mismatch with YSZ but these alloys go through a phase transformation on heating at temperatures between 850 and 925 °C which results in a dramatic dimension change over a short temperature interval. After going through the α to γ phase transition, the mismatch between the Fe 5 and 10 wt% Cr samples and YSZ falls to roughly zero due to the contraction associated with the phase change.

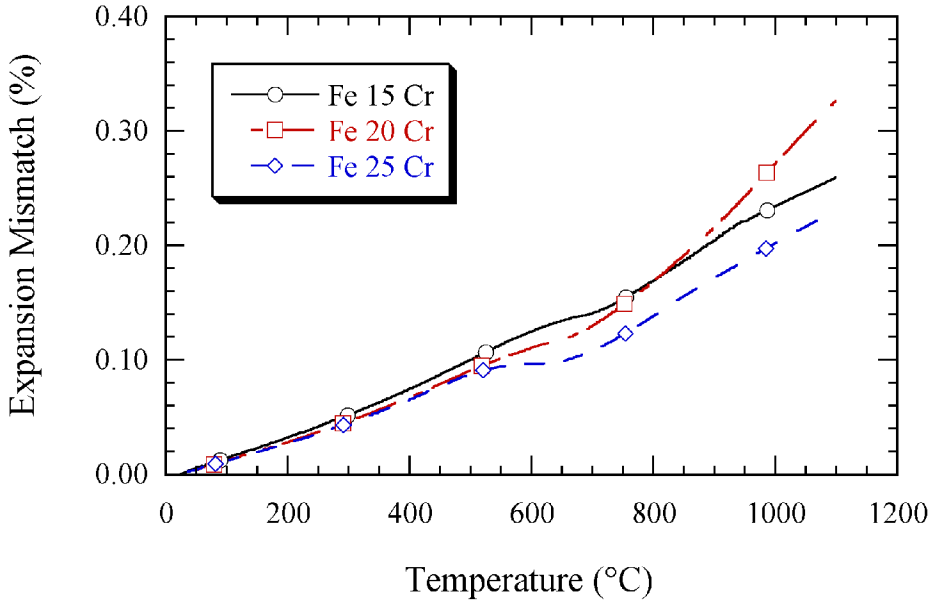

Figure 50. Expansion mismatch on heating for Fe-Cr alloys.

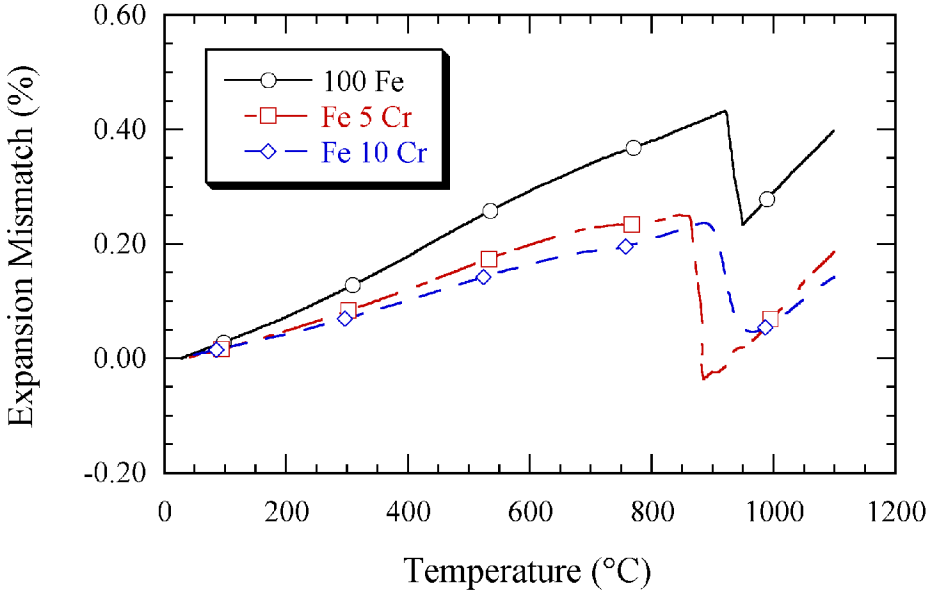

Figure 51. Expansion mismatch on heating for Fe-Cr alloys.

The $\Delta E_{T,\,heating}$ results for several Fe-Ni binary alloys are shown in Figure 52. The Fe 45 wt% Ni sample had zero mismatch with YSZ at a temperature of roughly 625 °C. A closer look at Fe-Ni alloys containing between 40 and 50 wt% Ni is shown in Figure 53. While the Fe 45 wt% Ni has a zero mismatch at 625 °C, the Fe 47.5 wt% Ni alloy had a lower maximum mismatch between room temperature and 600 °C than the 45 wt% Ni sample.

Figure 54 shows $\Delta E_{T,\,heating}$ values for Fe-Ni-Cr alloys with a iron-to-nickel ratio of one. The addition of chromium to the Fe 50 wt% Ni alloy resulted in a general increase in mismatch upon heating. The temperature at which the mismatch began to increase from near-zero values decreased with increasing chromium content. The Fe 50 wt% Ni sample had a near-zero mismatch with YSZ up to ~ 500 °C while the addition of 10 wt% Cr

decreased this zero-mismatch temperature to ~200 °C. Mismatch upon heating results for Fe-Ni 10 wt% Cr alloys near the Fe/Ni = 1 ratio are shown in Figure 55. The Fe/Ni ratio has little impact on the mismatch results for these alloys. A comparison of several alloys each containing 15 wt% Cr is shown in Figure 56. The Fe 15 wt% Cr sample had far lower mismatch with YSZ at all temperatures compared with the Fe-Ni-Cr ternary of Ni-Cr binary samples.

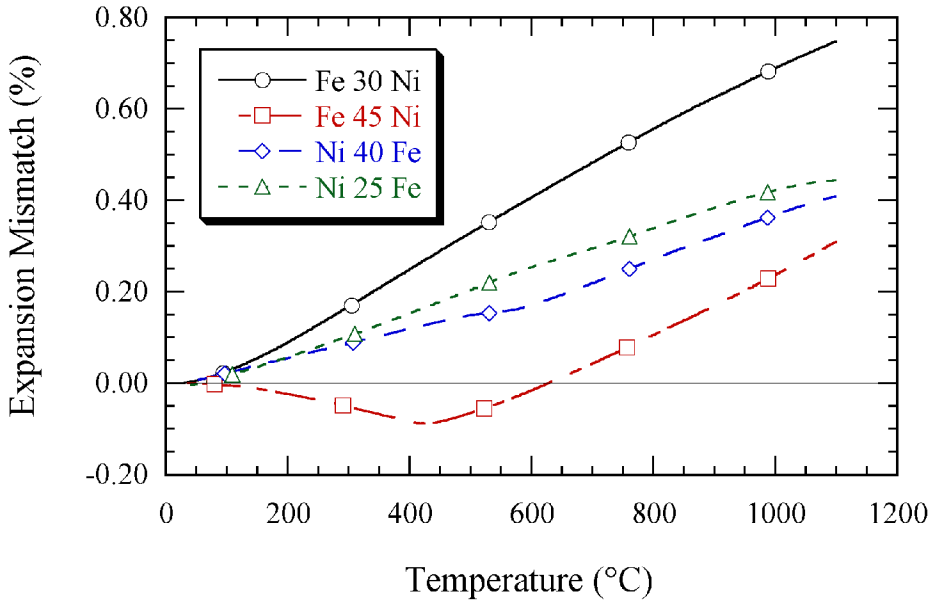

Figure 52. Expansion mismatch on heating for γ Fe-Ni alloys.

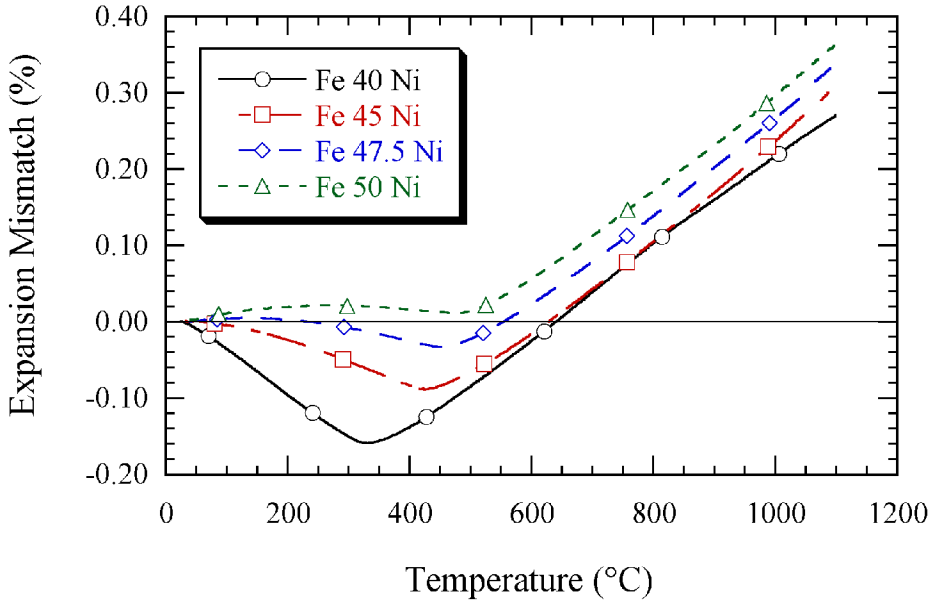

Figure 53. Expansion mismatch on heating for Fe-Ni alloys between 40 and 50 wt% Ni.

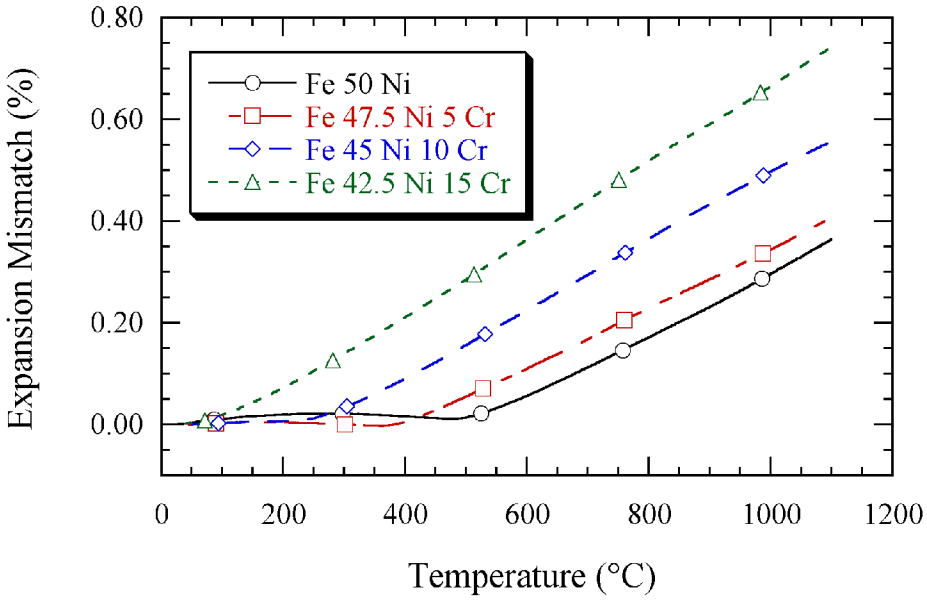

Figure 54. Expansion mismatch of Fe/Ni = 1 alloys.

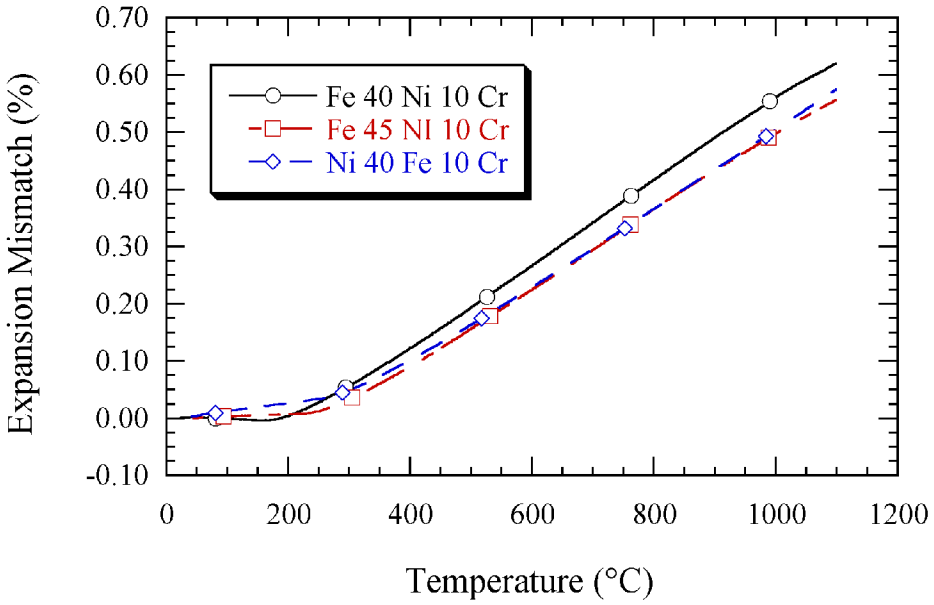

Figure 55. Expansion Mismatch of Fe-Ni-Cr alloys with 10 wt% Cr.

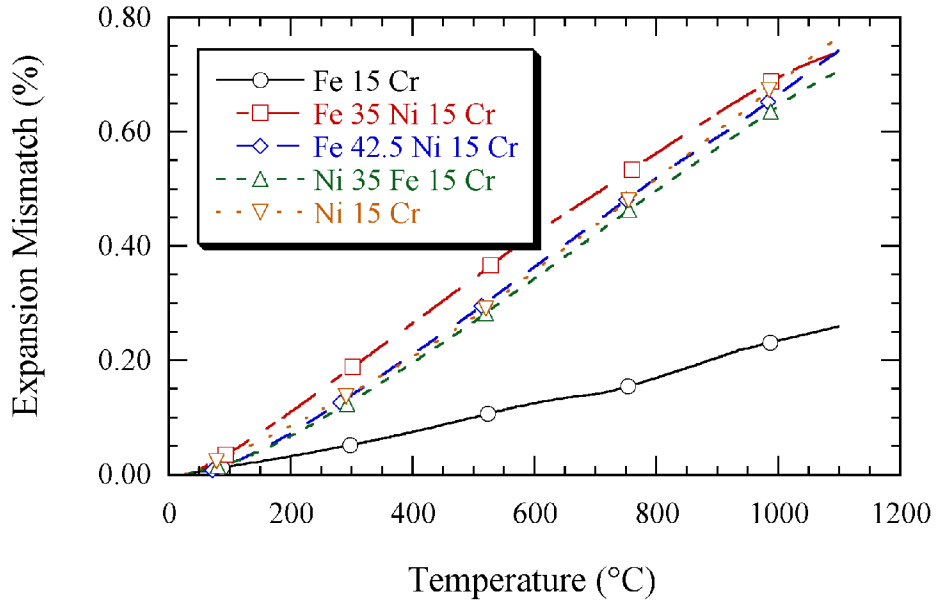

Figure 56. Expansion mismatch of select alloys each containing 15 wt% Cr.

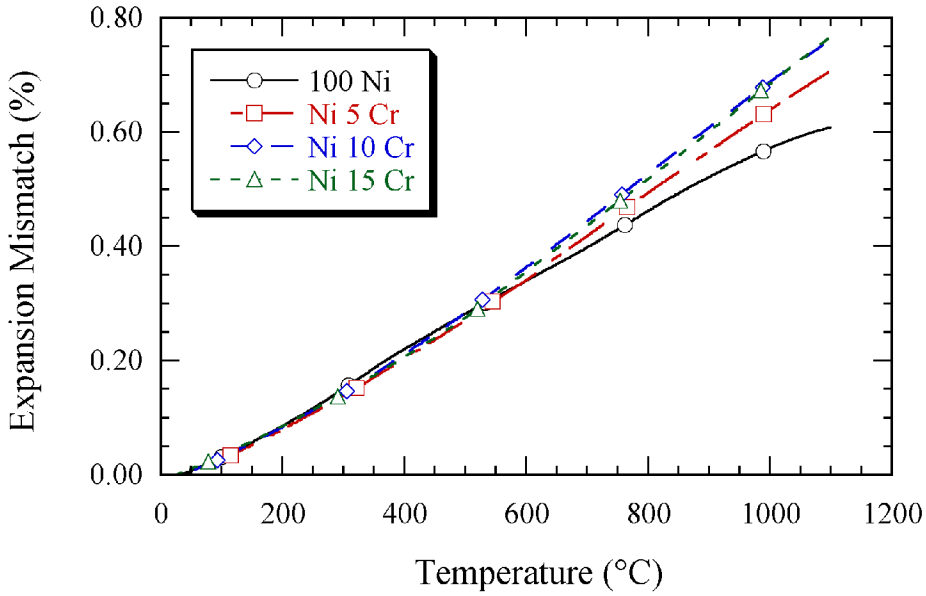

Figure 57. Expansion mismatch of Ni-Cr alloys upon heating.

The degree of alloy-YSZ thermal mismatch upon heating from room temperature is pertinent to SOFC designs that are rigidly joined at room temperature. The Fe 50 wt% Ni and Fe 47.5 wt% Ni alloys have a remarkably low mismatch with YSZ from room temperature up to roughly 500 °C, after which the mismatch begins to increase. At the target operation temperature of 700 °C, the Fe 40 wt% Ni sample has the lowest mismatch. An open question is whether the more extensive expansion mismatch at 425 °C for this composition will cause inter-layer delamination due to bowing or buckling during heating to the service temperature.

4.4.2 Cooling from 600 °C

Expansion mismatch, $\Delta E_{T,\,cooling}$, was calculated assuming that the given alloy and YSZ were in a stress-free state at 600 °C and stresses would develop upon cooling. Plots in

this section were created using raw expansion data and Equation 3.5 with a *Ts* value of 600 °C. Results would be applicable to situations where a structure were in a stress-free state at 600 °C and expansion mismatch upon cooling to lower temperatures would cause the generation of stress in the structure.

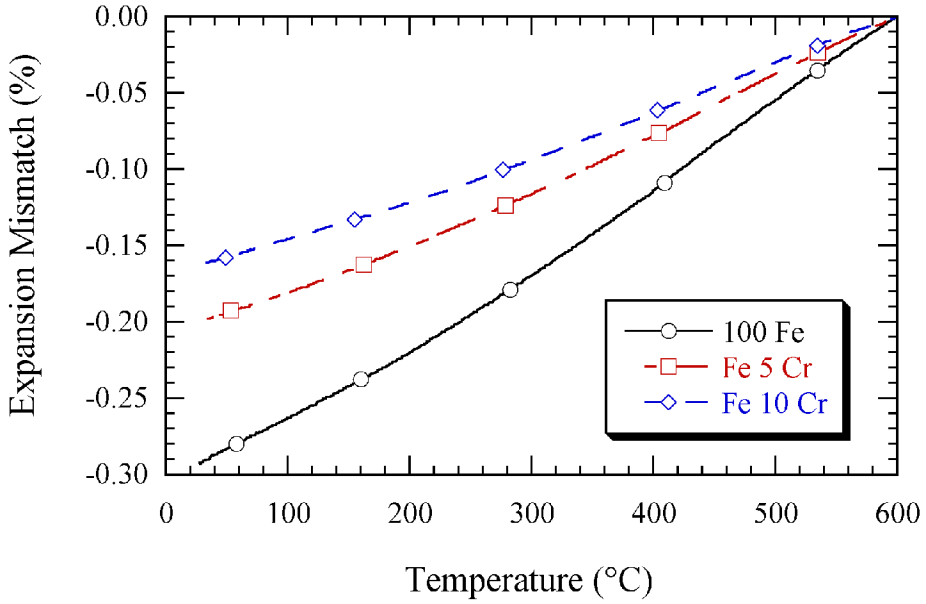

Figure 58. Expansion on cooling from 600 °C for Fe-Cr alloys under 10 wt% Cr. These results assume each alloy has fully transformed to the γ phase at 600 °C.

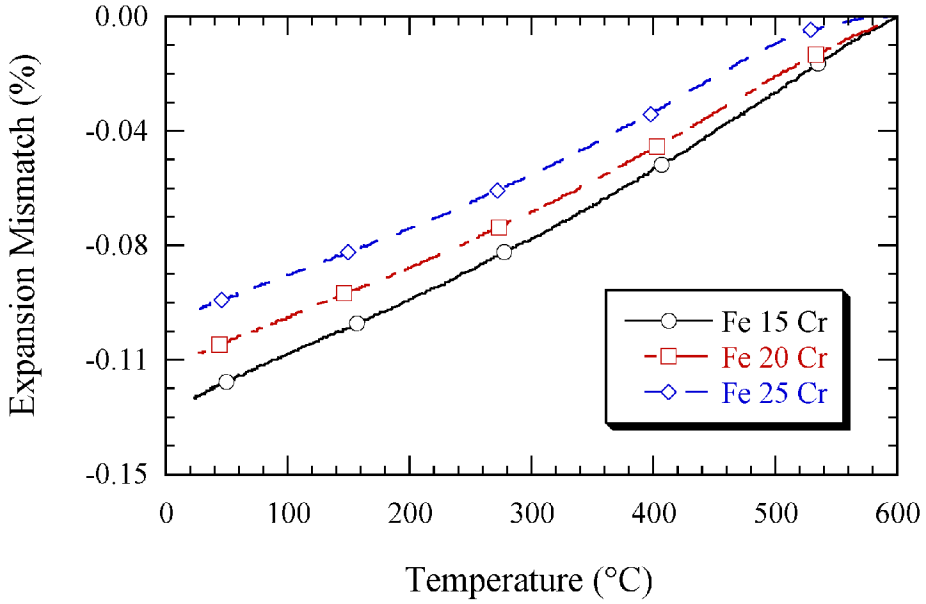

Figure 59. Expansion mismatch on cooling from 600 °C for Fe-Cr alloys containing greater than 10 wt% Cr.

Mismatch values for Fe-Ni alloys, Figure 60, show that the Fe 45 wt% Ni sample had low mismatch values from 600 °C down to room temperature and actually had a zero-net mismatch when cooled from 600 down to ~ 175 °C. A closer look at mismatch values for samples containing between 40 and 50 wt% Ni is shown in Figure 61. In looking at the behavior shown by the Fe 45 and 47.5 wt% Ni samples as shown in Figure 61, it would be expected that a composition value between these two samples would have a zero-mismatch with YSZ at room temperature upon cooling from 600 °C.

The effect of adding chromium to a Fe 50 wt% Ni sample while maintaining an iron-to-nickel ratio of one is shown in Figure 62. As was the case with mismatch upon heating, the addition of chromium increased the magnitude of mismatch between the alloy and YSZ. A 5 wt% addition of chromium nearly doubled the magnitude of mismatch with YSZ of the Fe 50 wt% Ni sample. Greater additions of chromium further increased the magnitude of mismatch at a given temperature.

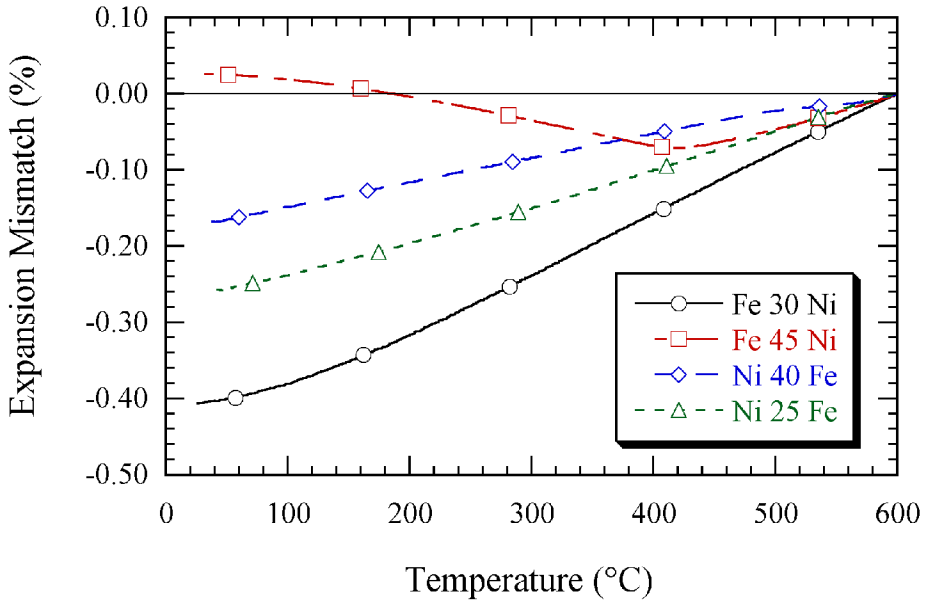

Figure 60. Expansion mismatch on cooling for Fe Ni alloys between 30 and 75 wt% Ni

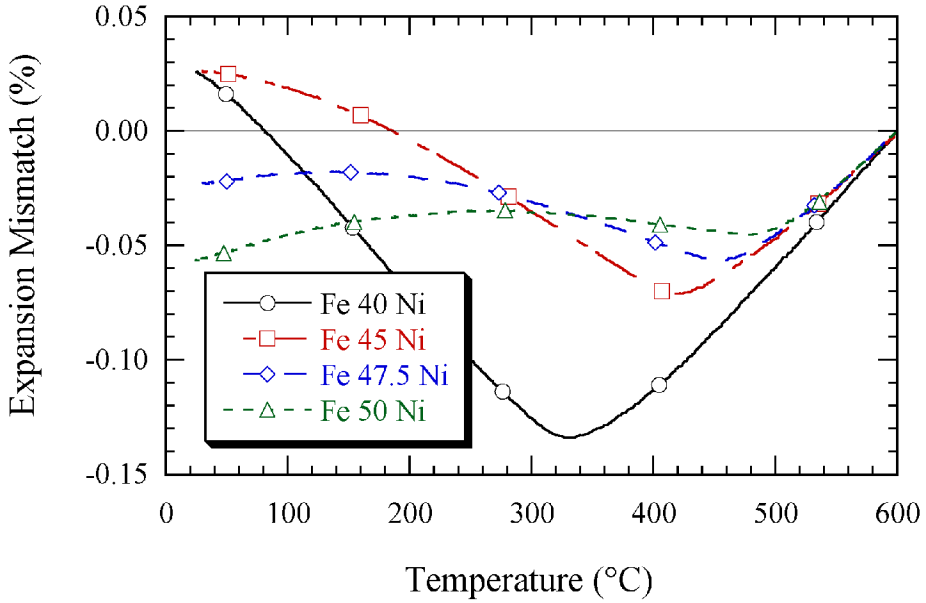

Figure 61. Expansion mismatch on cooling from 600 °C for Fe-Ni alloys between 45 and 50 wt% Ni.

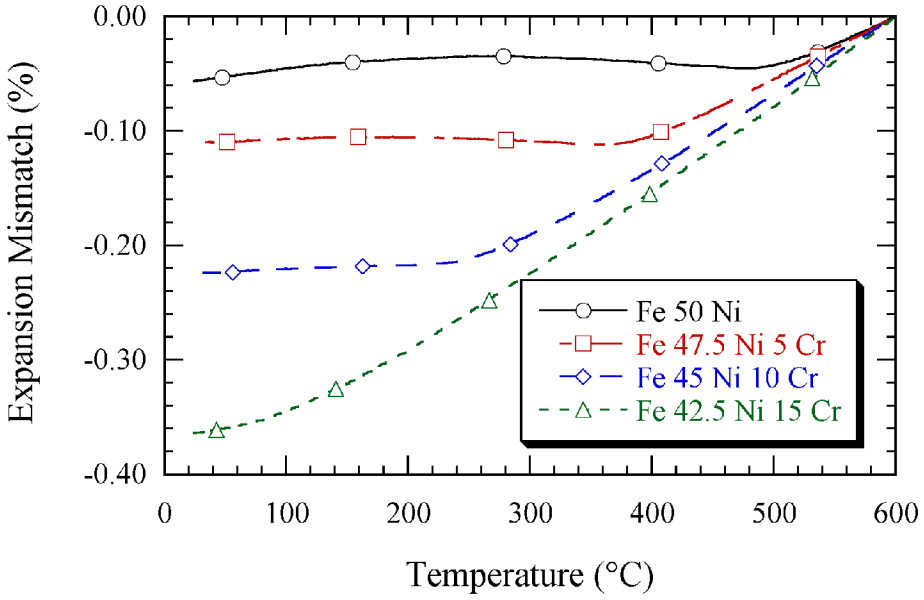

Figure 62. Expansion mismatch of Fe/Ni = 1 alloys upon cooling from 600 °C.

Thermal mismatch results of Fe-Ni-Cr alloys with 10 wt% Cr are shown in Figure 63. Changing the Fe-Ni ratio while maintaining a constant chromium content has a slight affect on mismatch values upon cooling from 600 C. In effect, this is due to the variation in the Curie temperature between the different samples. The Curie temperature was shown to decrease with higher Fe/Ni ratios (Figure 42) at a constant chromium content. Above the Curie temperature, these different alloys have similar CTE values and because of this the values of mismatch on cooling were similar. At temperatures lower than the Curie temperature, these alloys have a CTE which is nearly equivalent to that of YSZ. As a result, below the Curie temperature the mismatch values tend to become invariant with further temperature decrease.

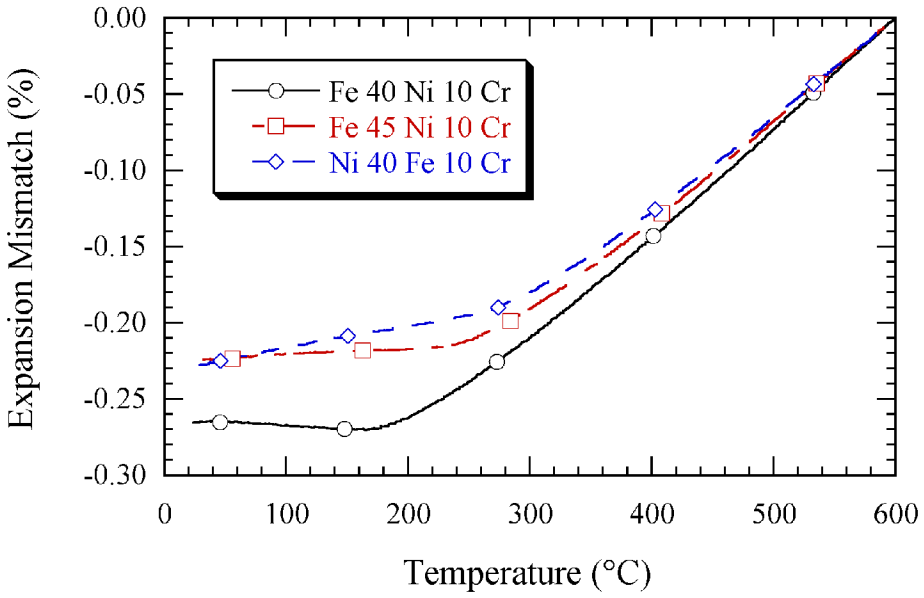

Figure 63. Expansion mismatch on cooling from 600 °C for Fe-Ni-Cr alloys with 10 wt% Cr.

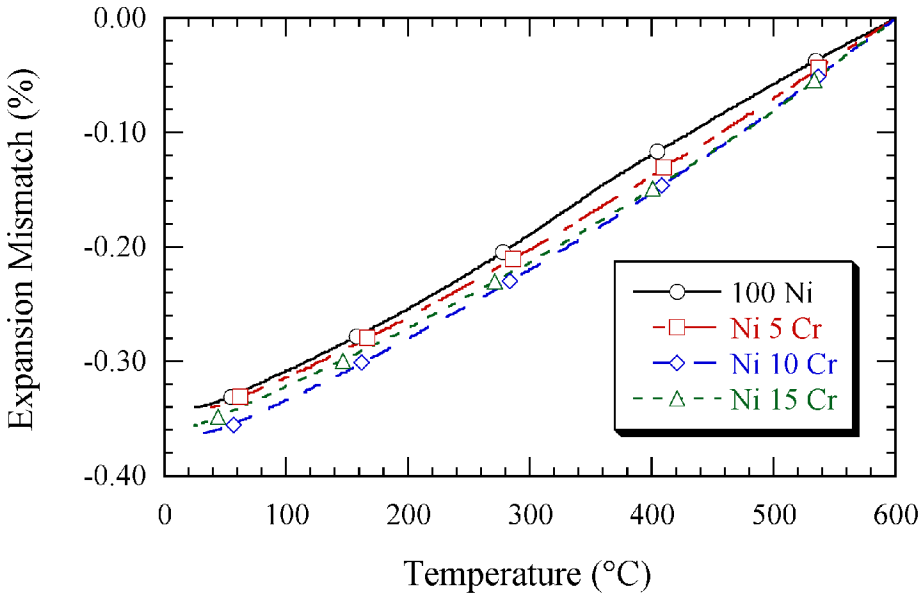

Figure 64. Expansion mismatch on cooling from 600 °C for Ni-Cr alloys.

A comparison between expansion mismatch upon cooling from 600 °C for several alloys each containing 15 wt% Cr is shown in Figure 65. This plot emphasizes the low mismatch observed from the Fe 15 wt% Cr sample. After cooling to room temperature, the Fe 15 wt% Cr had roughly one third the magnitude of expansion mismatch compared with other Fe-Ni-Cr ternary alloys with the same chromium content.

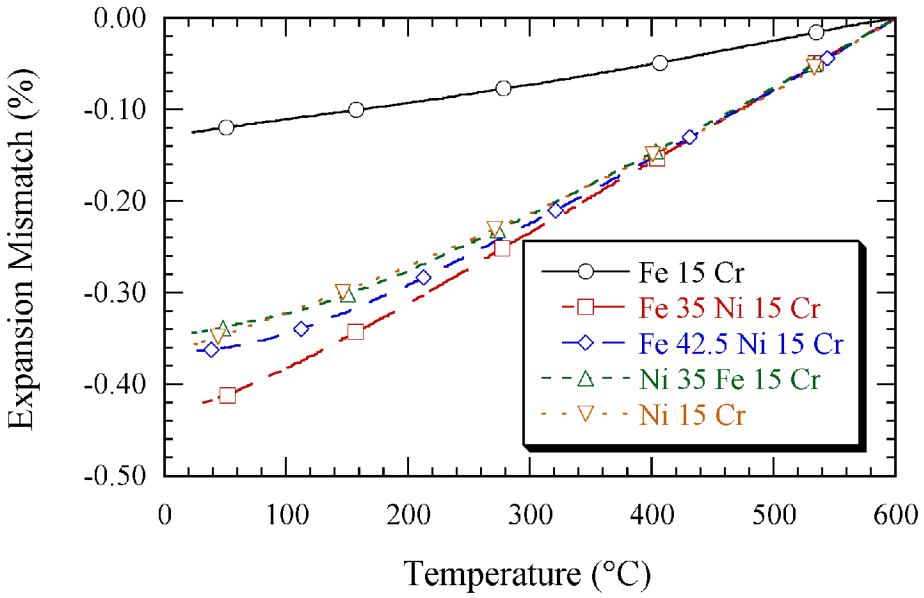

Figure 65. Expansion mismatch on cooling from 600 °C for alloys containing 15 wt% Cr

4.4.3 Cooling from 1100 °C

Calculations were also performed to understand the impact of changing the zero-stress temperature on the results for expansion mismatch upon cooling. For this case, a temperature of 1100 °C was used as the temperature below which stresses would develop upon cooling due to differences in thermal expansion between a given alloy and YSZ.

Results of expansion mismatch calculations for Fe-Cr alloys containing greater than 10 wt% Cr are shown in Figure 66. These alloys go through a Curie transformation on cooling (Figure 42) which results in a slight change in slope of the mismatch curves at the Curie temperature for the particular alloy. Similar calculations were not performed for alloys containing 10 wt% chromium or less because these alloys go through a phase transition upon cooling. The temperature at which this phase change occurs may not be identical to the temperature of the phase change upon heating. Since data was only

collected during heating, the exact phase change temperature upon cooling could not be determined and thus the calculations for these compositions were not performed.

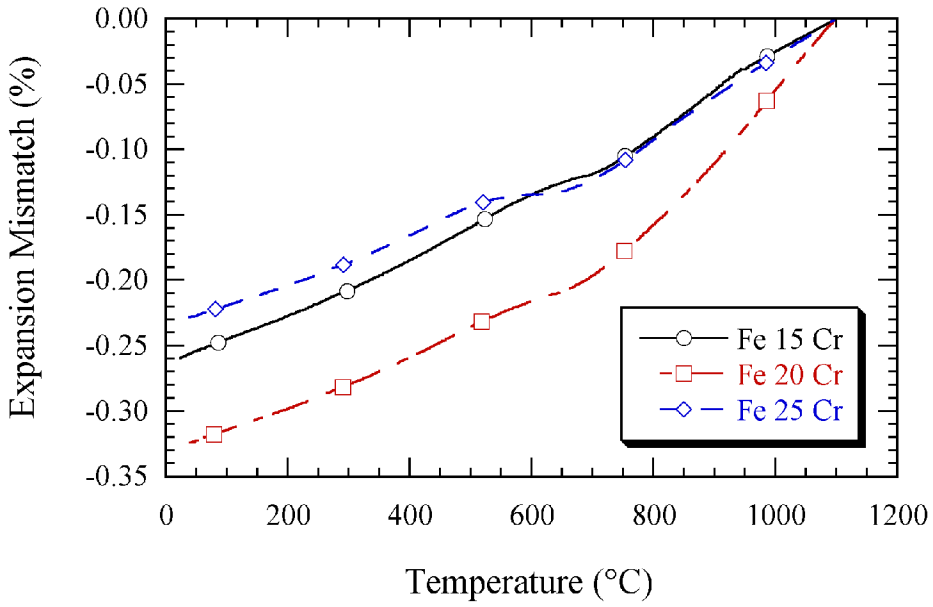

Figure 66. Expansion mismatch on cooling from 1100 °C for Fe-Cr containing 15 wt% Cr and greater.

The expansion mismatch trends within the Fe-Ni system when cooling from 1100 ° C, Figure 67, are quite similar to the trends observed for cooling from 600 °C. However, the magnitude of expansion mismatch is greater when the zero-stress temperature is increased from 600 to 1100 °C. This is also the case for the Fe-Ni alloys containing between 40 and 50 wt% Ni, Figure 68, which show a similar trend in mismatch though the magnitudes are greater.

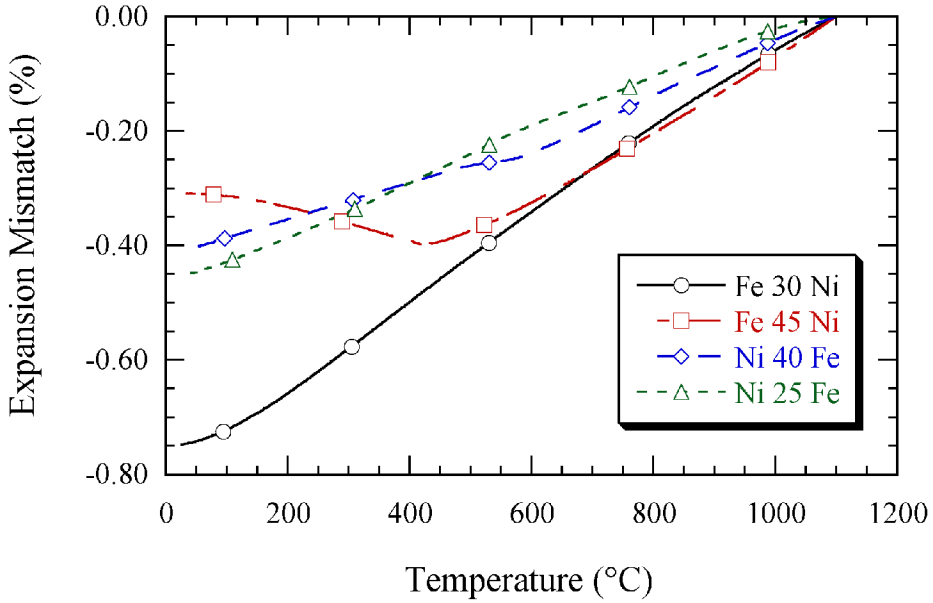

Figure 67. Expansion mismatch for Fe-Ni alloys between 30 and 75 wt% Ni.

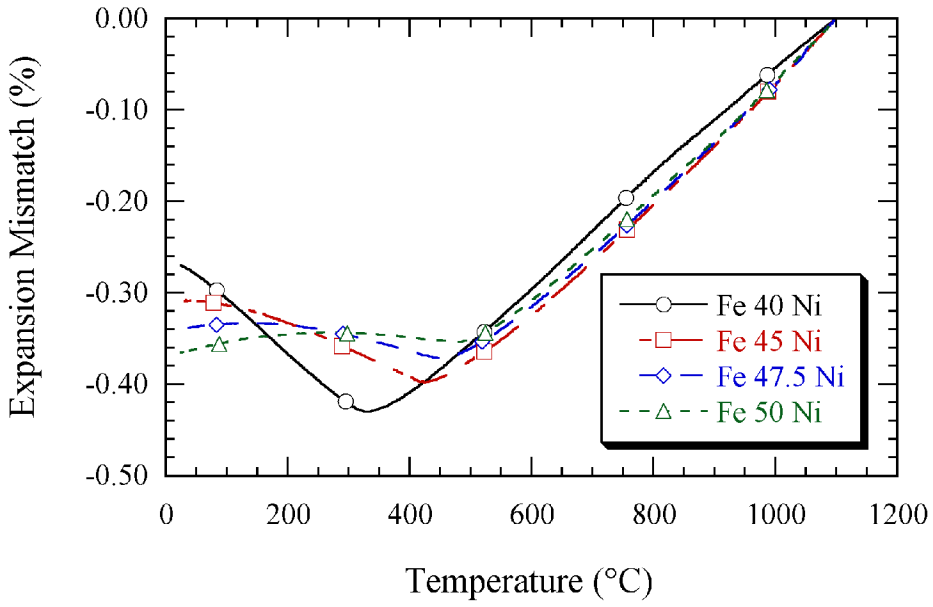

Figure 68. Expansion mismatch for Fe-Ni alloys between 40 and 50 wt% Ni

The effect of adding chromium to a Fe 50 wt% Ni sample on the expansion mismatch upon cooling from 1100 °C is shown in Figure 69. As was the case when the zero-stress temperature was assumed to be 600 °C (Figure 62), the addition of chromium tends to increase the magnitude of thermal mismatch. The mismatch values for these alloys tend to be quite similar from 1100 °C down to roughly 500 °C which is the Curie temperature of the Fe 50 wt% Ni sample. Below that point, the mismatch curve for the Fe 50 wt% Ni sample flattens out while the curves for the other alloys continue to decrease until each respective alloy reaches the Curie temperature . The Curie temperature plays an important role in determining how thermal expansion mismatch will develop for these alloys.

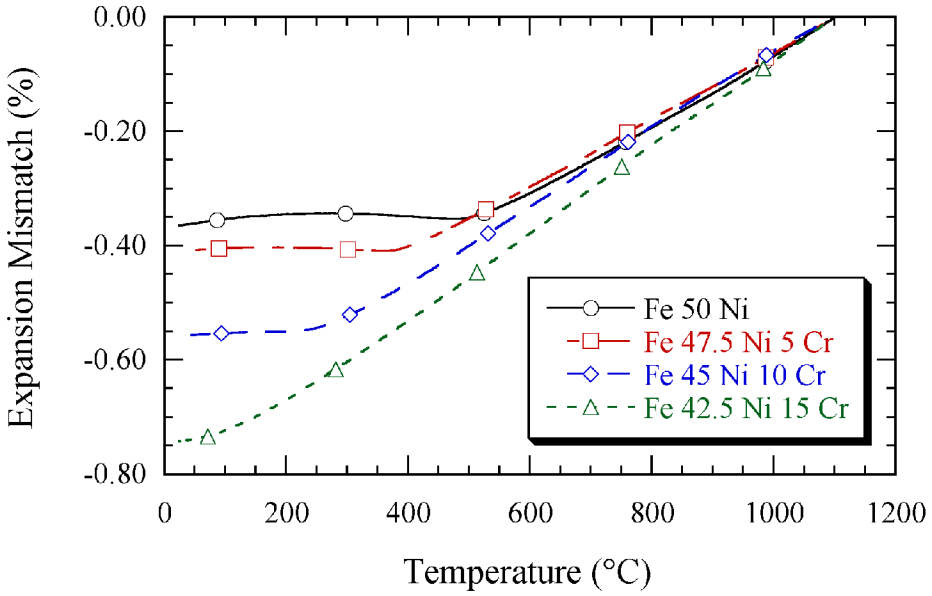

Figure 69. Expansion mismatch on cooling from 1100 °C for Fe/Ni = 1 alloys.

The expansion mismatch upon cooling from 1100 °C for three Fe-Ni-Cr alloys each with 10 wt% Cr is shown in Figure 70. The Fe/Ni ratio did not have a significant effect on

the expansion mismatch as measured for these particular alloys. The magnitude of the expansion mismatch increased linearly with decreasing temperature until ~ 250 °C which is roughly the Curie temperature for these particular alloys.

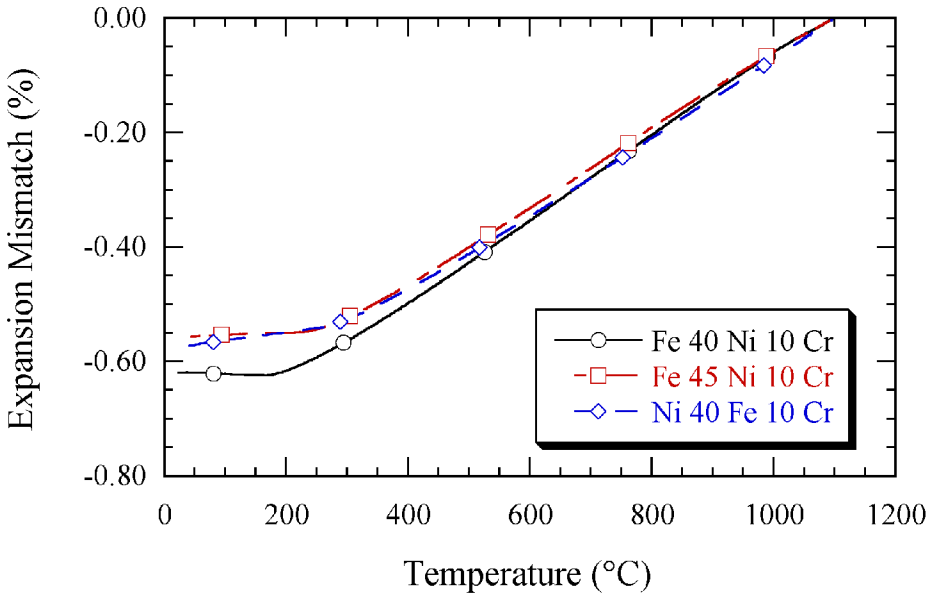

Figure 70. Expansion mismatch on cooling from 1100 °C for Fe-Ni-Cr alloys with 10 wt% Cr.

Expansion mismatch for Ni-Cr alloys upon cooling from 1100 °C is shown in Figure 71. The trends for this case were similar to those observed in Figure 64 which assumed a zero-stress temperature of 600 °C. Again, the addition of chromium to nickel increased the magnitude of expansion mismatch at a given temperature.

A plot showing the expansion mismatch for various alloys each containing 15 wt% Cr is shown in Figure 72. The Fe 15 wt% Cr sample had nearly one-third as much mismatch after cooling from 1100 °C to room temperature as compared with other alloys containing the same chromium content.

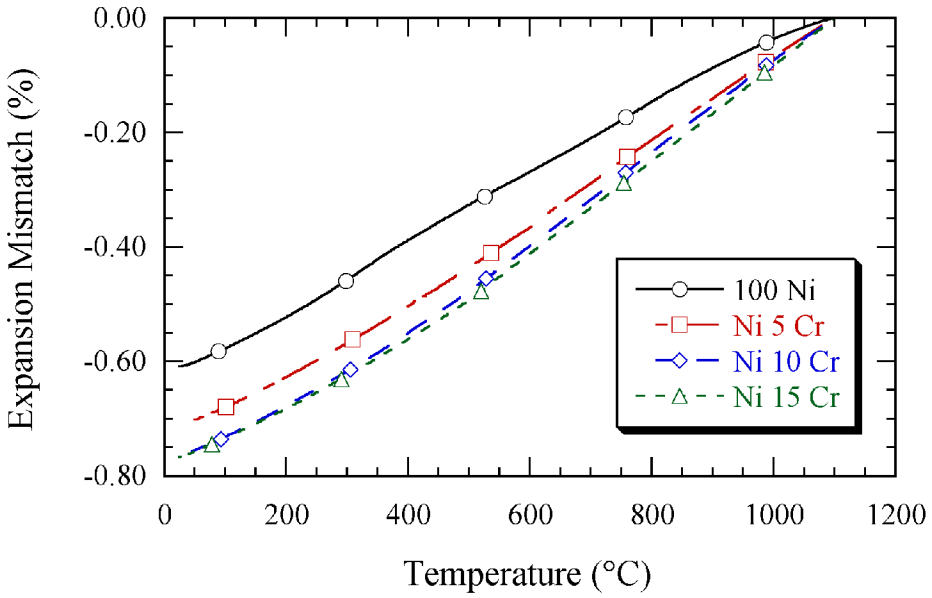

Figure 71. Expansion mismatch on cooling from 1100 °C for Ni-Cr alloys.

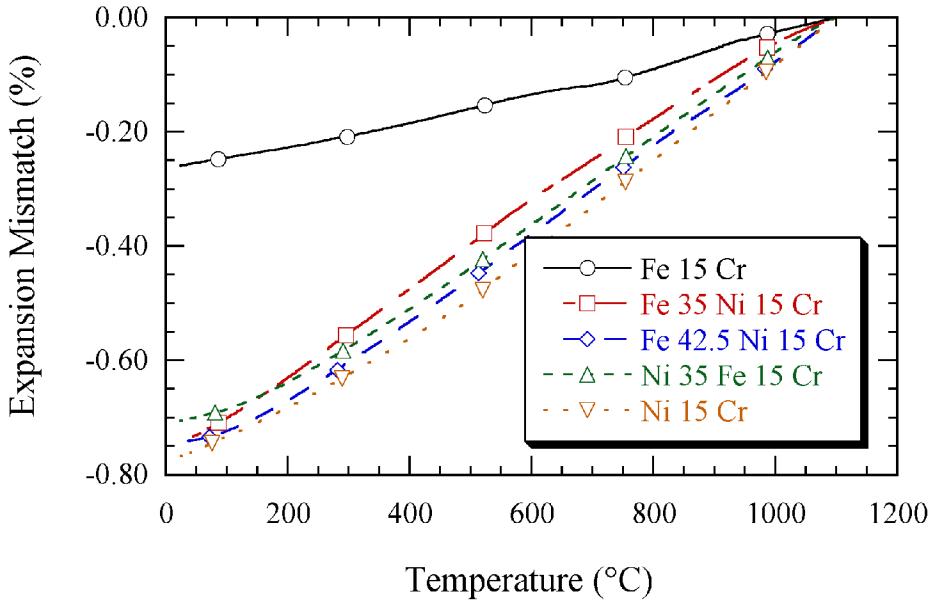

Figure 72. Expansion mismatch on cooling from 1100 °C for alloys containing 15 wt% Cr.

4.4.4 Selection of the Zero-Stress Temperature

At some point during cooling from the reduction/sintering heat-treatment, a last stress-free state temperature between the YSZ and the metal is assumed. If the cooling rate from the processing temperature were sufficiently slow to allow for plastic flow, the zero-stress temperature could reasonably assumed to be on the order of 0.4 to 0.5 of the absolute melting temperature (T_M) [56]. This ratio is generally considered the temperature above which stress relaxation, creep, and other thermally-activated processes can occur. Iron-nickel alloys with between 40 and 50 wt% Ni have melting temperatures in the range of 1725 to 1775 K. Thus a zero-stress temperature was estimated to be 600 °C. Figure 73 shows that the hardness of cold-worked nickel decreases abruptly at roughly 600 °C [57] which is roughly half of the absolute melting temperature. If, on the other hand, the cooling rate from the processing temperature (~ 1200 °C) were not sufficiently slow to allow for plastic flow, the zero-stress temperature could be much higher than 600 °C. For this case, 1100 °C was used as the zero-stress temperature.

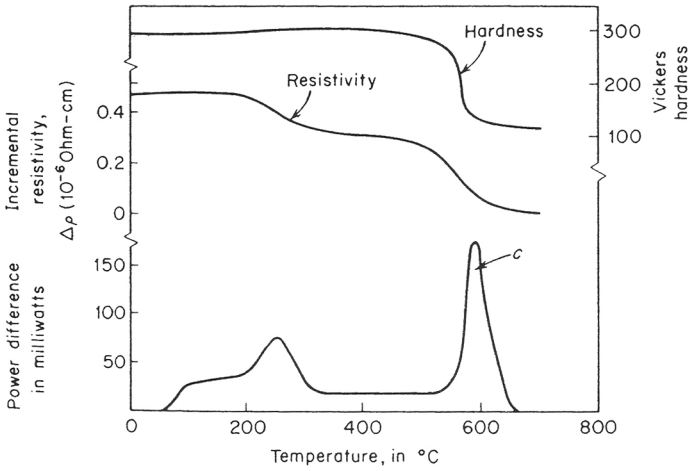

Figure 73. Anisothermal-anneal curve for cold-worked nickel [57].

The selection of the zero-stress temperature is critical because a change in this value could lead to different materials exhibiting superior mismatch values. Several materials in particular have been shown to have low thermal mismatch with YSZ under different heating and cooling conditions, specifically, Fe 47.5 Ni 5 Cr, Fe 47.5 Ni, and Fe 20 Cr. Figures 74, 75, and 76 show the expansion mismatch for each alloy, respectively, for each assumed heating and cooling condition. The alloys are compared against one another for each zero-stress temperature assumption in Figures 77 - 79. These plots emphasize the importance of clearly defining the zero-stress temperature and other criteria used for material selection. It may be desired for the interconnect to have a minimal amount of thermal mismatch upon heating from room temperature to 400 °C. In this case, the Fe 47.5 wt% Ni 5 wt% Cr alloy would be the best material candidate because it would have zero-mismatch with YSZ after heating to 400 °C. If the criteria were changed to state that a minimum amount of mismatch when heating from room temperature to 800 °C were desired, the Fe 47.5 wt% Ni material would be superior. Or, if the criteria were that mismatch should be minimized when cooling from 1100 °C to 400 °C, the Fe 20 wt% Cr material would offer the best performance.

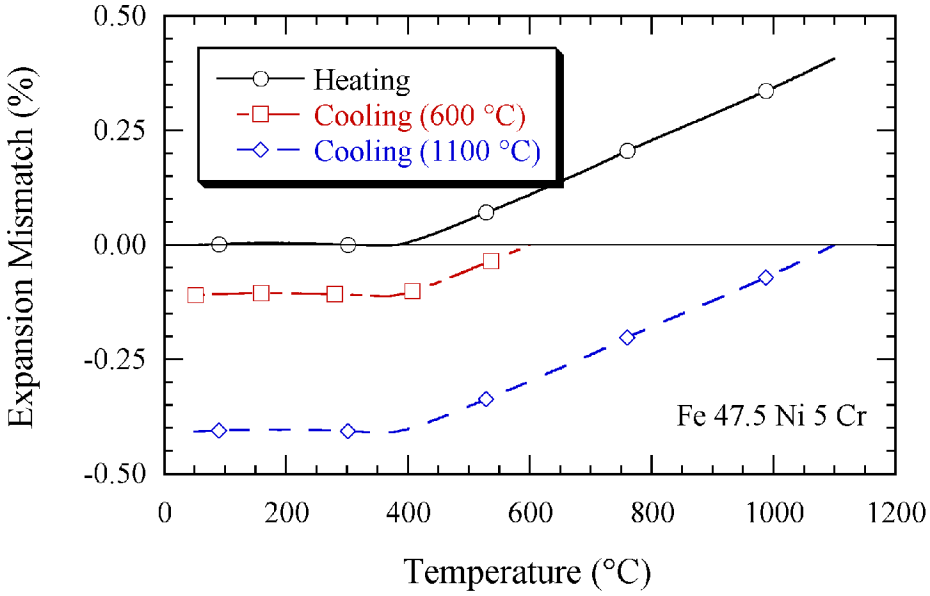

Figure 74. Expansion mismatch for Fe 47.5 wt% Ni 5 wt% Cr.

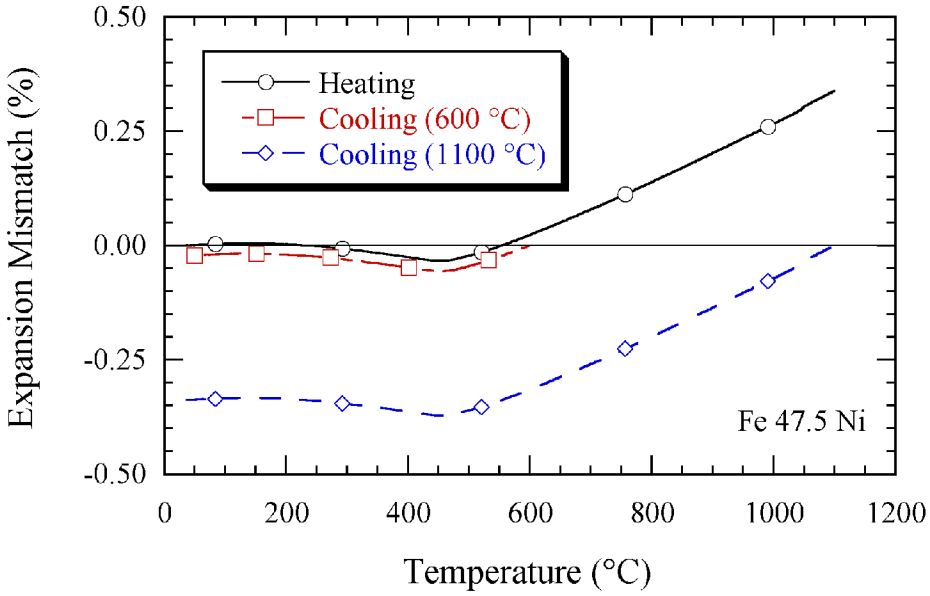

Figure 75. Expansion mismatch for Fe 47.5 wt% Ni.

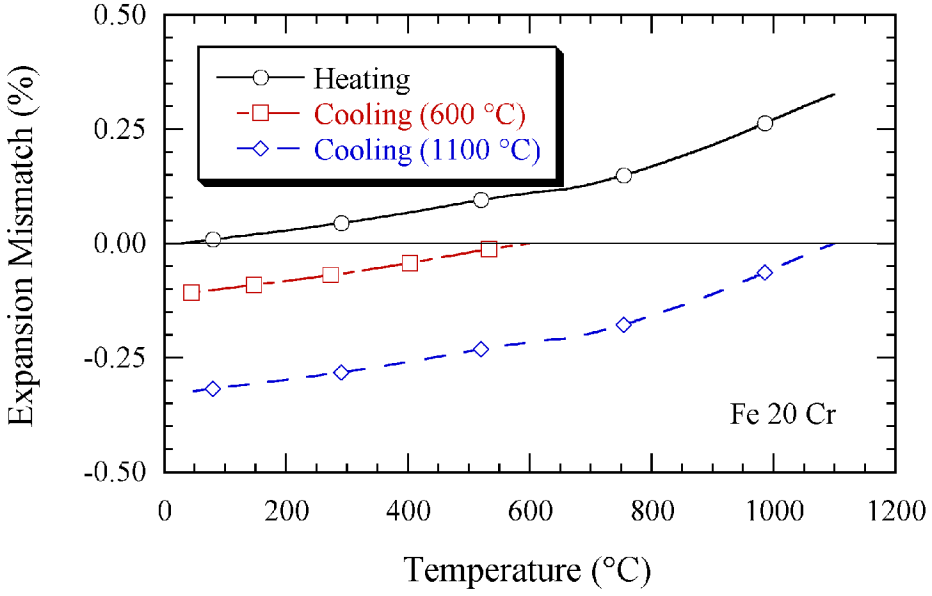

Figure 76. Expansion mismatch for Fe 20 wt% Cr.

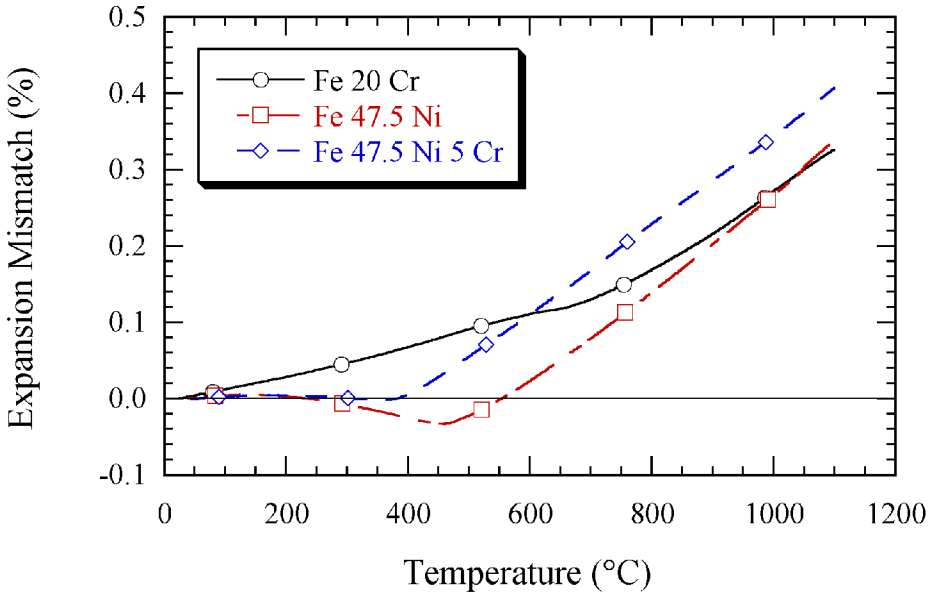

Figure 77. Expansion mismatch on heating for Fe 20 Cr, Fe 47.5 Ni and Fe 47.5 Ni 5 Cr.

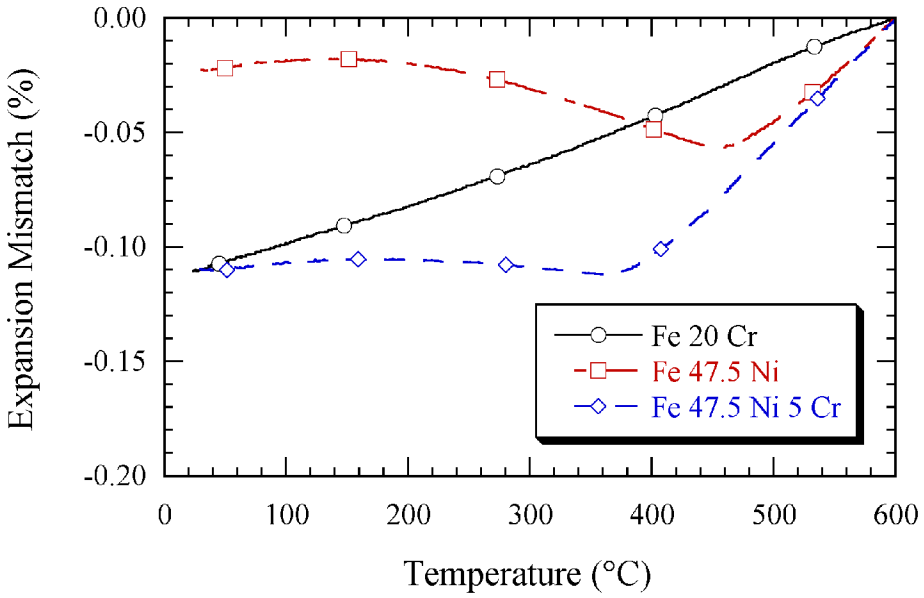

Figure 78. Expansion mismatch on cooling from 600 °C for Fe 20 Cr, Fe 47.5 Ni and Fe 47.5 Ni 5 Cr.

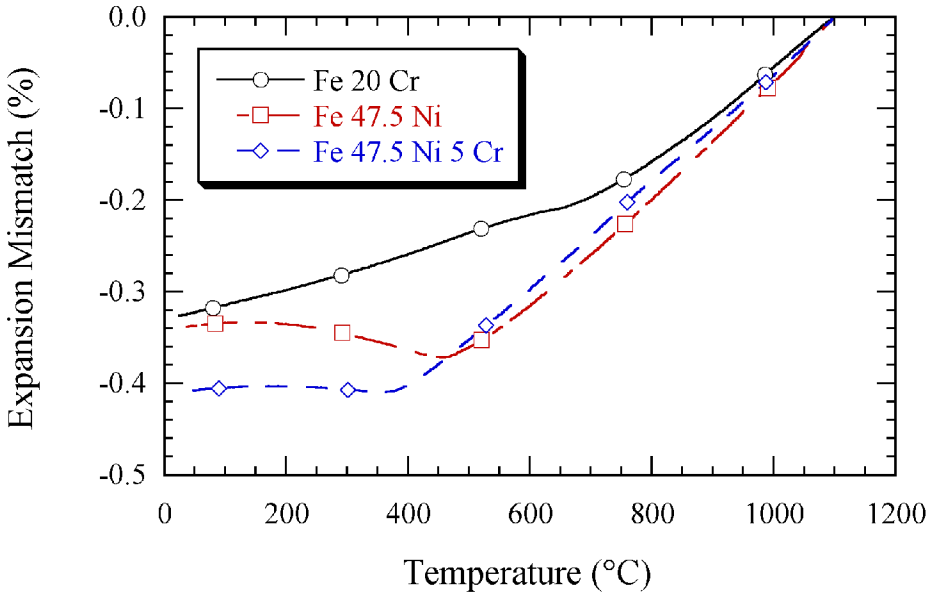

Figure 79. Expansion mismatch on cooling from 1100 °C for Fe 20 Cr, Fe 47.5 Ni and Fe 47.5 Ni 5 Cr.

The zero-stress temperature is a critical parameter that must be taken into account when selecting a metal alloy for use as an interconnect. An additional complication is the zero-stress temperature would likely be dependent on alloy composition, making the determination of a zero-stress temperature for one alloy meaningless for another alloy. In addition to understanding the thermal expansion behavior of alloys within these various systems, it would likely be necessary to understand the variation in zero-stress temperatures for the same alloys before an interconnect alloy could be selected.

4.4 Oxidation

Oxidation tests were performed using a resistance box furnace in static air as described in the experimental procedure. Rectangular strip samples were placed in the pre-heated furnace and removed at periodic intervals for weight measurements to provide weight gain versus time-at-temperature data. All samples discussed here, with the exception of XRD and microscopy samples, were oxidized during one experiment with the intention of providing a direct comparison between these particular alloys and to ascertain trends.

Weight gain versus time results for Fe-Cr alloys are shown in Figures 80 and 81. This system is the classic example of the benefits of adding certain elements to an otherwise oxidation-prone metal to improve the oxidation resistance. The pure iron sample experiences rapid weight gain in air at 700 °C. The sample showed signs of spallation as early as 3 hours into the oxidation test; after 22 hours at temperature, the spalling became too severe to allow for continued data collection.

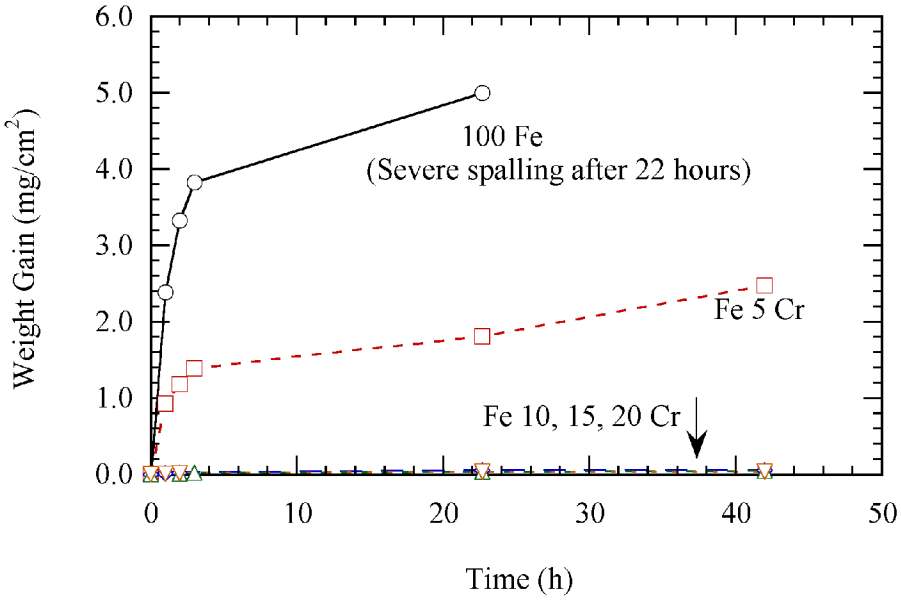

Figure 80. Oxidation of Fe-Cr alloys at 700 °C in air. Alloys with 10, 15, and 20 wt% Cr are also shown in Figure 81.

Additions of chromium to iron have the expected effect of reducing the oxidation of the alloy. The impact is particularly noticeable for the alloys containing 10 wt% Cr and greater. For these samples, weight gain after a given amount of time at temperature was roughly two-orders of magnitudes less than for the pure iron. Additional chromium additions above 10 wt% Cr also resulted in a decrease in oxidation, through the relative impact of the chromium addition tended to drop off at higher concentrations.

Chromium reduced oxidation of the base Fe-Cr alloy by producing a dense, adherent layer of Cr_2O_3 on the surface of the alloy [11]. The chromia layer acts a a diffusion barrier which slows the diffusion of oxygen from the atmosphere and thus slows the reaction between oxygen and the base alloy. It is often stated that a Fe-Cr alloy should contain 12 wt% Cr or more to sufficiently protect the base alloy from corrosion [17]. For the case studied here (static air at 700 °C) 10 wt% Cr appears to be sufficient.

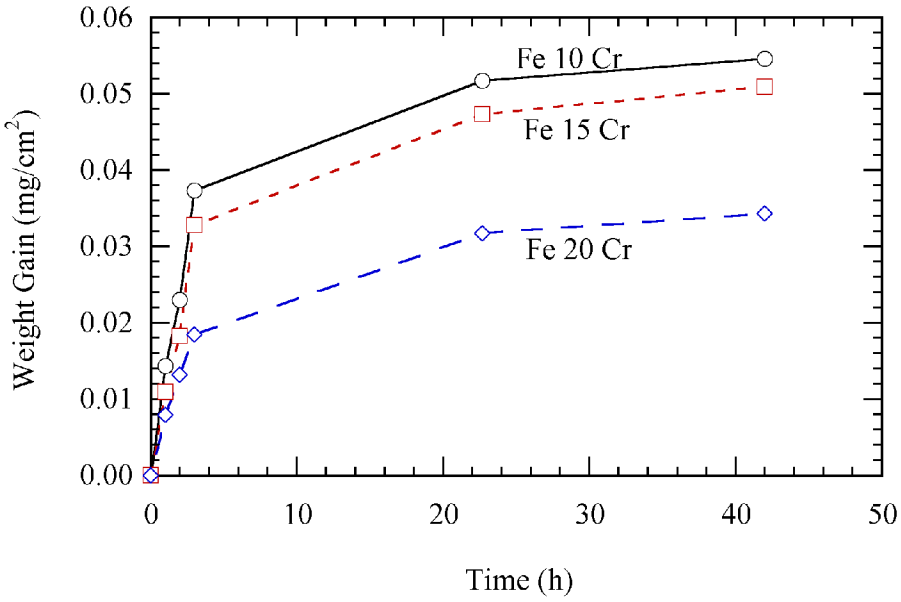

Figure 81. Oxidation of Fe 10, 15, and 20 wt% Cr alloys in static air at 700 °C.

Additions of chromium to a Fe-Ni alloy did not result in such dramatic reductions in weight gain as was observed in the Fe-Cr binary samples. Starting with a Fe 50 Wt% Ni alloy, chromium was added in 5 wt% increments while maintaining a Fe/NI ratio of one. The oxidation results for these samples are given in Figure 82 and show that chromium improved oxidation resistance under the experimental conditions but only by a relatively small amount compared to the Fe-Cr binary samples in Figures 80 and 81.

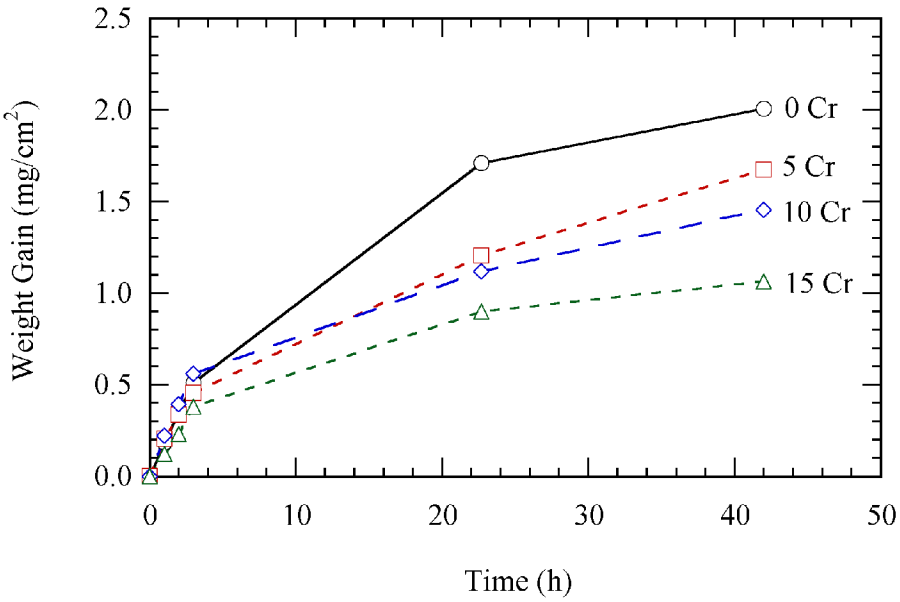

Figure 82. Oxidation of Fe-Ni-Cr alloys with Fe/Ni = 1.

Chromium additions to the Fe 50 wt% Ni base alloy were also made using two other methods, one maintaining 50 wt% Fe and the other maintaining 50 wt% Ni (constant Fe and constant Ni, respectively) in the alloy. Oxidation results for these Fe-Ni-Cr samples are shown in Figures 83 and 84. The general trends are quite similar to the Fe/Ni = 1 samples shown in Figure 82 where the chromium addition was found to improve oxidation resistance but the beneficial effect of chromium was not as significant as in the case of Fe-Cr samples.

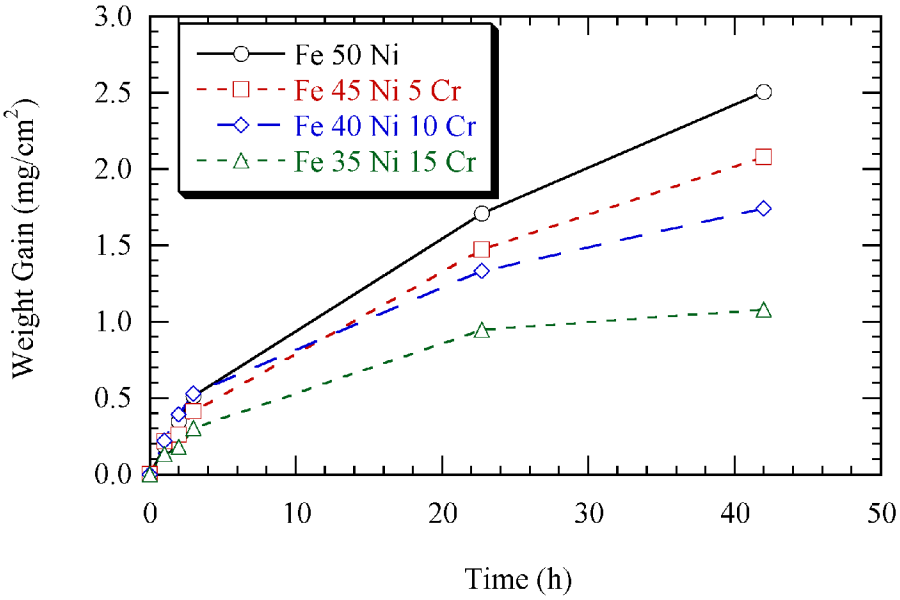

Figure 83. Oxidation of Fe-Ni-Cr samples with constant Fe content.

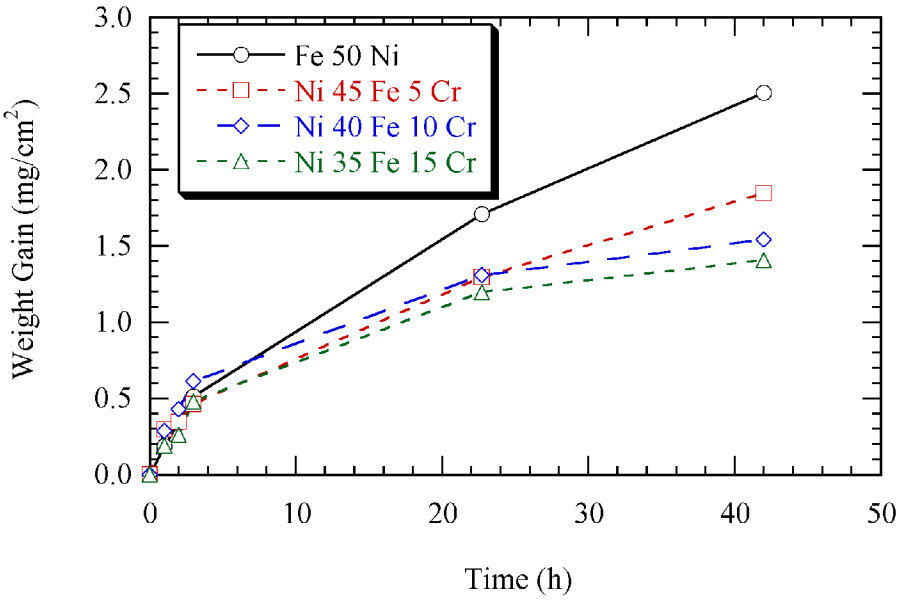

Figure 84. Oxidation of Fe-Ni-Cr samples with constant Ni content.

A comparison of oxidation behavior between several samples, each containing 15 wt% Cr, is shown in Figure 85. This plot shows the superior performance of the Fe-Cr

binary sample compared to the Fe-Ni-Cr samples. The weight gain after 42 hours for the Fe 15 wt% Cr sample was roughly 15 times less than the ternary Fe-Ni-Cr samples with the same chromium content.

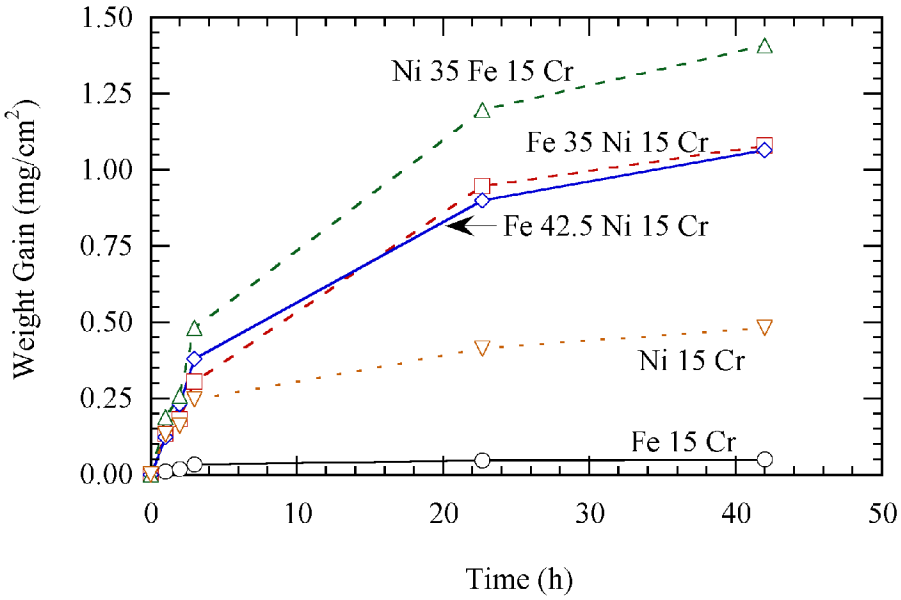

Figure 85. Oxidation of alloys containing 15 wt% Cr.

Additions of $Ca(OH)_2$ were made to a base oxide mixture of Fe 47.5 Ni 5 Cr prior to the paste processing stage. The $Ca(OH)_2$ readily oxidizes upon heating, even when heated in the hydrogen atmosphere used for reduction heat-treatment of the oxide samples, to form calcium oxide. These particular samples were reduced in the as-extruded condition; the resulting material would be expected to be a metal matrix with discrete CaO particles located on grain boundaries. The effect of CaO additions to a Fe 47.5 wt% Ni 5 wt% Cr alloy on the oxidation of the alloy in air are shown in Figure 86. Calcium oxide additions had a beneficial effect on the oxidation resistance of this Fe-Ni-Cr alloy. An addition of 0.5 wt% CaO lowered the weight gain due to oxidation by roughly 50%

compared with the same base alloy with no CaO. Increasing the amount of CaO added to the alloy further improved the oxidation resistance. Figure 87 shows the total weight gain after 22.7 hours at 700 °C as a function of CaO addition to the Fe 47.5 wt% Ni 5 wt% Cr alloy. The impact of CaO on the oxidation of the alloy tapered off for CaO contents greater than 2 wt%. It should be noted that the sample containing 5 wt% CaO formed a glassy-like coating on the top surface of the strip during the reduction heat-treatment and because of this, the oxidation result are suspect.

The addition of CaO to the Fe 47.5 wt% Ni 5 wt% Cr alloy was shown to increase porosity levels after reduction heat-treatment (Table 8). The increase in porosity would likely cause changes to other material properties such as strength, ductility, and conductivity. However, the thermal expansion behavior was shown to be invariant with a calcium oxide addition. That being the case, the addition of CaO could be used to provide slight improvements in oxidation resistance of the Fe 47.5 wt% Ni 5 wt% Cr alloy without affecting thermal expansion behavior of the material.

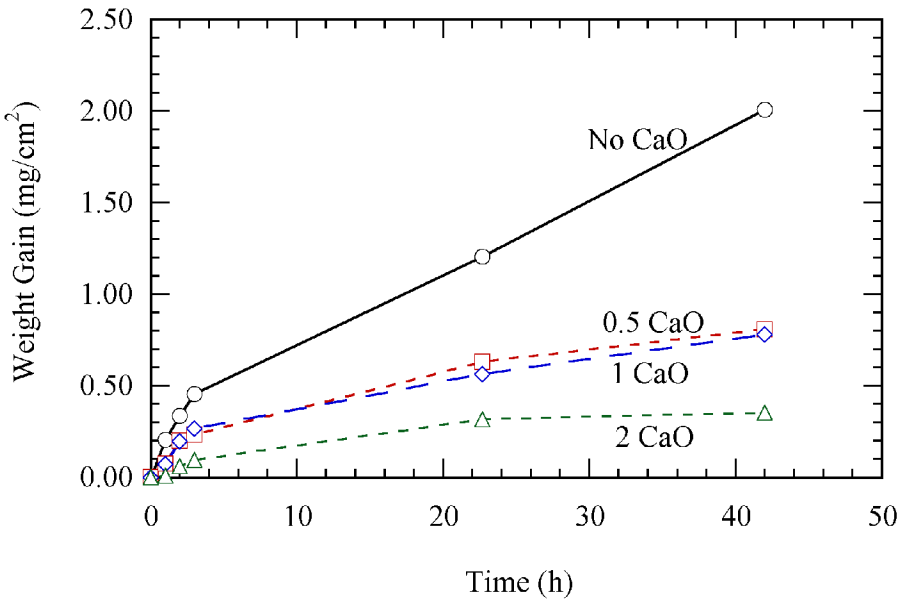

Figure 86. Oxidation of Fe 47.5 Ni 5 Cr base alloys with CaO addition.

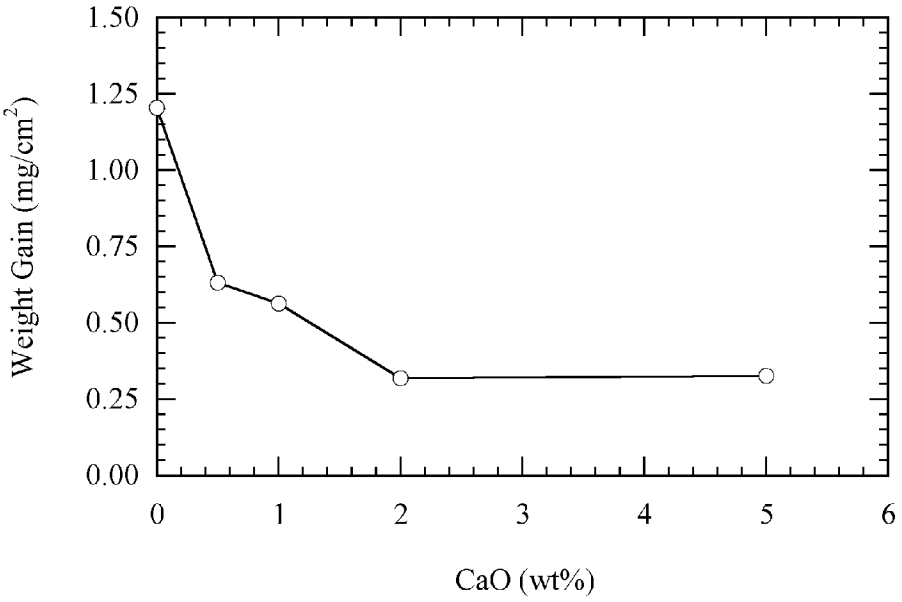

Figure 87. Total weight gain of Fe 47.5 Ni 5 Cr base alloys after 22.7 h in air at 700 °C.

The effect of another oxide addition, yttrium oxide, on the oxidation resistance of a Fe-Ni-Cr alloy is shown in Figure 88. In this case, the base alloy was Fe 39 wt% Ni 8 wt% Cr and the effect of a 0.5 wt% Y_2O_3 addition was observed. The results were quite similar to the effect of CaO shown in Figures 87 and 88; the 0.5 wt% Y_2O_3 addition lowered the weight gain after a given amount of time by roughly 50 % compared with the same base alloy with no oxide addition.

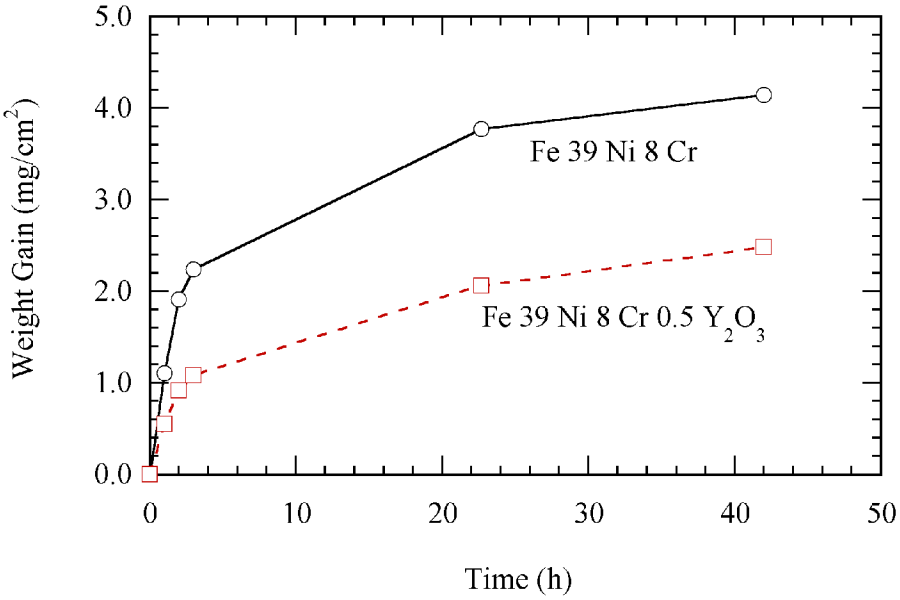

Figure 88. Oxidation of Fe 39 Ni 8 Cr base alloy with and without yttria addition.

A sample of Ni 40 wt% Fe 10 wt% Cr was oxidized in air at 700 C for 24 hours and then prepared for SEM analysis. A SEM micrograph of the oxidation layer is shown in Figure 89 (A). This oxidation layer was similar to others observed from Fe-Ni-Cr alloys of different compositions, although thickness varied with Cr content. Line-scans of the oxidation layer, Figure 89 (B - E), indicated that the surface region of the scale was rich in iron, nickel, and oxygen. An area closer to the base metal was found to have a higher concentration of chromium and oxygen with relatively small amounts of iron and chromium. This indicates that a chromia layer may be forming beneath an initial Fe,Ni-based oxide. Further experimentation is needed to fully understand the process by which the oxidation layer forms as a function of time in these alloys.

X-ray diffraction data were taken from Fe-Ni-Cr alloys after each had been oxidized in air at 700 °C for 24 hours to identify the oxide phases present in the respective

oxidation layers. The full scans for the 5, 10, and 15 wt% Cr samples with Fe/Ni = 1 are shown in Figures 90, 91, and 92, respectively. The phases detected in the oxide layers were $NiFe_2O_4$ and Fe_2O_3. It should be noted that the XRD pattern for Cr_2O_3 is similar to Fe_2O_3 allowing for the possibility that Cr_2O_3 could potentially be present in the oxidation layers. Diffraction peaks associated with the base Fe,Ni alloy were easily visible in the 15 wt% Cr sample indicating that that layer was relatively thin. The peak intensity of the base Fe,Ni alloy tended to decrease with decreasing chromium content which indicated that the oxide layer of the lower chromium containing samples was thicker compared to samples with higher chromium additions.

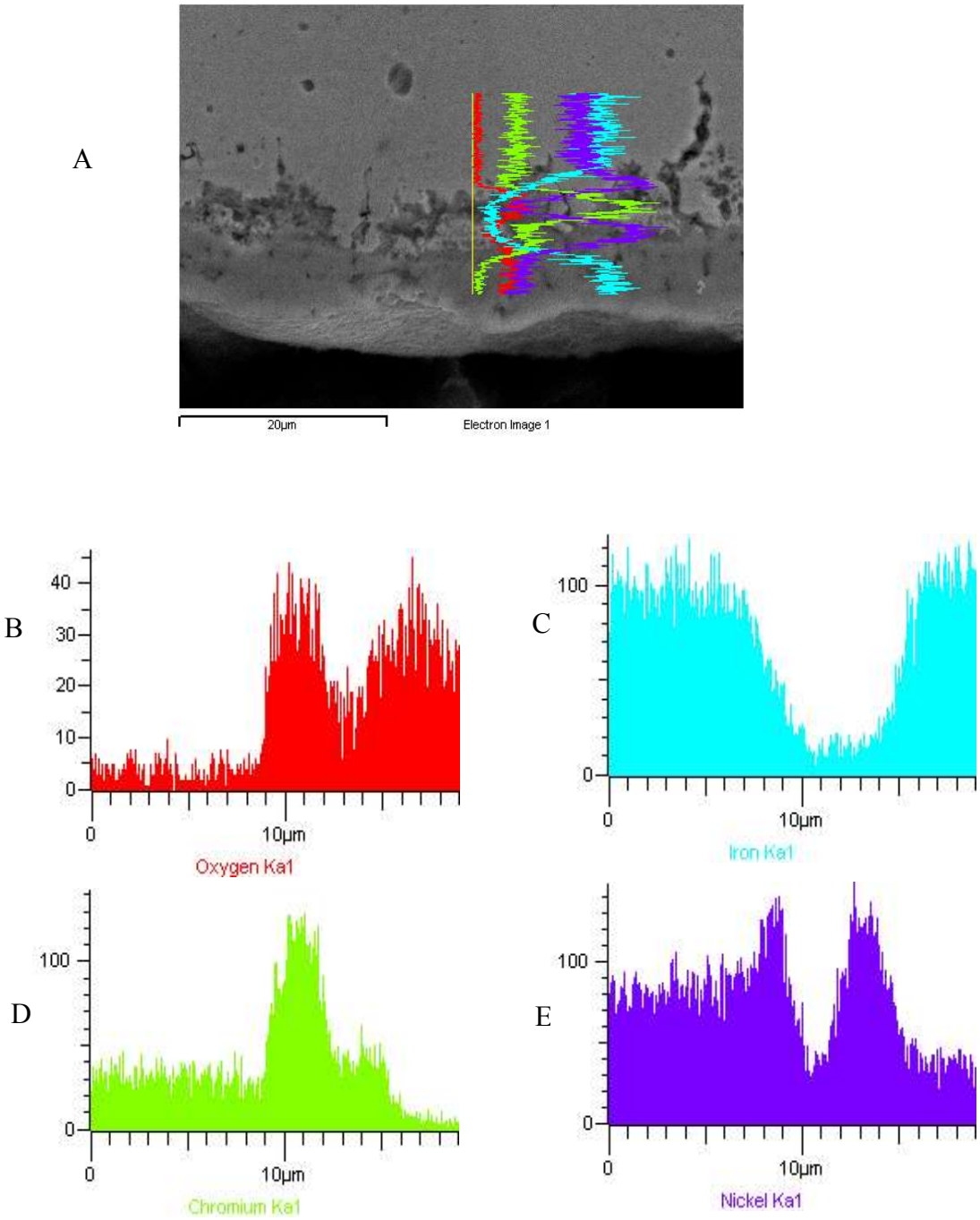

Figure 89. SEM image (A) and EDS line-scans for oxygen (B), iron (C), chromium (D), and nickel (E) of Ni 40 Fe 10 Cr after oxidation in air at 700 °C for 24 h.

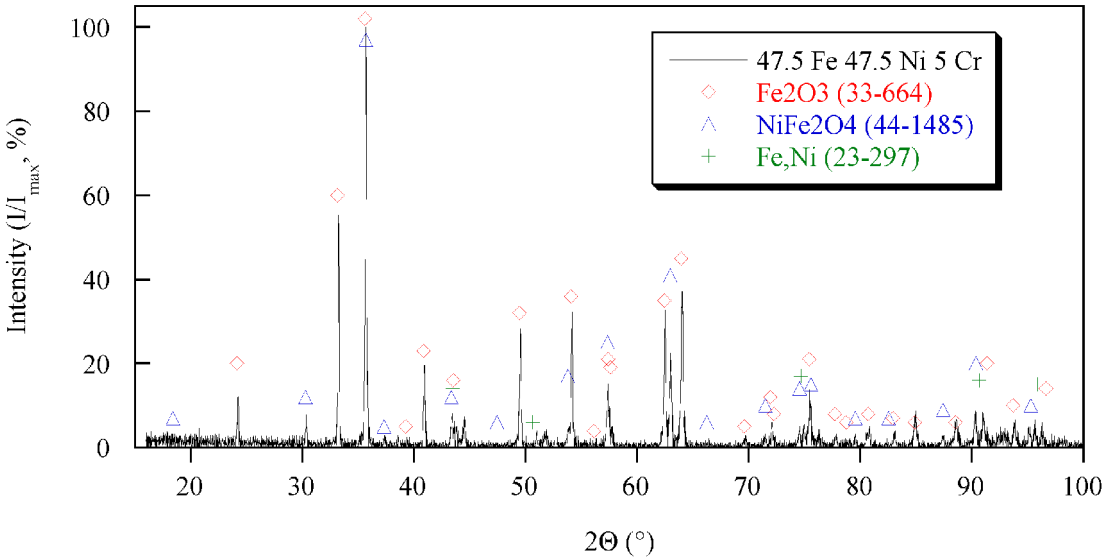

Figure 90. XRD pattern from Fe 47.5 Ni 5 Cr oxidized at 700 °C for 24 h in air.

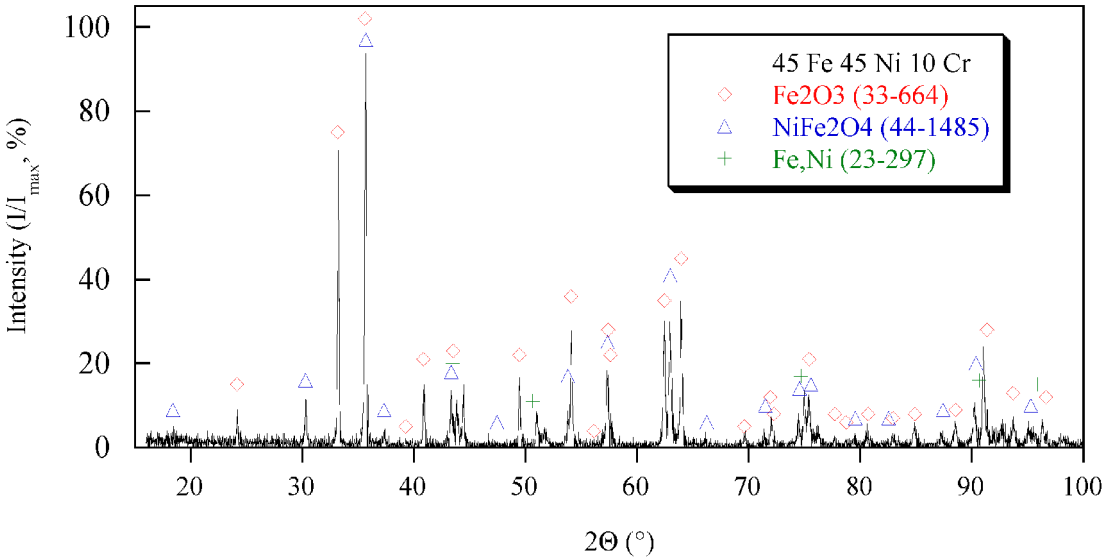

Figure 91. XRD pattern from Fe 45 Ni 10 Cr oxidized at 700 °C for 24 h in air.

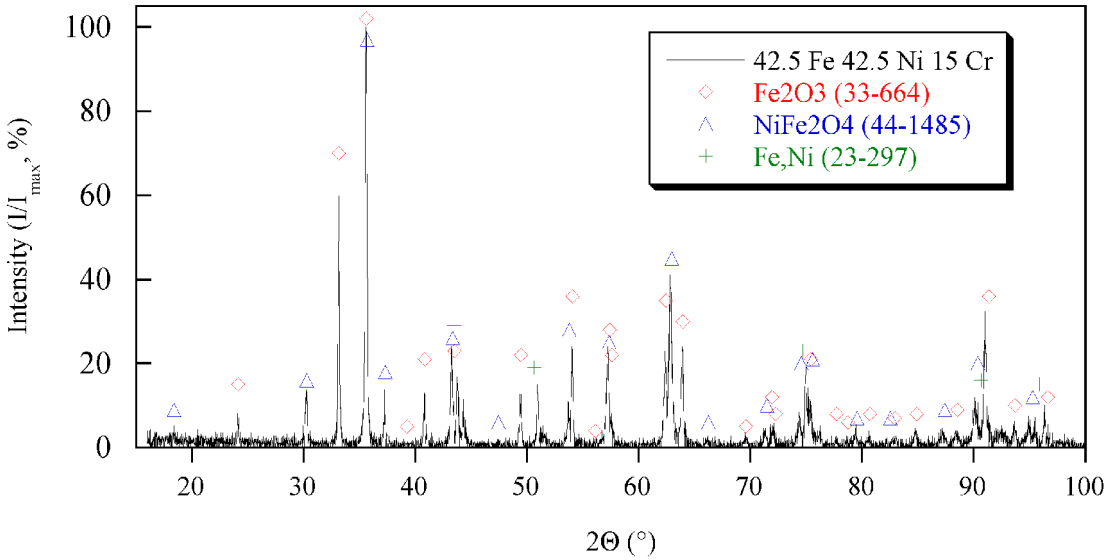

Figure 92. XRD pattern from Fe 42.5 Ni 15 Cr oxidized at 700 °C for 24 h in air.

Closer observation of certain specific peaks from the diffraction patterns of the Fe-Ni-Cr samples with a constant 15 wt% chromium content reveals additional information. As shown in Figure 93, the relative peak intensity for the $NiFe_2O_4$ (220) peak increased with increasing nickel content. Also, the relative intensity of the Fe_2O_3 (104) peak, Figure 94, increased with increasing iron content. Thus, changes to the Fe/Ni ratio affect the relative amounts of nickel- or iron-containing oxides found in the oxidation layer of the alloys.

While this work was not significantly detailed to provide accurate oxidation rate constants or activation energies, it clearly demonstrated that Fe-Cr binary alloys containing 10 wt% Cr or greater offer far superior oxidation resistance in air at 700 °C compared with Fe-Ni-Cr ternary samples. It was shown that small additions of oxides (CaO or Y_2O_3) made to a Fe-Ni-Cr ternary alloy improve the oxidation resistance of the material without changing the thermal expansion behavior of the alloy. The ability to improve the oxidation

resistance without affecting thermal expansion would likely be beneficial to an alloy used as a SOFC interconnect. In addition, improving the oxidation resistance without adding additional chromium to the alloy would likely reduce chromia poisoning of the electrode materials during the operation of the SOFC. However, additional research is needed to better understand the impact of oxide additions to these Fe-Ni-Cr alloys.

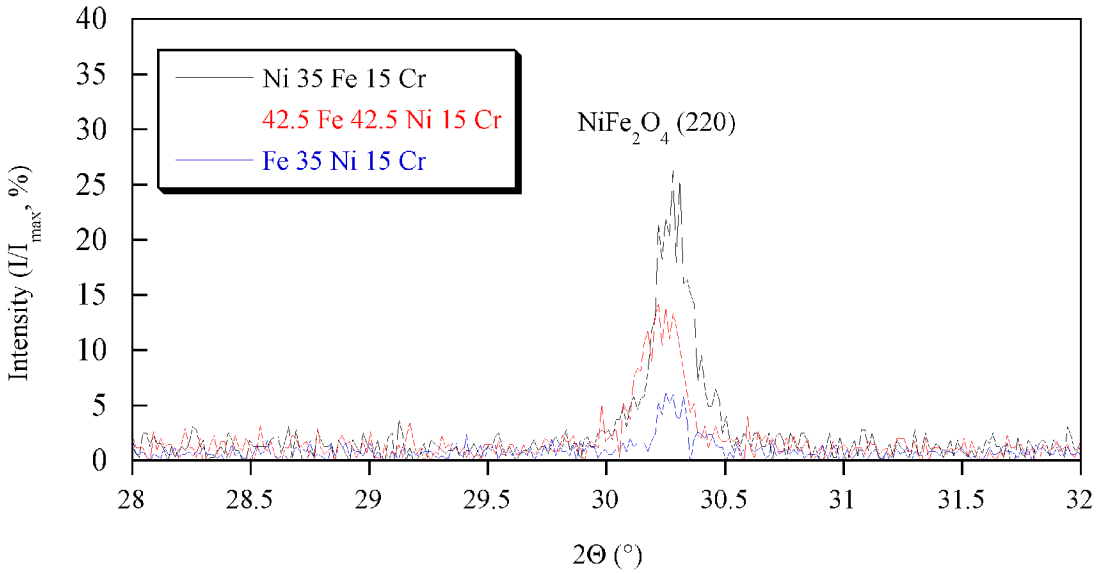

Figure 93. Detail of $NiFe_2O_4$ (220) peak from Fe-Ni-Cr samples containing 15 wt% Cr after oxidation at 700 °C for 24 h in air.

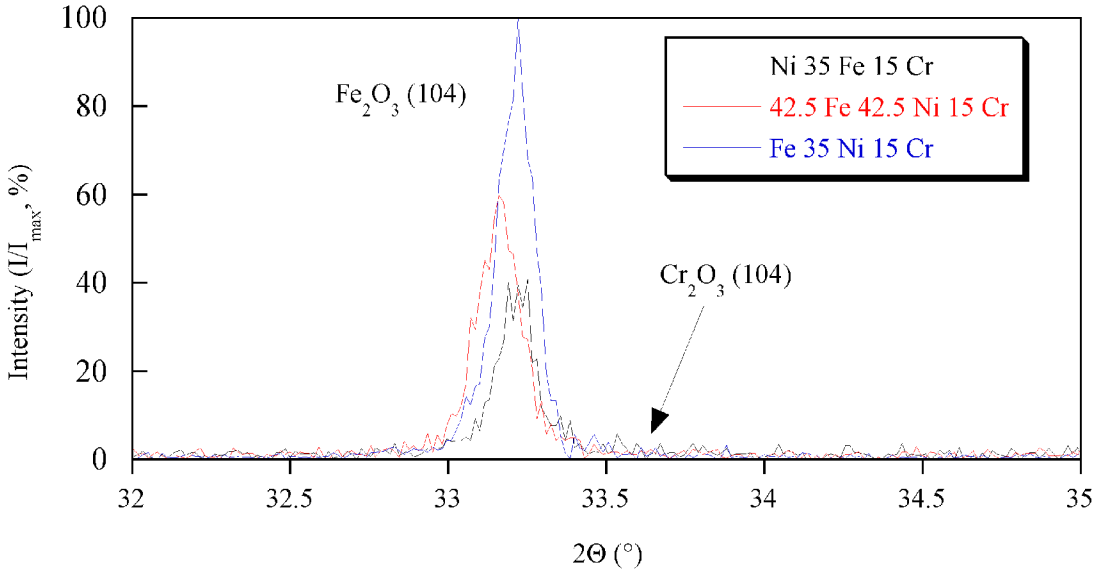

Figure 94. Detail of Fe_2O_3 (104) peak from Fe-Ni-Cr samples containing 15 wt% Cr after oxidation at 700 °C for 24 h in air.

4.6 Mechanical Properties

The issue of mechanical properties is largely absent from the discussion of desired SOFC interconnect properties in the literature. For the case of the hybrid SOFC structure, mechanical properties of the interconnect should satisfy several requirements. First, the metal alloy should yield at a lower stress than YSZ; it is desirable for the metal component to deform rather than the electrolyte to fracture. Second, the metal should exhibit significant ductility. While no exact minimum elongation value can be specified at this time, a general statement would be that the metal alloy should have more than 10% elongation prior to fracture.

A brief experiment was performed to provide basic information regarding the mechanical properties of select Fe-Ni-Cr alloys. Four compositions were selected and standard room-temperature tensile tests performed. As outlined in the Experimental

Procedure, these tensile specimens were in the form of flat dog-bones, cut in the the green state prior to reduction. For each composition, seven tensile tests were performed and the averaged results are shown in Table 12. An example of a single stress / strain curve is shown in Figure 95.

Table 12. Mechanical properties of Ni-Fe-Cr samples.

Sample	Yield Strength (MPa)	Ultimate Strength (MPa)	Elongation (%)
Ni 50 Fe	155	412	18.1
Ni 45 Fe 5 Cr	108	387	18.5
Ni 40 Fe 10 Cr	125	393	19.3
Ni 35 Fe 15 Cr	114	334	16.2

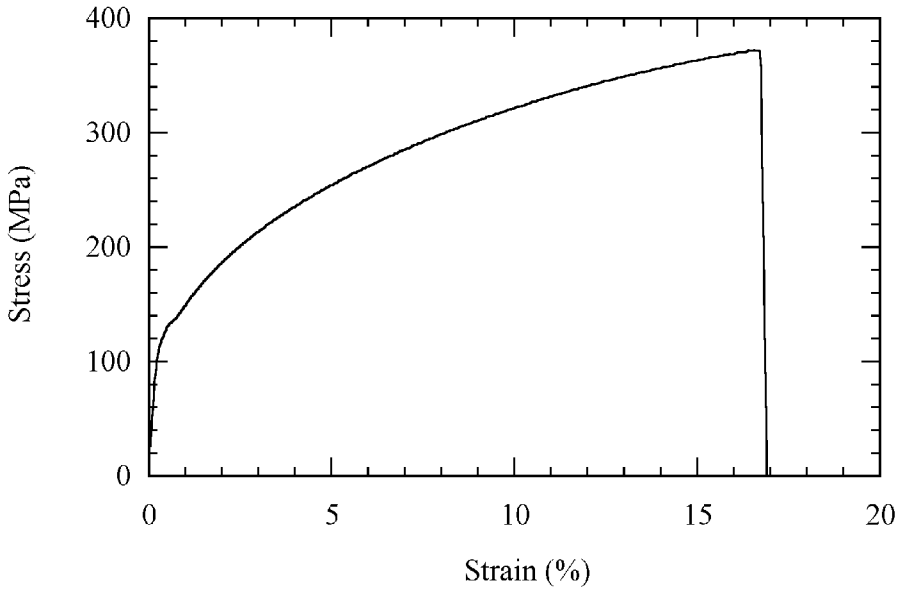

Figure 95. Stress-Strain curve for Ni 40 wt% Fe 10 wt% Cr.

Yield strength values ranged from 108 to 155 MPa for the samples tested. This is considerable lower than the fracture strength of YSZ which is approximately 200 to 300 MPa (dependent on porosity). Elongation at fracture ranged from 16.2 to 19.3% which was significantly higher than for Cu-based samples tested previously [52].

Based on the metallurgy of the Fe-Ni-Cr samples containing roughly 50 wt% Ni and 0 to 15 wt% Cr, it would be expected that other compositions in this general range (i.e. constant Fe and Fe/Ni = 1 samples) would have similar mechanical properties. The porosity present in these samples, Figure 25, has a detrimental effect on the mechanical properties. As discussed in detail by Bocchini [58], the presence of porosity results in a "knock-down effect" of strength and elongation values of a given material. However, even with the roughly 5 to 10 vol% porosity present in these samples, elongation values remained fairly high.

Mechanical properties of samples with an addition of CaO or Y_2O_3 were not examined in this work. It would be expected that the presence of a oxide particles within these alloys would result in increased strength and reduced elongation. Strength tends to increase due to the presence of the oxide particle as a result of the dispersion strengthening effect. The oxide particles act as barriers to dislocation flow thereby increasing strength. At the same time, the oxide particles would act to reduce elongation by providing crack nucleation sites. The question that remains to be answered is quantitatively how the presence of the CaO and yttria additions affect mechanical properties of these Fe-Ni-Cr alloys.

5. Conclusions

Alloy compositions were formed into honeycomb geometries through a paste extrusion technique from metal oxide precursors with accurate composition control. Actual alloy compositions were measured to be within 0.5 wt% (typical) of the intended composition. The thermal expansion behavior of a wide range of binary and ternary alloys comprised of iron, nickel, and chromium were analyzed. A technique was developed to calculate expansion mismatch between a given alloy and YSZ based on raw thermal expansion data.

The alloy most compatible with YSZ was found to change with the assumptions used to generate the expansion mismatch calculation. In general, Fe 20 wt% Cr and Fe 47.5 wt% Ni were shown to have low expansion mismatch with YSZ under a variety of heating and cooling conditions. The determination of the so-called zero-stress temperature for the alloy/YSZ hybrid solid oxide fuel cell structure is critical to calculate accurately the thermal expansion mismatch of a given alloy with YSZ. Fe-Cr alloys were shown to have superior oxidation resistance in air at 700 °C compared with Fe-Ni-Cr ternary alloys with similar chromium contents. It was shown that additions of CaO or Y_2O_3 as oxide dispersions into certain metal alloys have the potential to further improve oxidation resistance without affecting the thermal expansion behavior of the alloy. However, these additions were shown to hinder densification of the alloy during reduction heat-treatment

which resulted in higher as-reduced porosity levels. This could lead to detrimental impacts on other material properties such as reduced ductility or, at an extreme, loss of hermiticity. The combination of low expansion mismatch under a variety of conditions and the good oxidation resistance observed from the Fe 20 wt% Cr alloy makes it an likely candidate for use as a solid oxide fuel cell interconnect alloy.

These characterization techniques along with the honeycomb fabrication process provide a method by which potential alloys can be produced and screened rapidly to facilitate the development of an alloy for use as an interconnect in a solid oxide fuel cell.

6. Recommendations for Future Work

1. Determination of the zero-stress temperature.

Experiments should be performed to determine the temperature at which a given alloy can no longer deform plastically under cooling conditions. These experiments should be performed for a range of sample compositions to build an understanding of the impact of composition on the zero-stress temperature. Also, variation in cooling rates may have an affect on the observed zero-stress temperature. This information could then be used to modify the expansion mismatch calculations to provide a more accurate result.

2. Oxidation of potential alloys.

The oxidation behavior of a potential alloy must be determined under a variety of conditions. While the oxidation in air at a single temperature (as done here) provided a basic comparison of each alloy, a more detailed investigation is needed of alloys which show particular promise. The oxidation experiments should be performed under a variety of atmospheres ranging from pure air to pure hydrogen and possibly including methane atmospheres as well. In addition, oxidation tests at different temperatures would provide activation energy data for the different alloys. Post-oxidation analysis of the oxidation layer chemistry would provide additional insight into the oxidation process for each alloy. The electrical conductivity (or, contact resistance) of the oxide layers should also be investigated as this property has an impact on the efficiency of the SOFC.

3. Impact of oxide dispersions.

The ability to improve oxidation resistance without impacting thermal expansion behavior through the addition of an oxide dispersion was shown in this work. Additional experimentation should be aimed at understanding the mechanism by which the oxide dispersion improves oxidation resistance and the impact that alloy processing has on the final properties. Also, the potential benefits of other types of oxide additions, such as MgO or ZrO_2, should investigated. The addition of the oxide dispersion would likely affect the high-temperature mechanical properties of the alloy; this could be better understood by performing high-temperature tensile testing on alloys with various oxide additions.

Appendix

A.1 Smoothing / CTE Calculation of Thermal Expansion Data

Thermal expansion data were collected in the form of temperature versus $\Delta l/l_0$ datum pairs. The coefficient of thermal expansion (CTE), α_T, was calculated from the displacement versus temperature data as shown in Equation A.1

$$\alpha_T = \frac{dl/l_0}{dT} = \frac{1}{l_0}\frac{dl}{dT} \tag{A.1}$$

where T is temperature in °C, l_0 is the length at room temperature, and l is the length at a given temperature. With the raw dilatometer data of $\Delta l/l_0$ versus T, the value of α_T was calculated using a linear regression over small temperature intervals as shown in Equation A.2,

$$\alpha_T = \frac{n\sum x_i y_i - \sum x_i \sum y_i}{n\sum x_i^2 - \left(\sum x_i\right)^2} \tag{A.2}$$

where x_i represents a T datum point, y_i represents a $\Delta l/l_0$ datum point, and n is the range over which each regression is performed. Using this method, the value of α_T, strictly

speaking, is not the instantaneous slope at a point as expressed in Equation A.1. In order to approach the instantaneous slope, the value of *n* would have to approach zero. Of course, this is simply not possible when working with discrete datum pairs. At the other end of the spectrum, a value of *n* approaching the number of datum pairs in the set would provide a value of CTE approaching α_M which is the average CTE given by

$$\alpha_M = \frac{1}{l_0}\frac{\Delta l}{\Delta T} \tag{A.3}$$

Figure 96 shows the α_T versus temperature for pure iron as calculated from the same expansion data using three different values of *n*. Lower values of *n* result in a noisy plot with large variations in α_T over small temperature ranges. Increasing *n* tends to smooth the plot.

The CTE plot shown in Figure 96 includes a phase change at roughly 910 °C which causes the large discontinuity in the plot. A closer look at the region close to the phase change, Figure 97, reveals another effect of using different values of *n* in calculating CTE using Equation A.2. Increased values of *n* resulted in a lower observed α to γ transition temperature. Immediately after the phase change, increased values of *n* resulted in a higher observed 'end of phase-change event' temperature, as shown in Figure 98.

Variations in the *n* value give rise to a trade-off between smoothness of the CTE plot and resolution of discontinuities. Higher *n* values provide a smooth CTE versus temperature plot but with decreases sensitivity of discontinuities; lower *n* values have the opposite effect. The value of $n = 41$ was chosen as a good balance between smoothness and loss of sensitivity. This value was used to calculate CTE using Equation A.2 for each

expansion data set. For a typical experimental data set, the value of $n = 1$ equated roughly to a 20 °C temperature range.

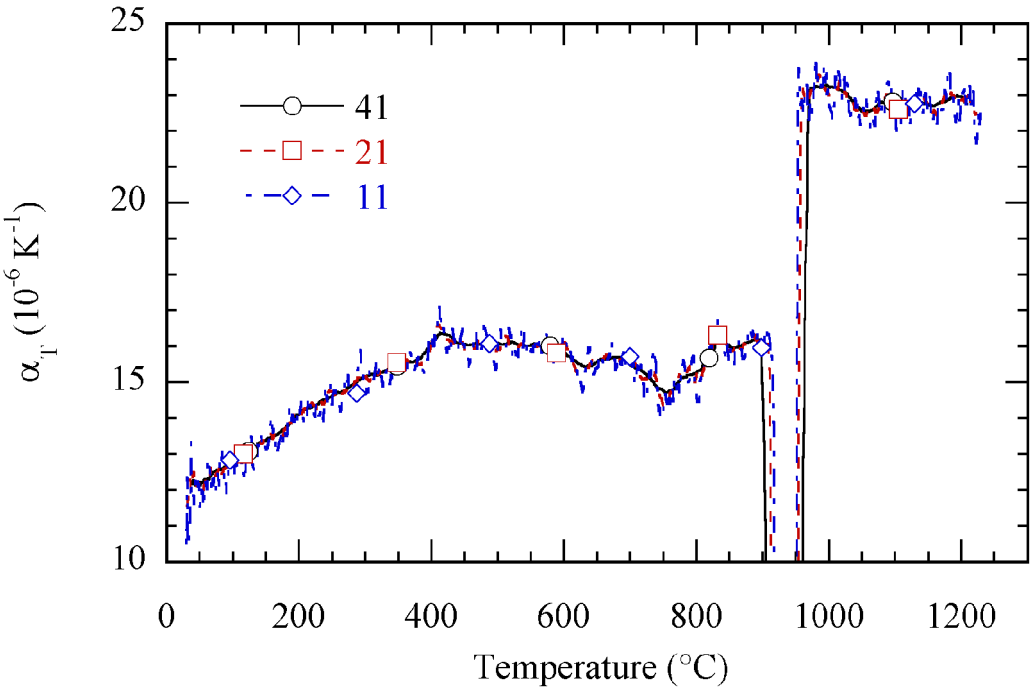

Figure 96. CTE of pure iron as calculated from the same expansion data set using three values of n (n = 41, 21 and 11).

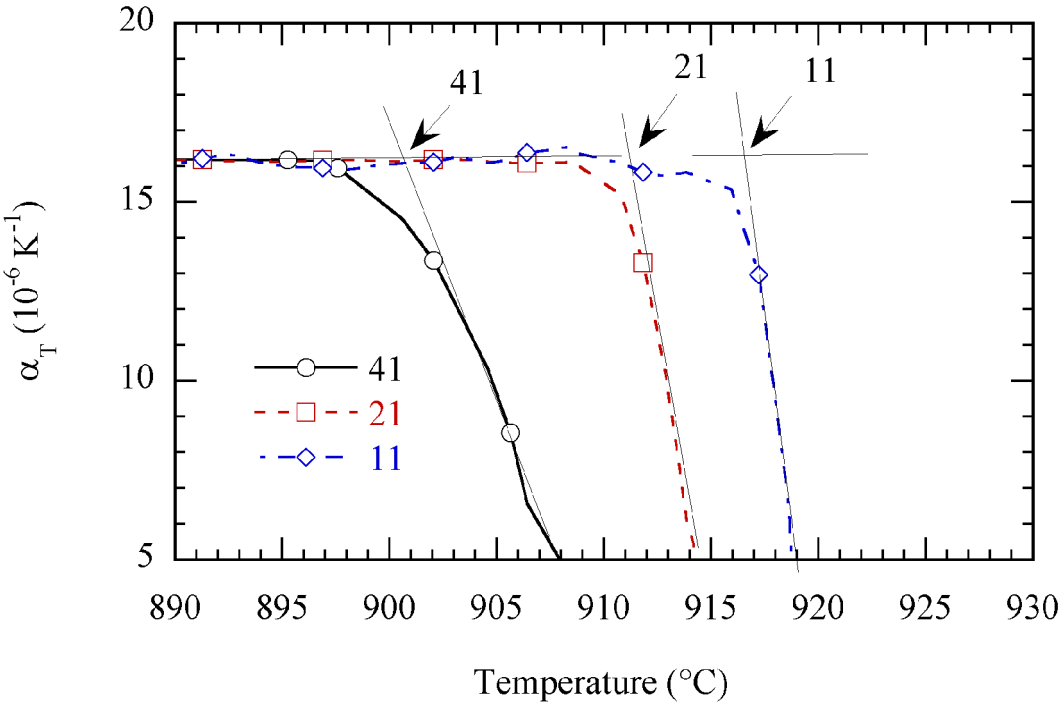

Figure 97. CTE versus temperature for pure iron in the region of the α to γ transition.

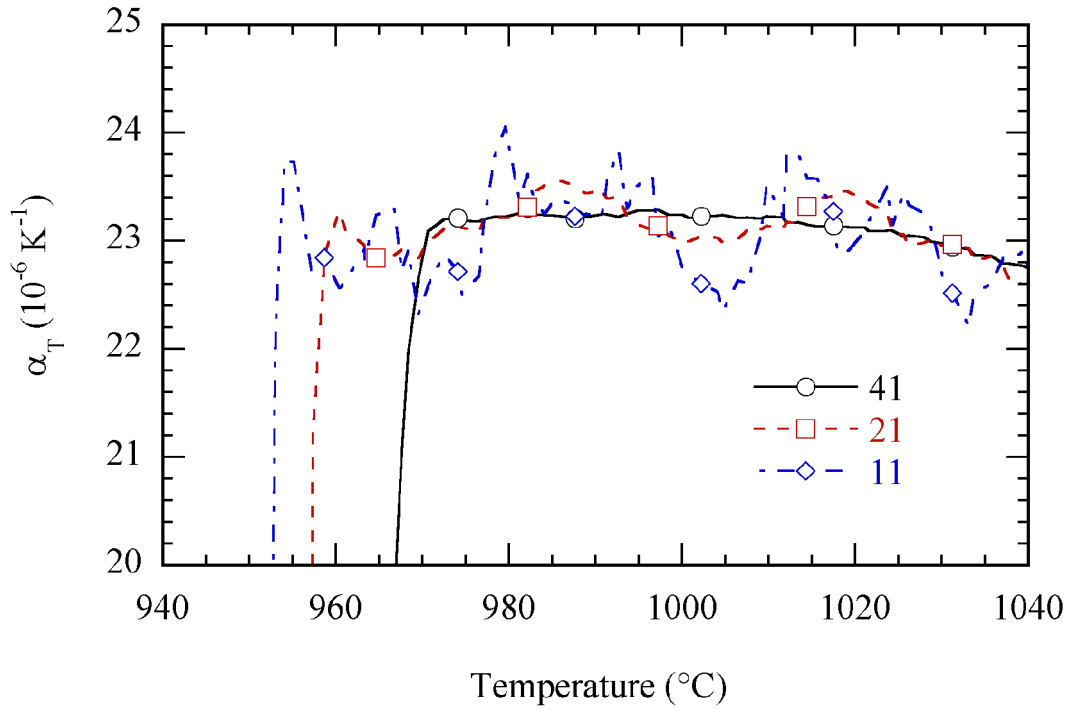

Figure 98. CTE versus temperature for pure iron immediately after the α to γ transition.

A.2 Linear thermal expansion and CTE plots.

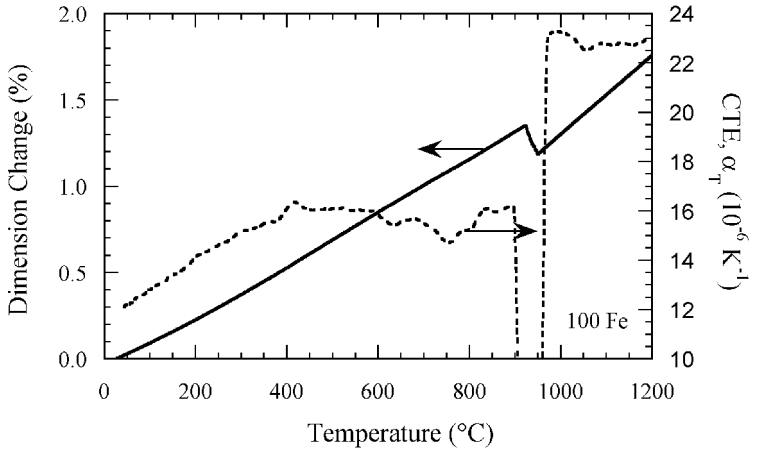

Figure 99. CTE and Expansion for 100 Fe.

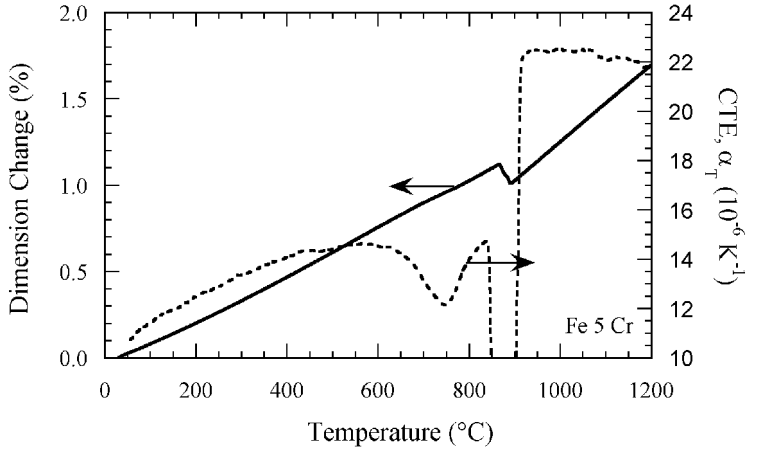

Figure 100. CTE and Expansion for Fe 5 Cr.

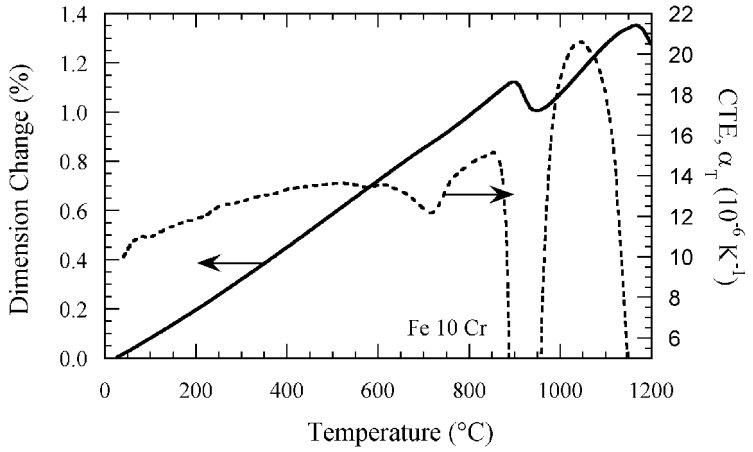

Figure 101. Expansion and CTE for Fe 10 Cr.

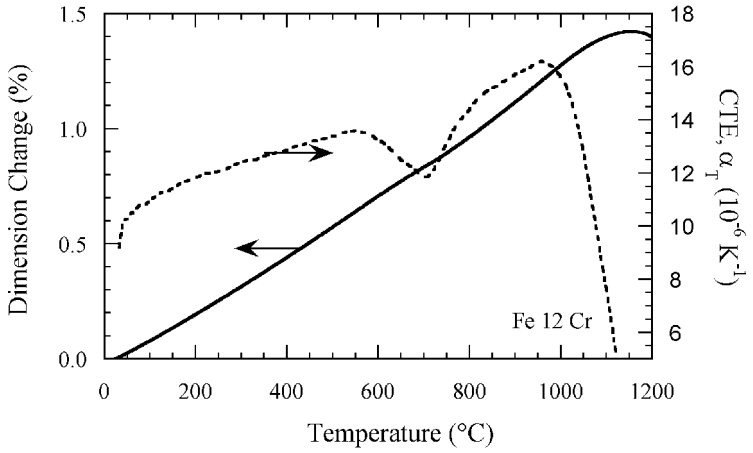

Figure 102. Expansion and CTE for Fe 12 Cr.

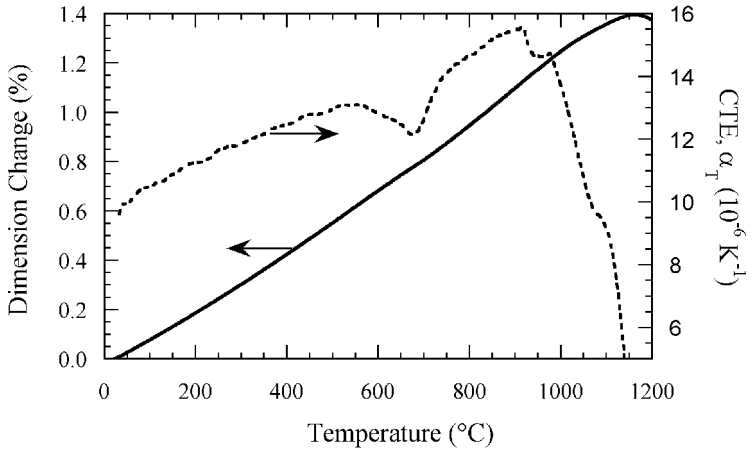

Figure 103. Expansion and CTE for Fe 15 Cr.

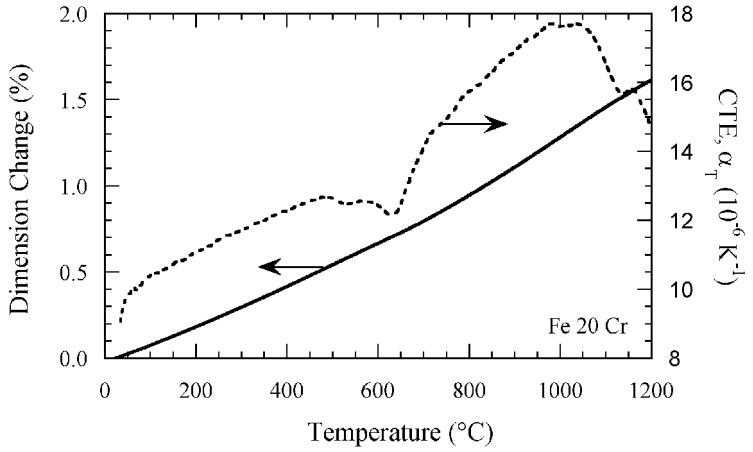

Figure 104. Expansion and CTE for Fe 20 Cr.

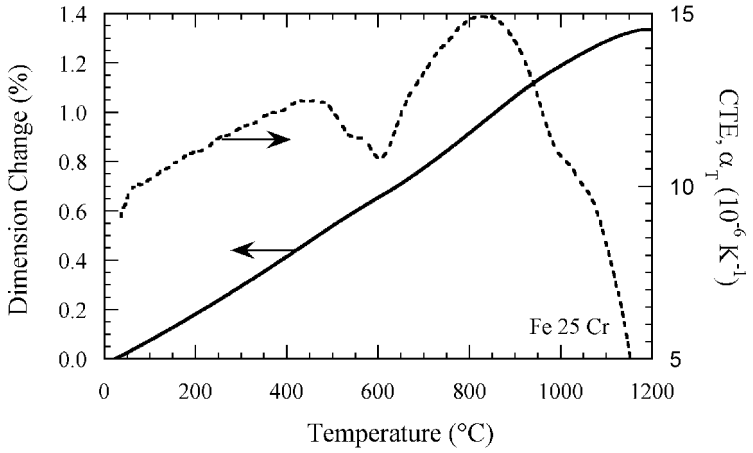

Figure 105. Expansion and CTE for Fe 25 Cr.

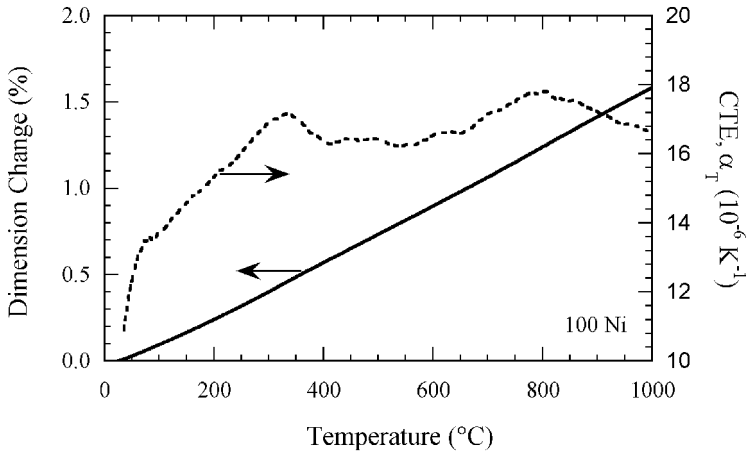

Figure 106. Expansion and CTE for 100 Ni.

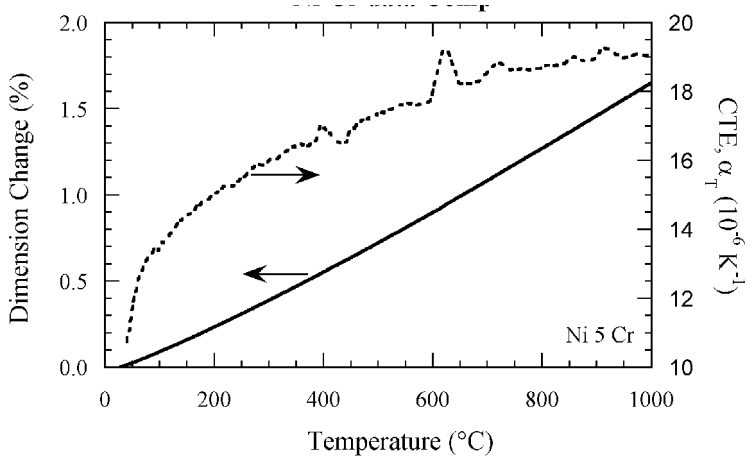

Figure 107. Expansion and CTE for Ni 5 Cr.

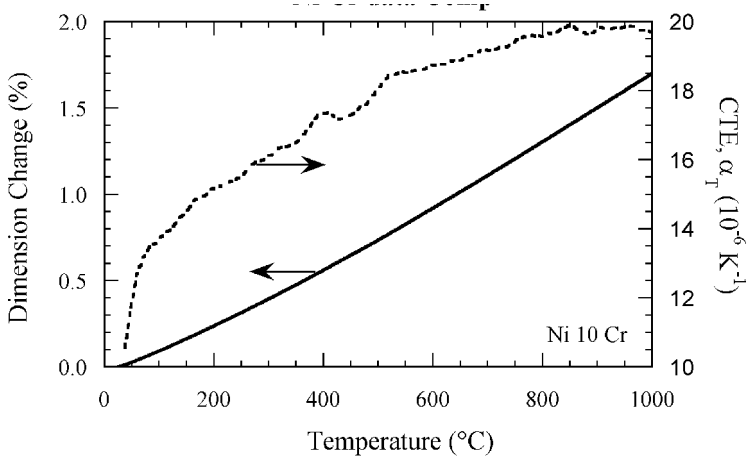

Figure 108. Expansion and CTE for Ni 10 Cr.

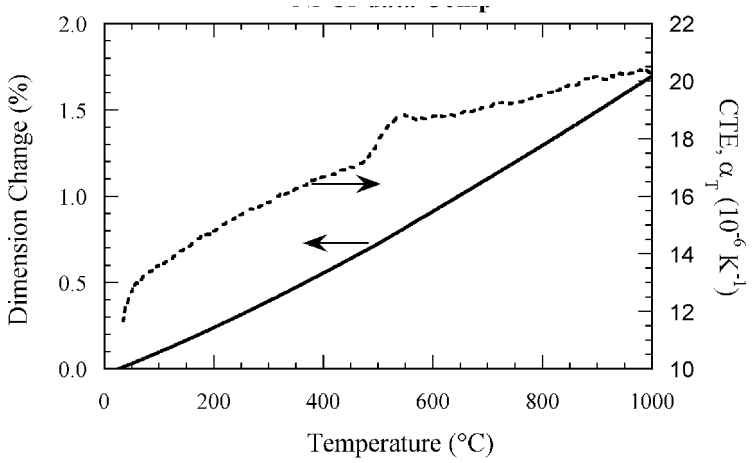

Figure 109. Expansion and CTE for Ni 15 Cr.

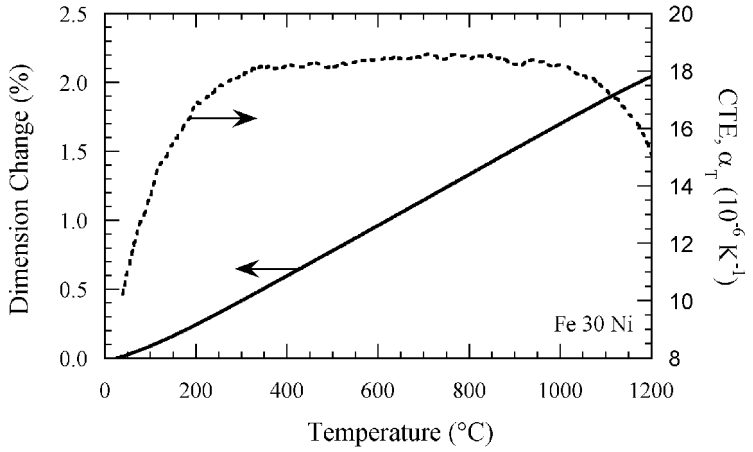

Figure 110. Expansion and CTE for Fe 30 Ni.

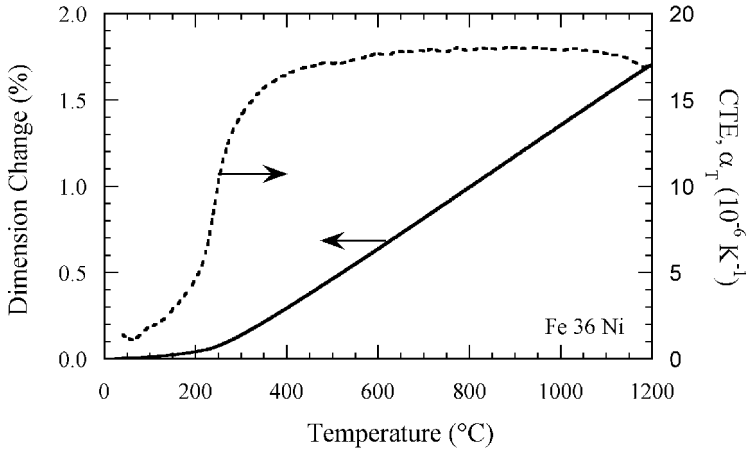

Figure 111. Expansion and CTE for Fe 36 Ni.

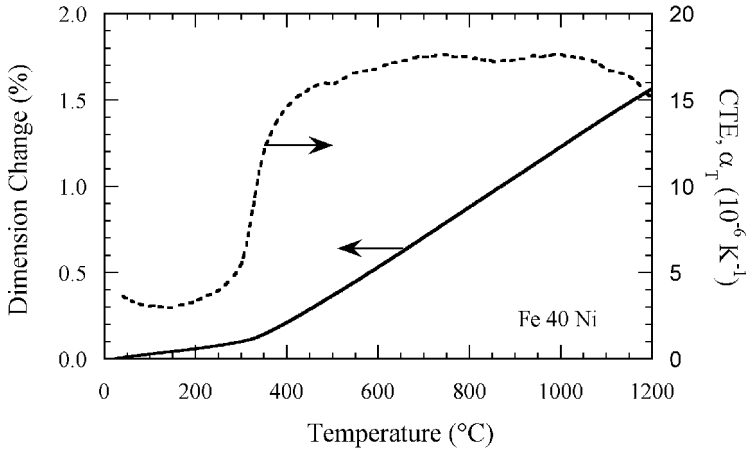

Figure 112. Expansion and CTE for Fe 40 Ni.

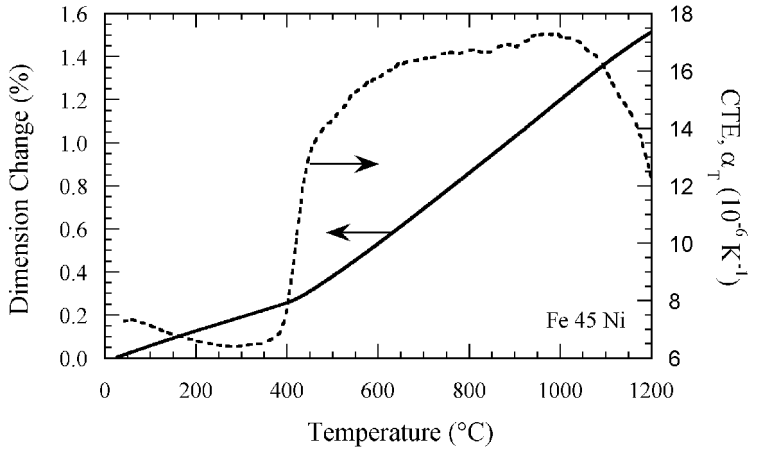

Figure 113. Expansion and CTE for Fe 45 Ni.

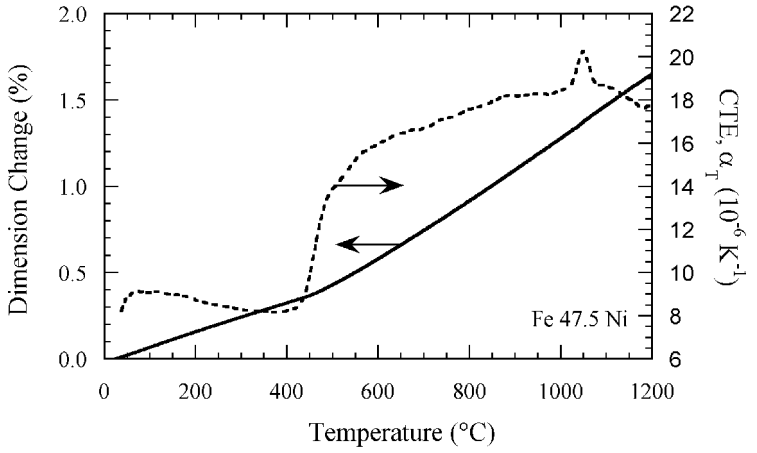

Figure 114. Expansion and CTE for Fe 47.5 Ni.

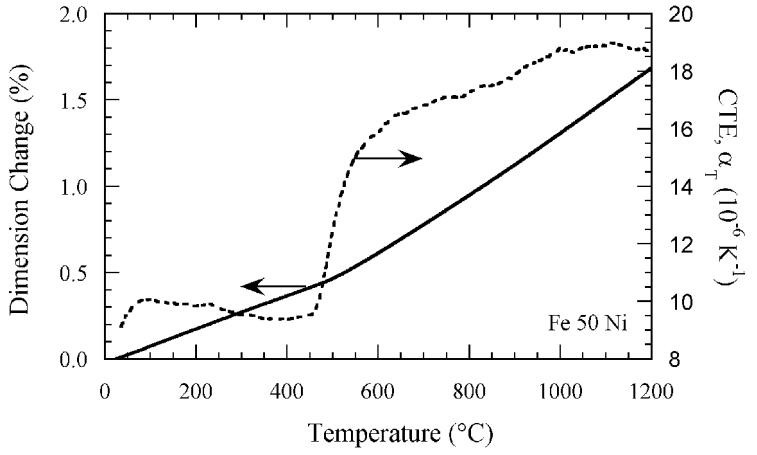

Figure 115. Expansion and CTE for Fe 50 Ni.

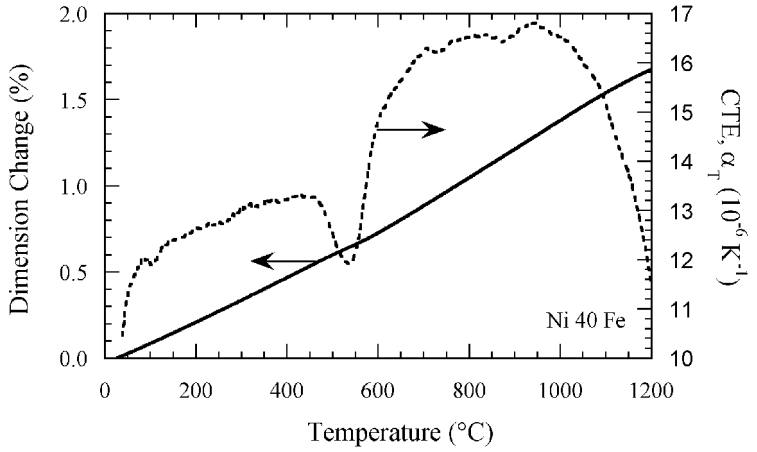

Figure 116. Expansion and CTE for Ni 40 Fe.

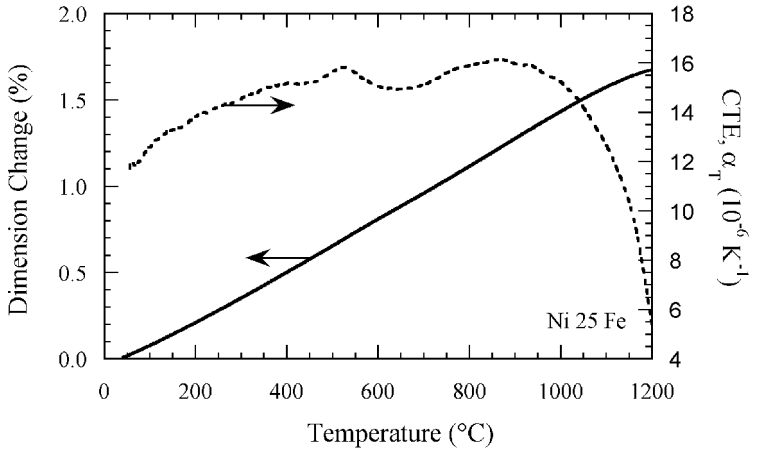

Figure 117. Expansion and CTE for Ni 25 Fe.

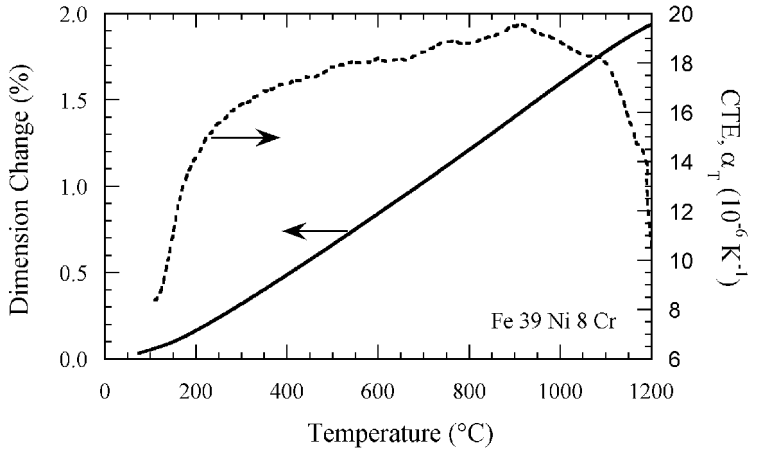

Figure 118. Expansion and CTE for Fe 39 Ni 8 Cr.

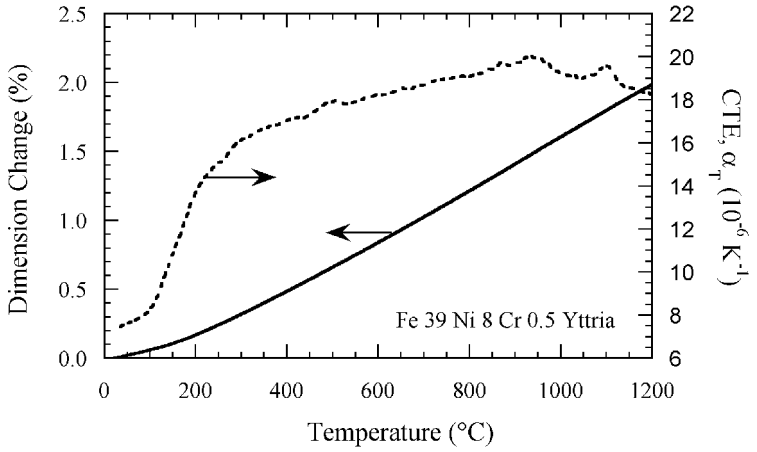

Figure 119. Expansion and CTE for Fe 39 Ni 8 Cr 0.5 Y_2O_3.

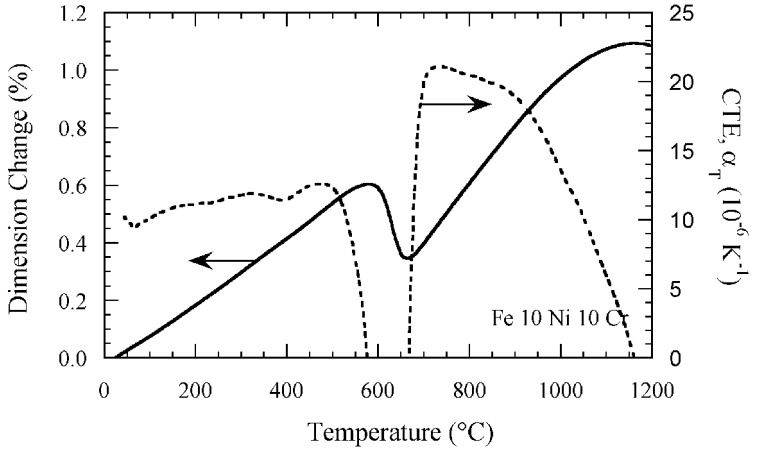

Figure 120. Expansion and CTE for Fe 10 Ni 10 Cr.

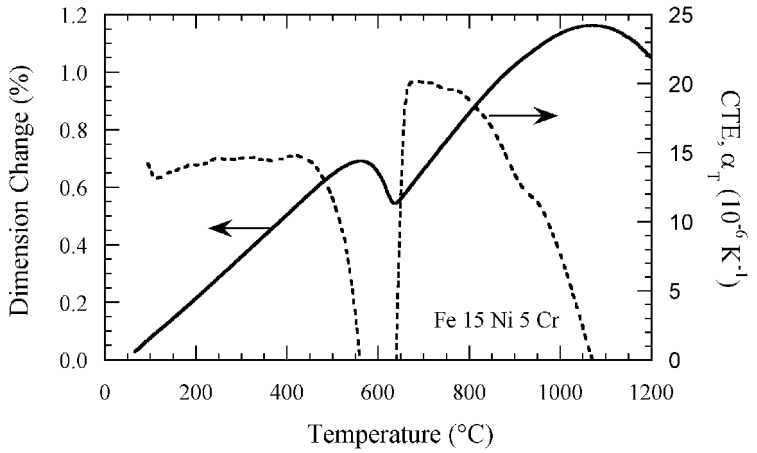

Figure 121. Expansion and CTE for Fe 15 Ni 5 Cr.

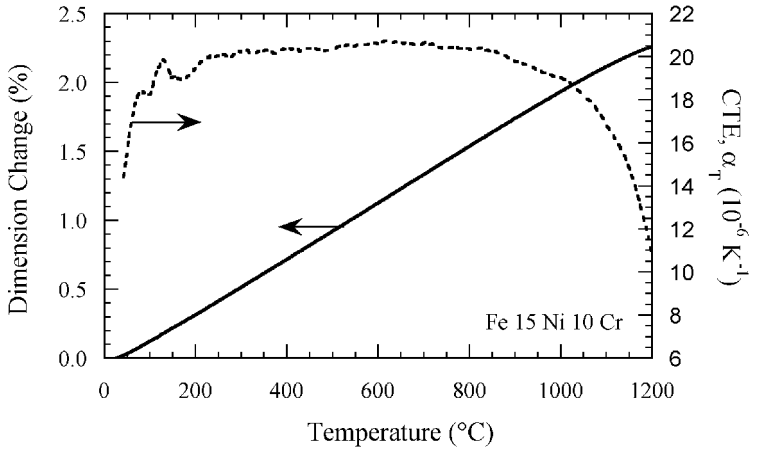

Figure 122. Expansion and CTE for Fe 15 Ni 10 Cr.

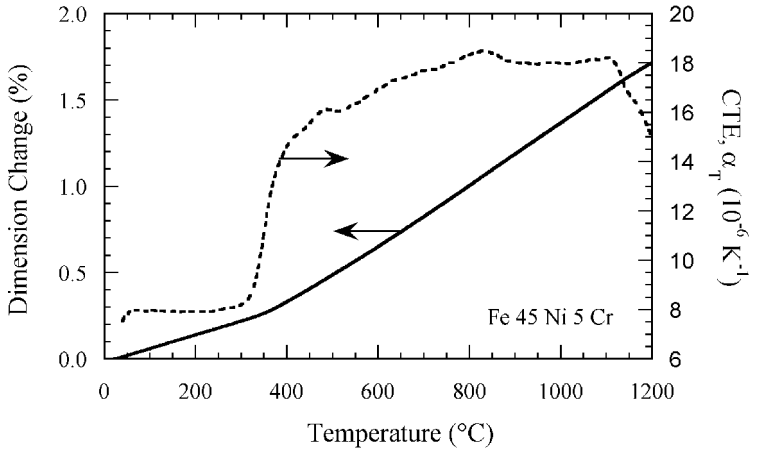

Figure 123. Expansion and CTE for Fe 45 Ni 5 Cr.

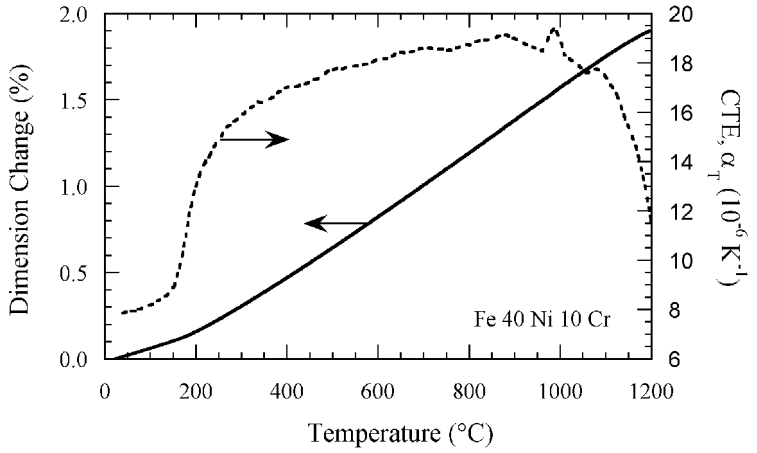

Figure 124. Expansion and CTE for Fe 40 Ni 10 Cr.

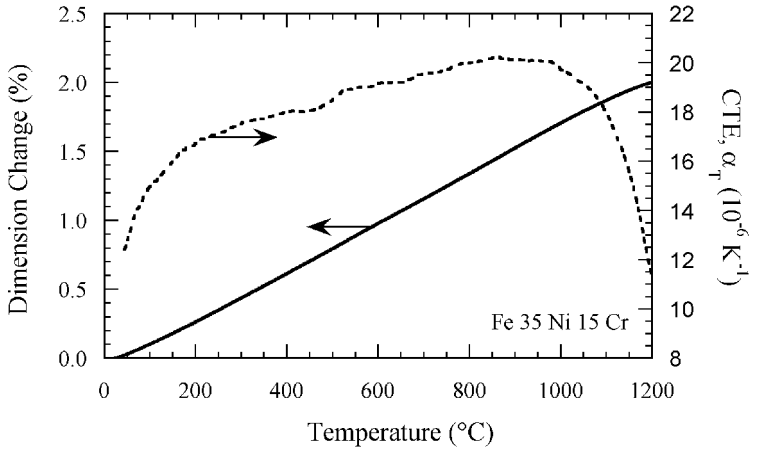

Figure 125. Expansion and CTE for Fe 35 Ni 15 Cr.

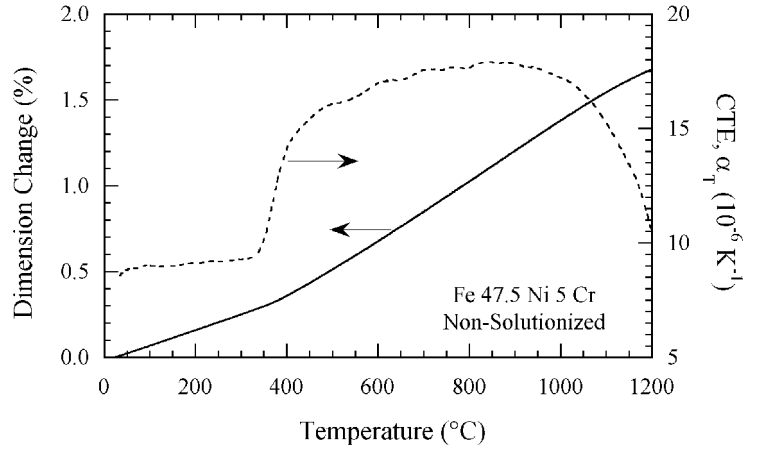

Figure 126. Expansion and CTE for Fe 47.5 Ni 5 Cr non-solutionized.

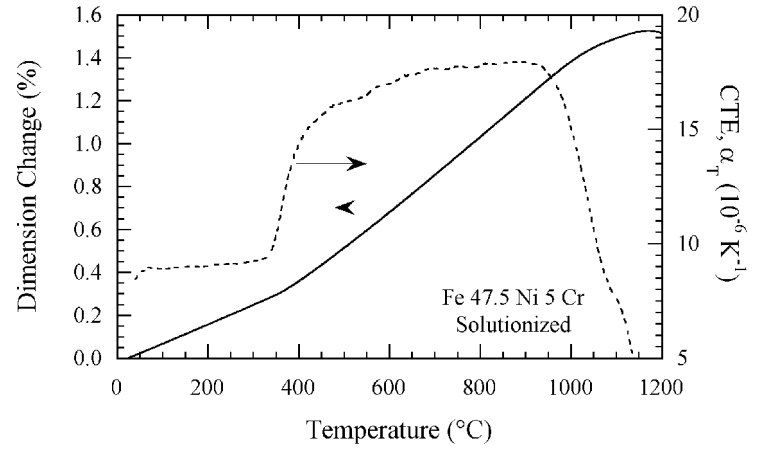

Figure 127. Expansion and CTE for Fe 47.5 Ni 5 Cr solutionized.

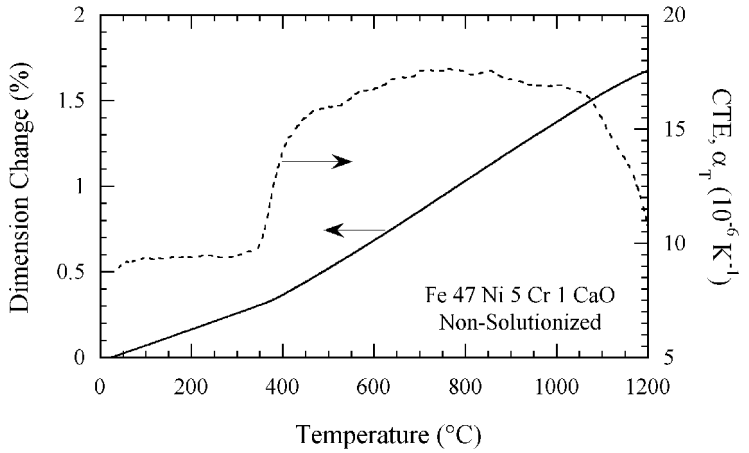

Figure 128. Expansion and CTE for Fe 47.5 Ni 5 Cr 1 CaO non-solutionized.

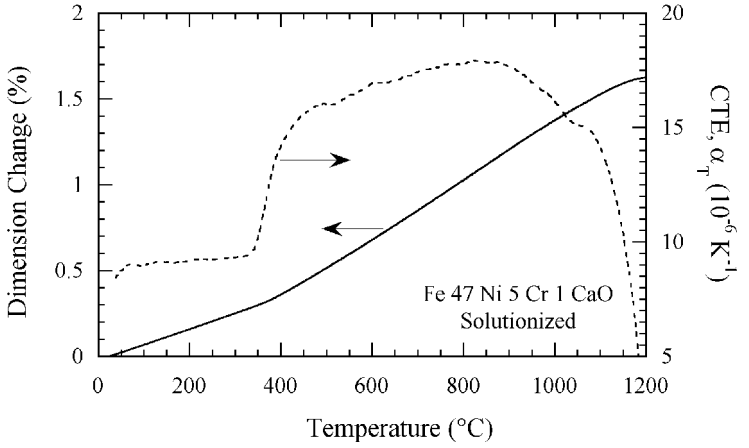

Figure 129. Expansion and CTE for Fe 47.5 Ni 5 Cr 1 CaO solutionized.

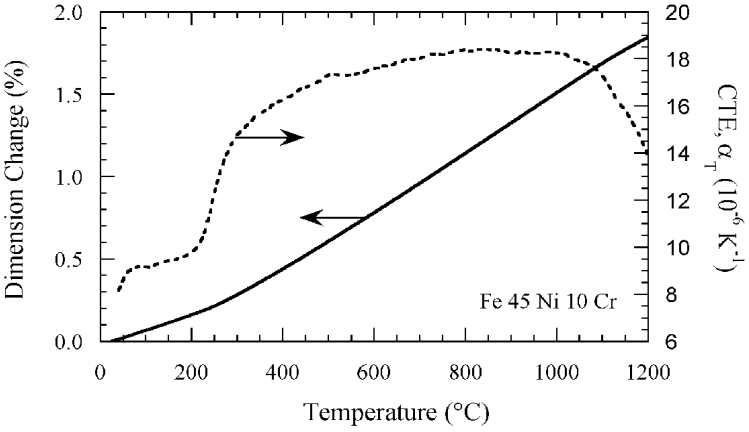

Figure 130. Expansion and CTE for Fe 45 Ni 10 Cr.

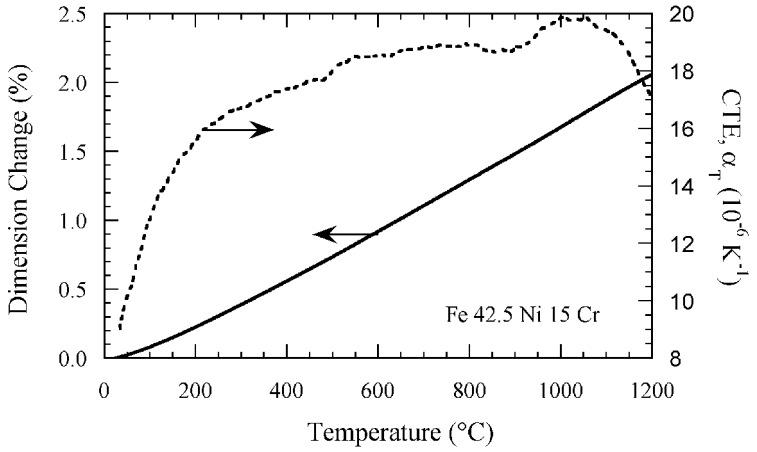

Figure 131. Expansion and CTE for Fe 42.5 Ni 15 Cr

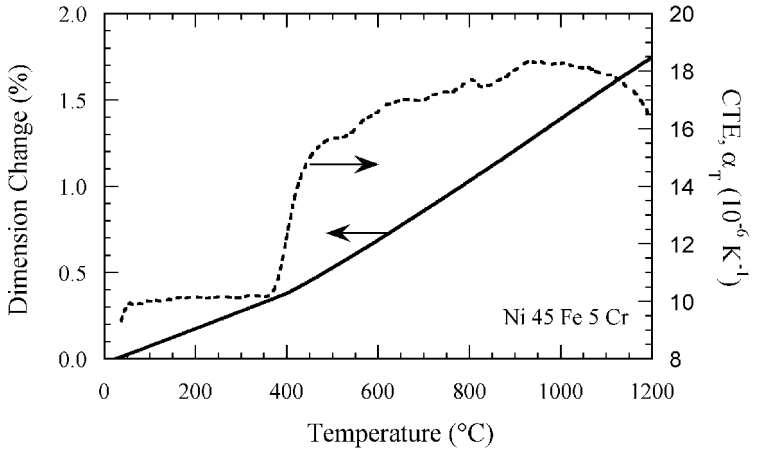

Figure 132. Expansion and CTE for Ni 45 Fe 5 Cr.

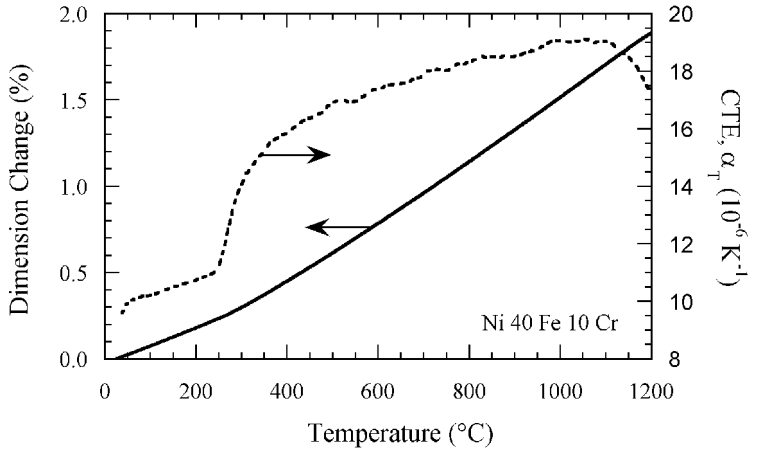

Figure 133. Expansion and CTE for Ni 40 Fe 10 Cr.

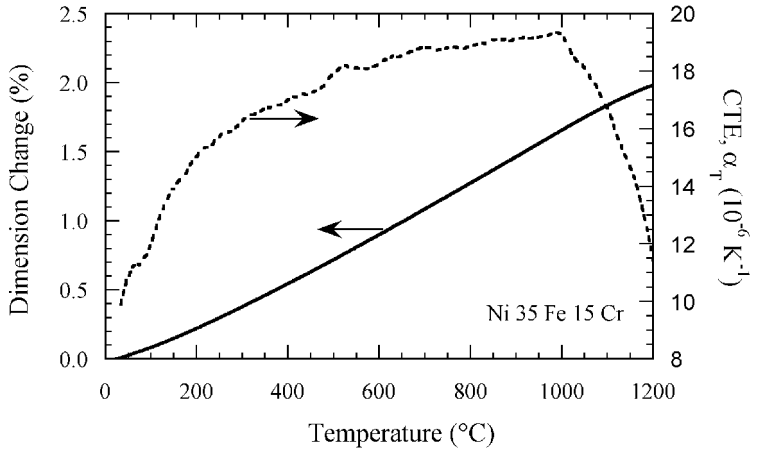

Figure 134. Expansion and CTE for Ni 35 Fe 15 Cr.

References

1 N.Q. Minh: "Ceramic fuel cells", *Journal of the American Ceramic Society* **76** (3), 563 (1993).

2 S. Linderoth, P.V. Hendriksen and M. Mogensen: Investigations of metallic alloys for use as interconnects in solid oxide fuel cell stacks, *Journal of Materials Science* **31** (1996) 5077.

3 W. Rauch, K.J. Lee, J. Cochran and M. Liu, in Solid Oxide Fuel Cells VIII Proceedings of the International Symposium, Paris, 2003, edited by S.C. Singhal and M. Dokiya (The Electrochemical Society, Pennington, N.J. 2003) p. 1090.

4 J. Cochran, K.Hurysz, K.J. Lee and T. Sanders: Extrusion and thermo-chemical processing of layered linear cellular materials, *Materials Science Forum* **426-432** (2003) 4295.

5 S. Eisele "Characterization of material behavior during the manufacturing process of a co-extruded solid oxide fuel cell" Masters Thesis, School of Mechanical Engineering, Georgia Institute of Technology, (2004).

6 C.S. Montross, H. Yokokawa, and M. Dokiya: Thermal stresses in planar solid oxide fuel cells due to thermal expansion differences, *British Ceramic Transactions* **101** (3) (2002) 85.

7 D.J. Hall and G.R. Colclaser, IEEE Trans. Energ. Conv. **14** (1999) 749.

8 C.S. Montross, *Journal of the European Ceramic Society* **18** (1997) 353.

9 O.T. Iancu and D. Munz, in Joining of Ceramics, glass and metal, W. Craft, editor, Oberursel, DGM (1989).

10 D. Burgreen, Elements of thermal stress analysis, Arcturus Publishers, Cherry Hill, NJ (1972).

11 P. Kofstad, High-Temperature Oxidation of Metals, John Wiley & Sons, New York, NY (1966).

12 S.P. Jaing, J.P. Zhang, and X.G. Zheng: A comparative investigation of chromium

deposition at air electrides of solid oxide fuel cells, *Journal of the European Ceramic Society* **22**, (2002) p. 361.

13 Y. Matsuzaki and I. Yasuda: Dependance of SOFC cathode degradation by chromium-containing alloy on compositions of electrodes and electrolytes, *Journal of the Electrochemical Society* **148** (2), (2001) p. A-126.

14 W.Z. Zhu and S.C. Deevi: Development of interconnect materials for solid oxide fuel cells. *Materials Science and Engineering* **A348**, 227 (2003).

15 W.J. Quadakkers, J. Piron-Abellan, V. Shemet and L. Singheiser: Metallic interconnectors for solid oxide fuel cells - a review. *Materials At High Temperatures* **20** (2), 115 (2003).

16 ASM Handbook Vol. 3, Alloy Phase Diagrams, ASM International, Materials Park, OH, (1992).

17 W.F. Smith, Structure and Properties of Engineering Alloys (Second Edition), McGraw-Hill, New York, NY, (1993).

18 S. Linderoth and P.H. Larsen, in *New materials for batteries and fuel cells*, edited by D.H. Doughty and L.F. Nazar, (Materials Research Symposium Proceedings Volume 575, San Fransisco, CA 1999) p. 325.

19 T. Uehara, A. Toji, K. Inoue, M. Yamaguchi and T. Ohno, in *Solid Oxide Fuel Cells VIII Proceedings of the International Symposium*, edited by S.C. Singhal and M. Dokiya (The Electrochemical Society, Pennington, N.J. 2003) p. 915.

20 K. Huang, P. Hou and J. Goodenough: Characterization of iron-based alloy interconnects for reduced temperature solid oxide fuel cells. *Solid State Ionics* **129**, 237 (2000).

21 T. Horita, Y. Xiong, K. Yamaji, N. Sakai and H. Yokokawa: Evaluation of Fe-Cr alloys as interconnects for reduced operation temperature SOFCs. *Journal of the Electrochemical Society* **150** (3), A243 (2003).

22 W.A. Mullenberg, S. Uhlenbruck, E. Wessel, H.P. Buchkremer and D. Stover: Oxidation behaviour of ferrous alloys used as interconnecting material in solid oxide fuel cells. *Journal of Materials Science* **38**, 507 (2003).

23 L. Mikkelsen and S. Linderoth: High temperature oxidation of Fe-Cr alloy in O_2-H_2-H_2O atmospheres; microstructure and kinetics, Materials Science and Engineering A 361, (2003) p.198.

24 T. Horita, Y. Xiong, K. Yamaji, N. Sakai and H. Yokokawa: Stability of Fe-Cr alloy

interconnects under CH_4-H_2O atmosphere for SOFCs, *Journal of Power Sources* **118**, (2003) p.35.

25 A. Martinez-Villafañe, J.G. Chacon-Nava, C. Gaona-Tiburcio, F. Almeraya-Calderon, G. Dominguez-Patiño, J.G. Gonzalez-Rodriguez: Oxidation performance of a Fe 13Cr alloy with additions of rare earth elements, Materials Science and Engineering **A363**, (2003) p. 15.

26 H. Greneir, T. Grögler, W. Köck and R. Singer, in Solid Oxide Fuel Cells IV , edited by M. Dokiya, O. Yamamoto, H. Tagawa and S.C. Singhal, (The Electrochemical Society, Pennington, N.J. 1995) p. 879.

27 J.H. Nadler, "Hydrogen reduction of iron and chromium oxides", Ph.D. Thesis, School of Materials Science and Engineering, Georgia Institute of Technology, (2003).

28 C.E. Guillaume, *Acad. Sci.* **125**, 235-238 (1897).

29 C.E. Guillaume, *Compt. Rend, Acad. Sci* **170**, 1554 (1920).

30 M. van Schilfgaarde, I.A. Abrikosov, and B. Johansson: Origin of the Invar effect in iron-nickel alloys. *Nature* **400**, 46-49 (1999).

31 Physics and Applications of Invar Alloys, Maruzen Company, Ltd. Tokyo, Japan (1978).

32 P. Chevenard, *Rev. Metall.* (Paris) **11**, 108 (1914).

33 Z. Yang, K.S. Weil, D.M. Paxton, and J.W. Stevenson: Selections and evaluation of heat-resistant alloys for SOFC interconnect application, *Journal of the Electrochemical Society* **150** (9), (2003), p. A1188.

34 J. Groza, "Heat Resistant Dispersion-Strengthened Copper Alloys," *Journal of Materials Engineering and Performance*, Vol. 1 (1), pp. 113-121, 1992.

35 J. Groza and J. C. Gibeling, "Principles of Particle Selection for Dispersion-Strengthened Copper," *Materials Science and Engineering A*, Vol. A171, pp. 115-125, 1993.

36 G. H. Gessinger, Powder Metallurgy of Superalloys, Butterworth and Company, London, p.225, 1984.

37 M.H Tikkanen and S. Ylasaari, *Physics of Sintering* 1 (1969) p. J1.

38 K. Takahashi, et al., "Sintering Characteristics of the MgO-Dispersed Ni Powder Reduced from (Ni,Mg)O", *Journal of the Japan Institute of Metals* **63** (5), (1999), p. 634.

39 L.V. Ramanathan: Corrosion control with rare earths, *Corrosion Prevention and Control* **45** (3), (1998), p. 87.

40 B.C. Church, J.K. Cochran and T.H. Sanders, Jr. in Processing and Properties of Lightweight Cellular Metals and Structures: Structural and Multifunctional Applications, A Gosh, ,T.H. Sanders and D. Claar, Editors, TMS, Warrendale, PA, (2002)

41 J.L. Clark, J.K. Cochran, T.H. Sanders and K.J. Lee in Processing and Properties of Lightweight Cellular Metals and Structures: Structural and Multifunctional Applications, A Gosh, ,T.H. Sanders and D. Claar, Editors, TMS, Warrendale, PA, (2002)

42 B.C. Church Materials and Manufacturing Processes 2004

43 B. Dempsey, "Thermal properties of linear cellular alloys", Masters Thesis, School of Mechanical Engineering, Georgia Institute of Technology, (2003).

44 J.L. Clark, "Dynamic and quasi-static mechanical properties of Fe-Ni alloy honeycomb", Ph.D. Thesis, School of Materials Science and Engineering, Georgia Institute of Technology, (2004).

45 A.M. Hayes, "Compression behavior of linear cellular steel" Masters Thesis, School of Materials Science and Engineering, Georgia Institute of Technology, (2002).

46 I. Hattori, "Ceramic Honeycomb Substrates for Automobile Exhaust Catalysts," *Ceramics Japan* **29** (4) (1994) 307.

47 J.H. Nadler, T.H. Sanders and R.F. Speyer: Oxide reduction and sintering of Fe-Cr alloy honeycombs. *Journal of Materials Research* **18** (8), 1787 (2003).

48 J.D. James, J.A. Spittle, S.G.R. Brown and R.W. Evans: A review of measurement techniques for the thermal expansion coefficient of metals and alloys at elevated temperatures, *Measurement Science and Technology* **12** (2001) R1.

49 J.B. Nelson and D.P. Riley: An experimental investigation of extrapolation methods in the derivation of accurate unit-cell dimensions of crystals, *Proceedings of the Physics Society* (London) **57**, (1945) p. 160.

50 W.B. Pearson: A Handbook of Lattice Spacings and Structures of Metals and Alloys, Pergamon Press, New York, (1958).

51 F.W. Jones and W.I. Pumphrey: Free energy and metastable states in the iron-nickel and iron-manganese systems. *Journal of the Iron and Steel Institute* **163**, (1949) p.781.

52 B.C. Church, "High conductivity alloys for extruded metallic honeycomb", Masters

Thesis, School of Materials Science and Engineering, Georgia Institute of Technology, (2002).

53 M.F. Ashby, S. Bahk, J. Bevk and D. Turnbull: "The influence of a dispersion of particles on the sintering of metal powders and wires", *Progress in Materials Science* **25**, (1980) p. 1.

54 R.P. Ingles, D. Lexis, B.A. Bender and R.W. Rice, *Journal of the American Ceramic Society* **65** (1982) C150.

55 P. Chevenard: Alliages de fer, de nickel, et de chrome. T*ravaux et Memoires du Bureau International des Poids et Mesures* **17** (1927) p. 72.

56 R.W. Evans and B. Wilshire, Creep of Metals and Alloys, The Institute of Metals, London (1985) p.4.

57 R.E. Reed-Hill: Physical metallurgy principles, PWS Publishing, Boston, (1994) p. 231.

58 G.F. Bocchini: The influence of porosity on the characteristics of sintered materials, *The International Journal of Powdered Metallurgy* **22** (3), (1986), p. 185.

Vita

Benjamin Cortright Church was born in Saginaw, Michigan on November 3, 1972, the son of Mary Ann and James Brownlee Church. After graduating from Arthur Hill High School in Saginaw, Michigan in 1991, he attended Michigan Technological University in Houghton, Michigan. There, he studied Materials Science / Metallurgical Engineering and received a Bachelor's of Science degree, *magna cum laude*, in 1997. From 1997 to 1999 he was employed as an Engineer at Honda R&D Americas, Inc. in Raymond, Ohio. In August 1999, he enrolled in the School of Materials Science and Engineering at Georgia Institute of Technology in Atlanta, Georgia. In May of 2001, Benjamin married Carmen Maria Perez. He completed a thesis entitled "High Conductivity Alloys for Extruded Metallic Honeycomb" and received a Masters of Science in Materials Science and Engineering in 2002. Benjamin earned the degree Doctor of Philosophy in Materials Science at Georgia Tech in December 2004.